

Spring 2005

## A Computational Study of Thermo-Fluid Dynamics of Pulse Detonation Engines

Alberto Davila Urresti

*Embry-Riddle Aeronautical University - Daytona Beach*

Follow this and additional works at: <https://commons.erau.edu/db-theses>



Part of the [Aerospace Engineering Commons](#), and the [Computer Engineering Commons](#)

---

### Scholarly Commons Citation

Urresti, Alberto Davila, "A Computational Study of Thermo-Fluid Dynamics of Pulse Detonation Engines" (2005). *Theses - Daytona Beach*. 223.

<https://commons.erau.edu/db-theses/223>

This thesis is brought to you for free and open access by Embry-Riddle Aeronautical University – Daytona Beach at ERAU Scholarly Commons. It has been accepted for inclusion in the Theses - Daytona Beach collection by an authorized administrator of ERAU Scholarly Commons. For more information, please contact [commons@erau.edu](mailto:commons@erau.edu).

A COMPUTATIONAL STUDY OF THERMO-FLUID DYNAMICS OF PULSE  
DETONATION ENGINES

By

Alberto Dávila Urresti

A Thesis Submitted to the Graduate Studies Office in Partial Fulfillment of the  
Requirements for the Degree of Master of Science in Aerospace Engineering

Embry-Riddle Aeronautical University

Daytona Beach, Florida

Spring 2005

UMI Number: EP32049

### INFORMATION TO USERS

The quality of this reproduction is dependent upon the quality of the copy submitted. Broken or indistinct print, colored or poor quality illustrations and photographs, print bleed-through, substandard margins, and improper alignment can adversely affect reproduction.

In the unlikely event that the author did not send a complete manuscript and there are missing pages, these will be noted. Also, if unauthorized copyright material had to be removed, a note will indicate the deletion.

**UMI<sup>®</sup>**

---

UMI Microform EP32049  
Copyright 2011 by ProQuest LLC  
All rights reserved. This microform edition is protected against  
unauthorized copying under Title 17, United States Code.

---

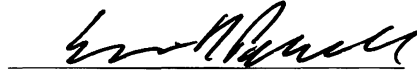
ProQuest LLC  
789 East Eisenhower Parkway  
P.O. Box 1346  
Ann Arbor, MI 48106-1346

# **A Computational Study of Thermo-Fluid Dynamics of Pulse Detonation Engines**

**By Alberto Dávila Urresti**

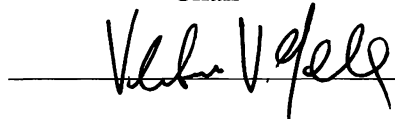
This thesis was prepared under the direction of the candidate's thesis committee chair, Dr. Eric R. Perrell, Department of Aerospace Engineering, and has been approved by the members of this committee. It was submitted to the Graduate Studies Office and accepted in Partial Fulfillment of the Requirements for the Degree of Master of Science in Aerospace Engineering.

THESIS COMMITTEE:



Dr. Eric R. Perrell

Chair



Dr. Vladimir Golubev

Member



Dr. Lakshman Narayanaswami

Member



Dr. Habib Eslami

Aerospace Engineering Department Chair



Associate Provost

Defended 1/23/06

Date

## ABSTRACT

**Author:** Alberto E. Dávila

**Title:** A Computational Study of Thermo-Fluid Dynamic of Pulse Detonation Engines

**Institution:** Embry-Riddle Aeronautical University

**Degree:** Masters of Science in Aerospace Engineering

**Year:** 2005

The purpose of this thesis is to use a transient Computational Fluid Dynamics computer code written in FORTRAN 90 for full reaction kinetics, to perform an analysis of the physical processes and chemical phenomena occurring on a single cycle of an ideal Pulse Detonation Engine (PDE) using a stoichiometric mixture of H<sub>2</sub> and O<sub>2</sub>. A small zone of high pressure and temperature is used to initiate the detonation wave in the PDE. A simple case with no chemical reactions and the same PDE geometry and “computational spark” is also tested. The speed of the wave relative to the reactants and a comparison with the simple case with no chemical reactions are used to verify the existence of a detonation wave being driven by the combustion of the reactants. The results and behavior of the detonation wave as it propagates through and out of the PDE are compared to those of similar numerical and experimental PDE cases in the literature, to verify the accuracy of the results. The results show that the basic physics and chemical phenomena occurring in the PDE can be modeled using a first order accurate computational code with non-equilibrium kinetics.

In future works the accuracy of the code will be increased to six-order in the spatial dimension to be able to model highly structured phenomena such as Deflagration to Detonation Transition (DDT) and fuel injection in supersonic flow for PDE applications.

## **ACKNOWLEDGEMENTS**

The author wishes to express special thanks to the Thesis Advisor, Dr. Eric Perrell, for his constant support, help and encouragement throughout the project. His input and suggestions made it possible for a positive and interesting outcome of this thesis. The author really enjoyed working with this new interesting type of propulsive technology, and thus the author would also like to also thank Dr. Vladimir Golubev for suggesting the topic for this thesis.

The author would like to thank Mr. Uyi Idahosa, lab administrator at Embry-Riddle Aeronautical University's Aerodynamics and Propulsion Computational Lab, for his patience and help while trouble shooting LINUX cluster operating problems.

## **DEDICATION**

The author would like to dedicate this Thesis to his parents, Alberto y Lupe Davila, whose sacrifice, love and support made it possible for the author to realize his dream of becoming an Aerospace Engineer.

The present thesis is also dedicated to my wife Katryn, for her love, constant support and encouragement.



## TABLE OF CONTENTS

I. INTRODUCTION.....	1
I.1. Background.....	1
I.2. Problem Statement.....	2
I.3. Objectives and Purpose of the Research.....	5
II. BACKGROUND THEORY AND EQUATIONS.....	7
II.1. Detonation Theory.....	7
II.1.1. The Hugoniot Curve.....	9
II.1.2. C-J Detonation Wave Speed.....	12
II.2. Chemical Model and Reaction Kinetics.....	13
III. COMPUTATIONAL SOLUTION OF THE PROBLEM.....	19
III.1. Pulse Detonation Engine Geometry.....	19
III.2. Grid Generation.....	20
III.2.1. Cases I, II, and II Grid Resolution.....	20
III.3. Boundary Conditions.....	23
III.3.1. PDE Block.....	23
III.3.2. Exterior Block.....	24
III.4. Initial Conditions.....	26
III.5. CFD Conditions.....	26
IV. RESULTS AND DISCUSSIONS.....	28
IV.1. Shock Tube Results.....	28
IV.2. Case I .....	29

IV.2.1. Centerline Pressure, Temperature and Molecular Composition.....	30
IV.2.2. Centerline Pressure and Velocity.....	39
IV.2.3. Pressure Contours.....	43
IV.2.4. Case I Results Discussion.....	45
IV.3. Case II .....	47
IV.3.1. Centerline Pressure, Temperature and Molecular Composition .....	47
IV.3.2. Centerline Pressure and Velocity.....	57
IV.3.3. Pressure Contours.....	61
IV.3.4. Case II Results Discussion.....	63
IV.4. Case III.....	67
IV.4.1. Centerline Pressure and Temperature.....	67
IV.4.2. Case III Results Discussion.....	70
IV.5. Detonation Wave Speed.....	71
IV.6. Results Comparison.....	74
V. HIGH ORDER EXTRAPOLATION .....	76
V.1. High Order Extrapolation Scheme Derivation.....	76
V.2. Test Case.....	81
VI. CONCLUSIONS AND RECOMMENDATIONS.....	83
VII. REFERENCES.....	85

## NOMENCLATURE

*A* area

*atm* atmospheres

$C_i$  concentration of species *i*

$\rho$  density

*K* Kelvin

*c* local speed of sound

$\dot{m}$  mass flow rate

*m* meters

$[X_i]$  Molar fraction of specie *i*

$M_i$  Molecular Concentration

$MW$  Molecular Weight

*Pa* Pascals

*P* pressure

*Z* species concentration conversion factor

*I<sub>sp</sub>* Specific Impulse

$\nu$  stoichiometric coefficients

*T* temperature

$R_u$  Universal gas constant

*u* velocity in the *x*- direction

*v* velocity in the *y*- direction

*w* velocity in the *z*- direction

## LIST OF FIGURES

Figure I.1: Ideal Pulse Detonation Engine Cycle.....	2
Figure II.1: Stationary 1D Combustion Wave.....	7
Figure II.2: Detonation wave in laboratory coordinate system.....	11
Figure III.1: Pulse Detonation Engine Profile.....	20
Figure III.2: Dimensions for Computational Blocks .....	21
Figure III.3: 3D Modeling of Pulse Detonation Engine using GRIDGEN.....	22
Figure III.4: Faces for the PDE computational block.....	24
Figure III.5: Faces for the Exterior computational block.....	25
Figure IV.1: Centerline Pressure and Temperature at $t = 1\mu\text{sec}$ .....	33
Figure IV.2: Molecular Composition at $t = 1\mu\text{sec}$ .....	33
Figure IV.3: Centerline Pressure and Temperature at $t = 0.12\text{ msec}$ .....	34
Figure IV.4: Molecular Composition at $t = 0.12\text{ msec}$ .....	34
Figure IV.5: Centerline Pressure and Temperature at $t = 0.24\text{ msec}$ .....	35
Figure IV.6: Molecular Composition at $t = 0.24\text{ msec}$ .....	35
Figure IV.7: Centerline Pressure and Temperature at $t = 0.36\text{ msec}$ .....	36
Figure IV.8: Molecular Composition at $t = 0.36\text{ msec}$ .....	36
Figure IV.9: Centerline Pressure and Temperature at $t = 0.55\text{ msec}$ .....	37
Figure IV.10: Molecular Composition at $t = 0.55\text{ msec}$ .....	37
Figure IV.11: Centerline Pressure and Temperature at $t = 1.5\text{ msec}$ .....	38
Figure IV.12: Centerline Pressure and Velocity at $t = 1\mu\text{sec}$ .....	40
Figure IV.13: Centerline Pressure and Velocity at $t = 0.12\text{ msec}$ .....	40

Figure IV.14: Centerline Pressure and Velocity at $t = 0.24$ msec.....	41
Figure IV.15: Centerline Pressure and Velocity at $t = 0.36$ msec.....	41
Figure IV.16: Centerline Pressure and Velocity at $t = 0.55$ msec.....	42
Figure IV.17: Pressure Contour at $t = 1\mu\text{sec}$ .....	43
Figure IV.18: Pressure Contour at $t = 0.12$ msec.....	43
Figure IV.19: Pressure Contour at $t = 0.24$ msec.....	44
Figure IV.20: Pressure Contour at $t = 0.36$ msec.....	44
Figure IV.21: Pressure Contour at $t = 0.55$ msec.....	45
Figure IV.22: Centerline Pressure and Temperature at $t = 1\mu\text{sec}$ .....	51
Figure IV.23: Molecular Composition at $t = 1\mu\text{sec}$ .....	51
Figure IV.24: Centerline Pressure and Temperature at $t = 0.12$ msec.....	52
Figure IV.25: Molecular Composition at $t = 0.12$ msec.....	52
Figure IV.26: Centerline Pressure and Temperature at $t = 0.24$ msec.....	53
Figure IV.27: Molecular Composition at $t = 0.24$ msec.....	53
Figure IV.28: Centerline Pressure and Temperature at $t = 0.36$ msec.....	54
Figure IV.29: Molecular Composition at $t = 0.36$ msec.....	54
Figure IV.30: Centerline Pressure and Temperature at $t = 0.55$ msec.....	55
Figure IV.31: Molecular Composition at $t = 0.55$ msec.....	55
Figure IV.32: Centerline Pressure and Temperature at $t = 1.5$ msec.....	56
Figure IV.33: Centerline Pressure and Velocity at $t = 1\mu\text{sec}$ .....	58
Figure IV.34: Centerline Pressure and Velocity at $t = 0.12$ msec.....	58
Figure IV.35: Centerline Pressure and Velocity at $t = 0.24$ msec.....	59
Figure IV.36: Centerline Pressure and Velocity at $t = 0.36$ msec.....	59

Figure IV.37: Centerline Pressure and Velocity at $t = 0.55$ msec.....	60
Figure IV.38: Pressure Contour at $t = 1\mu\text{sec}$ .....	61
Figure IV.39: Pressure Contour at $t = 0.12$ msec.....	61
Figure IV.40: Pressure Contour at $t = 0.24$ msec.....	62
Figure IV.41: Pressure Contour at $t = 0.36$ msec.....	62
Figure IV.42: Pressure Contour at $t = 0.55$ msec.....	62
Figure IV.43: Centerline Pressure and Temperature at $t = 1\mu\text{sec}$ .....	67
Figure IV.44: Centerline Pressure and Temperature at $t = 0.12$ msec.....	68
Figure IV.45: Centerline Pressure and Temperature at $t = 0.24$ msec.....	68
Figure IV.46: Centerline Pressure and Temperature at $t = 0.36$ msec.....	69
Figure IV.47: Centerline Pressure and Temperature at $t = 0.55$ msec.....	69
Figure V.1: Adjacent computational cells with their respective index.....	76

## LIST OF TABLES

Table II.1: Typical properties across a detonation and a deflagration.....	8
Table II.2: Comparison of Experimental Detonation Wave velocity with C-J Theory Detonation Wave Velocity.....	13
Table II.3: Kinetic Mechanism for H <sub>2</sub> – Air according to Jachimowski.....	14
Table IV.1. Shock Tube Analytical Results.....	29
Table IV.2: Detonation Wave Velocity and Mach Number.....	71
Table IV.3: Comparison of Case II Results with other Computational and Experimental Results.....	74
Table V.1: Expanded operators with appropriate number of terms.....	79
Table V.2 Finite Difference Operators expanded.....	80
Table V.3 Test Matrix for High Order Extrapolation Scheme.....	82

# I.INTRODUCTION

## I.1 Background

Pulse Detonation Engines (PDEs) have come into the focus of the propulsion research community in recent years as a possible means to reach high supersonic speeds in atmospheric flight, for orbit insertion, large stand-off weapon delivery, or even intercontinental passenger service. Some competing concepts include supersonic combustion ramjets, or “scramjets”, and rockets. Scramjet technology is in an embryonic stage of development. Rocket propulsion is inherently inefficient, as it requires an oxidizer, as well as a fuel, to be carried on board of vehicle. In addition, a PDE does not need any rotating machinery such as a compressor or a turbine, which makes the engine simple and lightweight.

PDE research programs are being sponsored by ONR, Air Force, NASA, and DARPA, among other agencies, both domestic and foreign [2]. NASA Glenn Research Center is particularly involved in PDE research through its Pulse Detonation Engine Technology project, and has formed several partnerships with universities and industry to evaluate the application of PDE technology to hybrid subsonic and supersonic gas turbine engines for commercial and military applications and combined cycle propulsion systems for access to space applications [3]. General Electric, and Pratt and Whitney have well-established PDE research programs [4].

The fundamental difference between PDEs and all other forms of airbreathing and rocket propulsion is the speed of the combustion wave. A detonation moves at supersonic speeds, producing a shock wave and a pressure gain.



Deflagrations, which occur in other propulsion systems, are subsonic constant pressure processes. The pressure gain from the shock wave makes PDEs more efficient in theory.

## I.2 Problem Statement

The operation cycle of a PDE is analogous to that of an internal combustion engine. This operating cycle is depicted in the figure below.

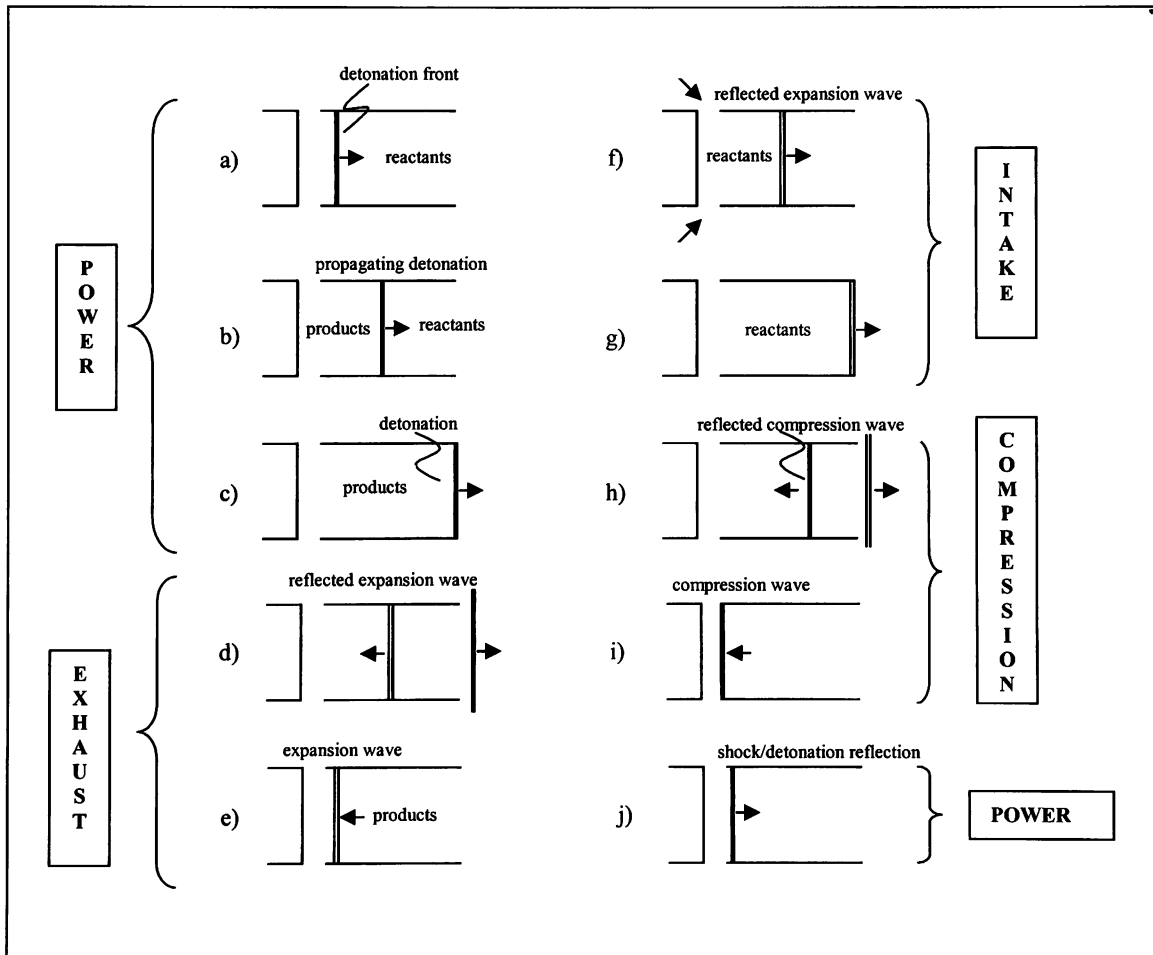


Figure I.1 Ideal Pulse Detonation Engine cycle

The power cycle is equivalent to that shown in figures I.1a through I.1c, in which a detonation wave travels through a detonation tube filled with fuel and an oxidizer (Oxygen, air, etc). Upon the detonation reaching the exit, the exhaust cycle starts with an expansion wave reflecting back into the tube and traveling through the burned gases (Figures I.1e-I.1d).

Upon reflecting from the back wall of the tube, the expansion wave draws a fresh charge of fuel and air into the tube, completing the intake process (Figures I.1f-I.1g). The compression process starts when the expansion wave reflects from the ambient conditions at the exit, as a shock wave, and travels back into the tube, compressing the fuel and air mixture (Figures I.1h-I.1i). The reflected shock wave further compresses and heats the mixture, initiating combustion, and the cycle repeats.

Although PDEs are more efficient in theory than other types of airbreathing propulsion, sustained operation is difficult to obtain. It is a well-known experimental result that detonations tend towards the upper Chapman-Jouguet point on the Hugoniot curve [7]. This means that strong supersonic waves, which are desired, tend to weaken to the sonic limit. In order to avoid having to “overdrive” the detonation with timed bursts from a rocket-like combustor behind the back wall of the PDE, an easily detonable mixture should be achieved.

Another problem is the need to use intake valves to close off the forward end of the combustor on detonation, and then to open and draw a fresh air charge to initiate another detonation and make the engine cycle continuously. Usually rotating valves are used for their relative longevity in this harsh environment. Thus, timing and appropriate mixture amount of fuel and oxidizer is to be well understood.

In actual laboratory PDE experiments it is very important to adequately mix the fuel and oxidizer and turbulence producing devices have been used to enhance the fuel-air mixing [2].

Perhaps one of the most important issues with PDE research is that of detonation initiation. The amount of energy required and the rate at which it needs to be supplied to initiate a detonation in hydrocarbon-air,  $H_2-O_2$ , and  $H_2$ -Air mixtures is impractical [2] [11]. In a laboratory environment, if the energy input is insufficient for direct detonation initiation, a process called DDT (Deflagration to Detonation Transition) can be used. DDT is the process by which a flame can be generated and under appropriate conditions a high speed flame or deflagration could transition to a detonation.

In numerical simulations however, it is possible to directly initiate a detonation by means of a “computational spark”, which is a narrow region within the PDE computational grid, usually near the wall, with high pressure and temperature. Once again though, attention should be paid to the right set of initial conditions and the grid cell width to obtain an actual detonation. Generally, the accuracy of these numerical results depends on a number of factors such as the fidelity of the physical and chemical model on which the equations are based on, the accuracy of the solution algorithm, the numerical resolution used, as well as the initial and boundary conditions [2].

Performance parameters of a single cycle PDE such as Specific Impulse ( $I_{sp}$ ) have been measured in both numerical and laboratory experiments. Two factors that seem to influence this  $I_{sp}$  are how much of the PDE is actually filled up with reactants and whether a nozzle is used at the end of the PDE tube [2].

It is still not certain whether a nozzle (convergent or divergent) at the end of the PDE increases the impulse of the engine or not.

### **I.3 Objectives and Purpose of the Research**

The main purpose of this thesis is to use a first order transient CFD (Computational Fluid Dynamics) code to study the physical and chemical reaction kinetics phenomena occurring on a single-cycle of an ideal Pulse Detonation Engine (PDE). A stoichiometric mixture of Hydrogen ( $H_2$ ) and Oxygen ( $O_2$ ) is used, and the chemical model for the reaction kinetics of the mixture is that of Jachimowski [6] with 6 species and 9 chemical reactions.

The approach is to use a “computational spark”, which is a narrow region within the PDE computational grid close to the wall, to start a detonation. Two sets of initial conditions (pressure and temperature) are tested in two different cases to see which set of conditions generate a detonation wave. To verify that a detonation has formed, a subroutine is implemented within the CFD code to calculate the speed of the wave. Also, the different molar concentration of the products is observed to make sure that the detonation wave is being driven out of the PDE by the reactions occurring behind it. One more simple case is tested with the same initial conditions (pressure and temperature) and stoichiometric gas mixture as one of the previous cases that seemed to form a detonation, but with no chemical reactions occurring.

This simple case is equivalent to that of a “shock tube” and is used to study the effect of the chemical reactions on the speed and strength of the combustion or detonation wave obtained in the previous two chemically reacting cases.

The numerical results of this study are compared to those of He and Karagozian [1] with a similar PDE geometry and chemical mixture. This comparison will show that the CFD code is accurate enough to describe the basic physics and chemical phenomena occurring in a PDE.

Finally, a recommendation is made to implement a set of equations to increase the accuracy of the computer code from “first order” to “sixth order” accurate in space, and to be able to be able to model other phenomena such as Deflagration to Detonation Transition (DDT) and fuel injection in supersonic flow for PDE applications.

## II. BACKGROUND THEORY AND EQUATIONS

### II.1 Detonation Theory

A detonation is generated by the chemical reactions occurring in a premixed gas. In a **detonation**, the combustion wave generated by the chemical reactions is propagating at supersonic speed. Since this combustion wave is propagating supersonically, a shock wave will be formed, driven and sustained by these fast chemical reactions occurring behind it. If the combustion wave generated by the chemical reactions does not propagate supersonically, then the combustion wave is called a **deflagration**. In order to understand the difference in properties behind a detonation and deflagration waves, a one-dimensional steady combustion wave is used. This combustion wave is shown in the following figure.

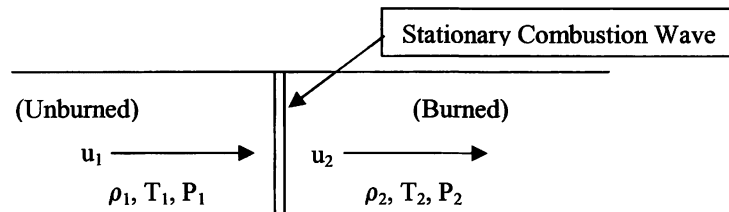


**Figure II.1 Stationary 1D combustion wave**

In Figure 2.0 the unburned gases are moving towards the combustion wave with velocity equal to  $u_1$ . Consider the wave to be stationary. The properties of the burned gases are given with the subscript 2. Typically, the properties ahead and behind deflagration and detonation waves have been reported by Friedman [10], and are shown in Table II.1.

**Table II.1 Typical properties across a detonation and a deflagration**

<b>Property ratio</b>	<b>Detonation</b>	<b>Deflagration</b>
$M_1$	5-10	0.0001-0.03
$M_2$	0.4-0.7 (deceleration)	4-6 (acceleration)
$P_2/P_1$	13-55 (compression)	$\approx 0.98$ (slight expansion)
$T_2/T_1$	8-21 (heat addition)	4-16 (heat addition)
$\rho_2/\rho_1$	1.7-2.6	0.13

As is shown in Table II.1, the Mach number for a detonation is greater than 1, and therefore a shock wave will form. A detonation comprises the interaction between a hydrodynamic process, the shock wave, and a thermochemical process, the combustion [13]. As shown in Table II.1, in both a detonation and a deflagration there is an increase in temperature due to the energy released by the combustion of the mixture.

As shown in Table II.1, one of the main characteristics of the detonation is the significant pressure ratio across the combustion wave. The strength and the speed of the detonation wave are determined by this pressure ratio, and therefore the results in this study will focus on the pressure and temperature behavior across the combustion wave for all of the PDE cases described in the previous section.

## II.1.1 The Hugoniot Curve

In order to understand and explain the basic physics of the detonation phenomenon, a one dimensional analysis - first made by Chapman in 1899 – is presented in this study. The reader is referred to [13] for the assumptions made in this one dimensional analysis. The assumptions made by Chapman, and that are also made in this study, are negligible body forces and adiabatic flow.

First, consider the stationary combustion wave in figure II.1. The three conservation laws and the gas state relationship for this one dimensional flow are presented.

1. **Mass Conservation.** The mass flow rate and mass flux are constant.

$$\frac{\dot{m}}{A} = \rho_1 u_1 = \rho_2 u_2 \quad \text{Equation II.1}$$

where A is the area normal to the x axis.

2. **Momentum Conservation.** The only force acting is the pressure (negligible body forces)

$$P_1 + \rho_1 u_1^2 = P_2 + \rho_2 u_2^2 \quad \text{Equation II.2}$$

3. **Energy Conservation.** The absolute enthalpy is constant.

$$h_1 + \frac{u_1^2}{2} = h_2 + \frac{u_2^2}{2} \quad \text{Equation II.3}$$

The absolute enthalpy in Equation II.3 can be divided into its heat of formation and sensible enthalpy contributions.

$$h(T) = \sum Y_i h_{f,i}^\circ + \sum Y_i \int_{T_{ref}}^T C_{p,i} dT \quad \text{Equation II.4}$$

where the summation is done over all the species  $i$  present in the mixture.



$T_{ref}$  in Equation II.4 is the reference temperature at which the heat of formation is given. The sensible enthalpy is also measured with respect to  $T_{ref}$ .  $T_{ref}$  typically has the value of 298.15 K, the reference value used in the JANAF tables [8]. Assuming constant specific heats and substituting Equation II.4 into II.3, the following relation is obtained.

$$CpT_1 + \frac{u_1^2}{2} + q = CpT_2 + \frac{u_2^2}{2} \quad \text{Equation II.5}$$

where  $q = \sum_{state1} Y_i h_{f,i}^\circ - \sum_{state2} Y_i h_{f,i}^\circ$

**4. State Relationship.** Assuming ideal-gas behavior, the following relationship applies.

$$P_i = \rho_i R_i T_i \quad \text{Equation II.6}$$

where  $R_i = \frac{R_u}{MW_i}$

When the three conservation equations and the state relationship are combined, the following relationship is obtained [13].

$$\frac{\gamma}{\gamma-1} \left( \frac{P_2}{\rho_2} - \frac{P_1}{\rho_1} \right) - \frac{1}{2} (P_2 - P_1) \left( \frac{1}{\rho_1} + \frac{1}{\rho_2} \right) - q = 0 \quad \text{Equation II.7}$$

Equation II.7 is known as the Hugoniot Curve. It gives the properties of the burned gases behind a combustion wave for a given set of initial conditions, pressure ( $P$ ), specific volume ( $1/\rho$ ), and heat addition ( $q$ ). The amount of heat addition depends on the type and stoichiometry of the gas mixture. The geometry of the Hugoniot Curve is depicted in many introductory combustion texts, such as Kuo [7].

The Hugoniot Curve is divided into 5 regions of possible mathematical solutions. The four physically possible regions are for strong, and weak detonations, and deflagrations. There are two points that separate the strong and weak regions for each type of wave. These are called the Chapman-Jouguet (CJ) points. These points are the points of tangency between the Hugoniot Curve and the Rayleigh lines. The Rayleigh lines are derived from the continuity and momentum equations, II.1 and II.2. The reader is referred to Turns [13] for this derivation.

For the strong and weak detonation regions, the Hugoniot curve shows that the pressure of the burned gases behind the combustion wave is significantly higher than the unburned gas pressure. The most apparent difference between a strong and a weak detonation is the pressure of the burned gases. Another difference that is relevant to the present study of detonations for propulsion applications is the Mach number of the burned gas behind the wave. In the previous wave-fixed coordinate system shown in Figure II.1, the Mach number  $M_2$  is greater than unity for a weak detonation, and less than unity for a strong detonation.  $M_2$  is equal to unity at the CJ points. With this in mind, consider now the wave moving through a stationary gas, as shown in the following figure.

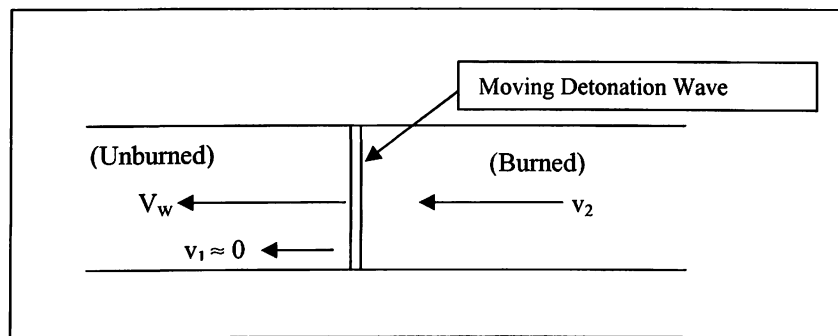


**Figure II.2 Detonation wave in laboratory coordinate system**

In Figure II.2 the detonation wave is moving toward the left with velocity  $V_w$  into stagnant unburned gas. Kuo [7] makes three observations for this moving detonation wave. One is that the Chapman-Jouguet wave is traveling supersonically, as it has been noted. Also the burned gases will move in the same direction as the detonation wave. Finally, the burned gases can not catch up with the wave.

For propulsion applications it is desired to maximize both the pressure and the velocity of the burned gas. A strong detonation's advantage over a weak detonation has been noted for the former. Since  $M_2$ , relative to the wave, is lower for a strong detonation, it seems reasonable that a higher burned gas velocity is also attainable with a strong detonation. The burned gas Mach number in a laboratory fixed coordinate system, as in Figure II.2, will determine if a diverging or converging/diverging nozzle geometry is optimal for propulsion.

### **II.1.2 C-J Detonation Wave Speed**

Knowledge of the detonation velocity is of great importance. There are many methods available for the calculation of C-J detonation wave velocities. Table II.2 shows a comparison of experimental detonation velocity data given by Lewis and Friauf [16] on a stoichiometric mixture of hydrogen and oxygen, and calculated results based on Chapman-Jouguet theory.

**Table II.2 Comparison of Experimental Detonation Wave velocity with C-J Theory**

**Detonation Wave Velocity**

Explosive Mixture	P <sub>2</sub> (atm)	T <sub>2</sub> (K)	$u_1$ (C-J Theory) (m/s)	$u_1$ (expt. [16]) (m/s)	Dissociation (mole %)
(2H <sub>2</sub> + O <sub>2</sub> )	18.0	3583	2806	2819	32

Table II.2 shows that the velocity obtained by the analytical methods is close to the experimental detonation velocity given in Lewis and Freud [16], and thus analytical methods can provide a good approximation when dissociation is taken into account. The constant pressure adiabatic flame temperature for the same explosive mixture, at 18 atm, is 3483 K. The experimental detonation velocity given in Table II.2 seems to be that of a CJ detonation wave, whereas in our study, as shown later, a weak detonation was obtained.

## **II.2 Chemical Model and Reaction Kinetics**

To perform the analysis of the PDE performance a CFD code developed by Perrell [5], to study combustion, reaction kinetics and gas dynamics processes in high speed and propulsive flows will be used.

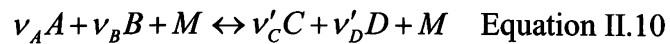
## Finite Rate Chemistry Model

To model the reaction kinetics and the gas dynamics inside the PDE, the combustion modeling is that for an H<sub>2</sub>-O<sub>2</sub> mixture with 6 species and full reaction kinetics according to Jachimowski [6]. These species are OH, H<sub>2</sub>, O<sub>2</sub>, H<sub>2</sub>O, O, and H. The reactions used are the following.

**Table II.3 Kinetic Mechanism for H<sub>2</sub> – Air according to Jachimowski**

Reaction Number	Reaction	$C_r$ (cm <sup>3</sup> /gmol/sec)	$\eta_r$	$E_r/k$ (K)	Reaction Type
1	H <sub>2</sub> + O <sub>2</sub> = OH + OH	1.7E13	0.	24169	Exchange
2	OH + H <sub>2</sub> = H <sub>2</sub> O + H	2.2E13	0.	2593	
3	H + O <sub>2</sub> = OH + O	2.20E14	0.	8459	
4	O + H <sub>2</sub> = OH + H	1.80E10	1.	4481	
5	OH + OH = H <sub>2</sub> O + O	6.3E12	0.	549	
6	H + OH + M = H <sub>2</sub> O + M	2.20E22	-2.	0.	Dissociation and Recombination
7	H + O + M = OH + M	6.00E16	-0.6	0.	
8	H + H + M = H <sub>2</sub> + M	6.40E17	-1.	0.	
9	O + O = O <sub>2</sub> + M	6.00E13	0.	-503	

For a full reaction and non-equilibrium chemically reacting flow consider a set of bi-directional reactions of the form



where  $\nu$  and  $\nu'$  are the stoichiometric coefficients of the reactants and products respectively.  $M$  is a **collision partner**, and could be any molecule.

In recombination reactions, the collision partner is required to carry away the energy liberated in forming the stable species. During collision, the internal energy of the newly formed molecule is transferred to the collision partner,  $M$ , and is manifest as kinetic energy of  $M$ . Without this energy transfer, the newly formed molecule would dissociate back to its constituents species.  $M$  can also have a higher vibrational, rotational, or electronic state, or radiation can be emitted. The rate of production of any chemical specie  $E$  is

$$\frac{\partial \rho_E}{\partial t} = M_E \sum_{r=1}^{nr} (\nu'_E - \nu_E)_r \left\{ k_{fwd} C_A^{\nu_A} C_B^{\nu_B} C_M - k_{bwd} C_C^{\nu_C} C_D^{\nu_D} C_M \right\}_r \quad \text{Equation II.11}$$

where the summation is over all reactions. In equation II.11,  $M_E$  is the molecular mass of specie  $E$ .

The species concentrations  $C$  are

$$C_E = \frac{\rho_E}{M_E} \quad \text{Equation II.11}$$

The forward rate coefficient for reaction  $r$  is

$$k_{fwd,r} = C_r T^{\eta_r} \exp\left(\frac{-E_r}{kT}\right) \quad \text{Equation II.12}$$

In equation II.13,  $C_r$ ,  $\eta_r$ , and  $K_r$  are constants whose values are given in Table II.3.  $E_r$  is called the activation energy and represents the threshold above which a reaction can take place.  $k$  is the Boltzmann's constant and has the value of  $1.38054 \times 10^{-6}$  erg/K. The units for  $k_{fwd_r}$  are  $\frac{cm^3}{gmol.sec}$ .

The backward rate coefficient is

$$k_{bwd_r} = \frac{k_{fwd_r}}{K_{C_r}} \quad \text{Equation II.13}$$

The equilibrium coefficient in terms of the specie concentrations is

$$K_{C_r} = \frac{C_C^{v'_C} C_D^{v'_D} \dots}{C_A^{v'_A} C_B^{v'_B} \dots} \quad \text{Equation II.14}$$

Upon substituting from the equation of state (where pressure is in Pascals), e.g.

$$p_A = C_A R_u T \quad \text{Equation II.15}$$

this becomes

$$K_C = \frac{p_C^{v'_C} p_D^{v'_D} \dots}{p_A^{v'_A} p_B^{v'_B} \dots} (R_u T)^{-\Delta_r v} \quad \text{Equation II.16}$$

where

$$\Delta_r v = v'_C + v'_D + \dots - v_A - v_B - \dots \quad \text{Equation II.17}$$

Noting that the equilibrium coefficient in terms of partial pressures is defined

$$K_{P_r} = \frac{\left(\frac{p_C}{p_0}\right)^{\nu_C} \left(\frac{p_D}{p_0}\right)^{\nu_D} \dots}{\left(\frac{p_A}{p_0}\right)^{\nu_A} \left(\frac{p_B}{p_0}\right)^{\nu_B} \dots} \quad \text{Equation II.18}$$

we can write immediately

$$K_{C_r} = K_{P_r} \left(\frac{p_0}{R_u T}\right)^{\Delta_r \nu} \quad \text{Equation II.19}$$

The reference pressure  $p_0$  is 101,325 Pa, the value used in the JANAF Tables [8].

From these tabulated data, we can compute

$$K_{P_r} = \exp\left(\frac{-\Delta G_{T_r}^0}{R_u T}\right) \quad \text{Equation II.20}$$

The Gibbs energy change is

$$\Delta G_{T_r}^0 = \nu'_C g_C^0 + \nu'_D g_D^0 + \dots - \nu_A g_A^0 - \nu_B g_B^0 - \dots \quad \text{Equation II.21}$$

The standard partial molal Gibbs functions are fit as cubic splines to tabulated functions of temperature given in the JANAF tables [8].

$$g_S^0 = c_{S,1} + c_{S,2} T_{index} + c_{S,3} T_{index}^2 + c_{S,4} T_{index}^3 \quad \text{Equation II.22}$$



$T_{index}$  is the temperature minus the greatest integer multiple of 100 K, since the data are tabulated in 100 K increments.

$$T_{index} = T - 100 \times \text{int}\left(\frac{T}{100}\right)$$

Equation II.23

### III. COMPUTATIONAL SOLUTION OF THE PROBLEM

#### III.1 Pulse Detonation Engine Geometry

The geometry chosen for this computational study is two-dimensional axis-symmetric. The geometry consists of a straight tube, closed in one end and attached to a nozzle at the other. Since the PDE geometry is symmetrical about the x-axis, only the upper half will be considered for this study. The radius and length of the straight section of the PDE are 0.2 m and 1 m, respectively. A divergent nozzle was chosen to be attached to the straight tube because of previous studies that suggest that a divergent nozzle might increase the impulse of the engine, and therefore benefit its performance [9]. The contour of the nozzle is a smooth curve given by the following relation given in terms of areas first [9].

$$A / A_i = 1 ; 0 \leq x / L \leq \delta / L \quad \text{Equation III.1}$$

$$A / A_i = 1 + (AR-1) \sin^n [(\pi/2) (x-\delta)/(L-\delta) ] ; \delta/L < x / L \leq 1 \quad \text{Equation III.2}$$

Where  $L$  is the total length of the PDE, that is, the straight tube and the nozzle.  $L$  is 2 meters.  $\delta$  is the distance along the x- axis at which it is desired to start the divergent nozzle, and in this study it has the value of 1 meter.

$AR$  is the ratio of exhaust to inlet area and it has the value of 4.  $n$  is an integer value and the value of two was chosen to yield cross-sectional profiles with continuous slopes along the PDE and zero slope at the end of the divergent nozzle [9].

The following is a plot of the previous equations.

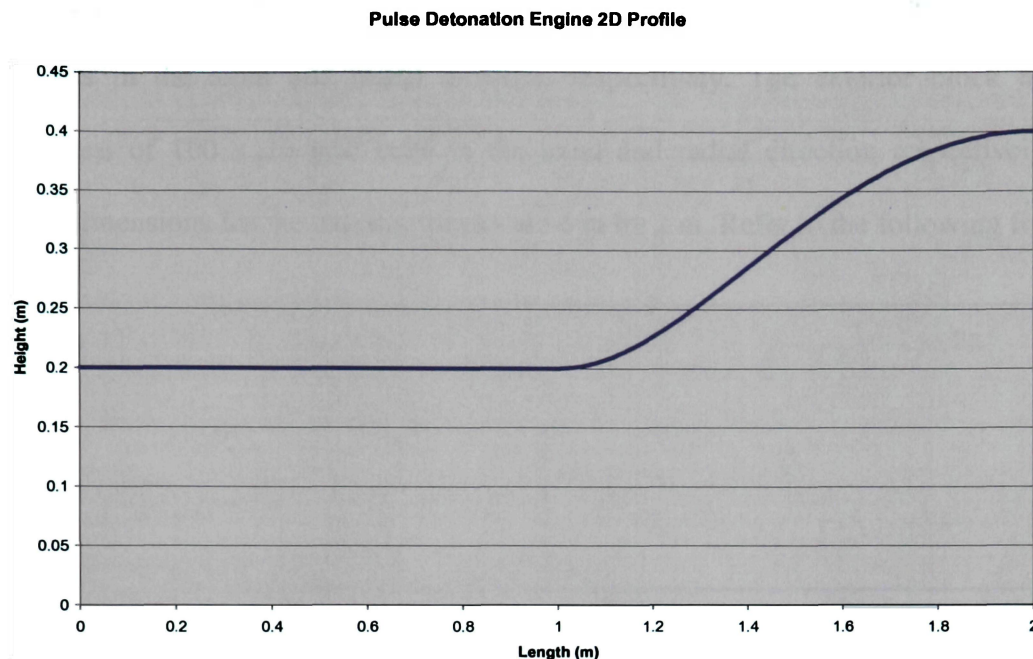


**Figure III.1 Pulse Detonation Engine Profile**

## **III.2 Grid Generation**

The grid for all the computational cases is structured. Even though the study is two-dimensional, the CFD code performs a degenerative three-dimensional analysis and therefore it needs a grid mesh which is also three-dimensional. However, there is only one cell in the  $z$  - direction. As a consequence, a wedge is used for the mesh of the 2D axi-symmetric PDE. The numerical scheme for this type of geometry is a 3D Flux Vector Splitting technique given in [20].

### **III.2.1 Cases I, II, and III Grid Resolution**

For all of the cases studied there were two computational blocks. One of the blocks was the PDE itself, and the other one was an exterior block adjacent to the PDE.

The mesh for the PDE block was structured and had the dimensions of 150 x 6 grid cells in the axial and radial direction respectively. The exterior block had the dimensions of 100 x 26 grid cells in the axial and radial direction respectively. The overall dimensions for the exterior blocks are 6 m by 2 m. Refer to the following figure.

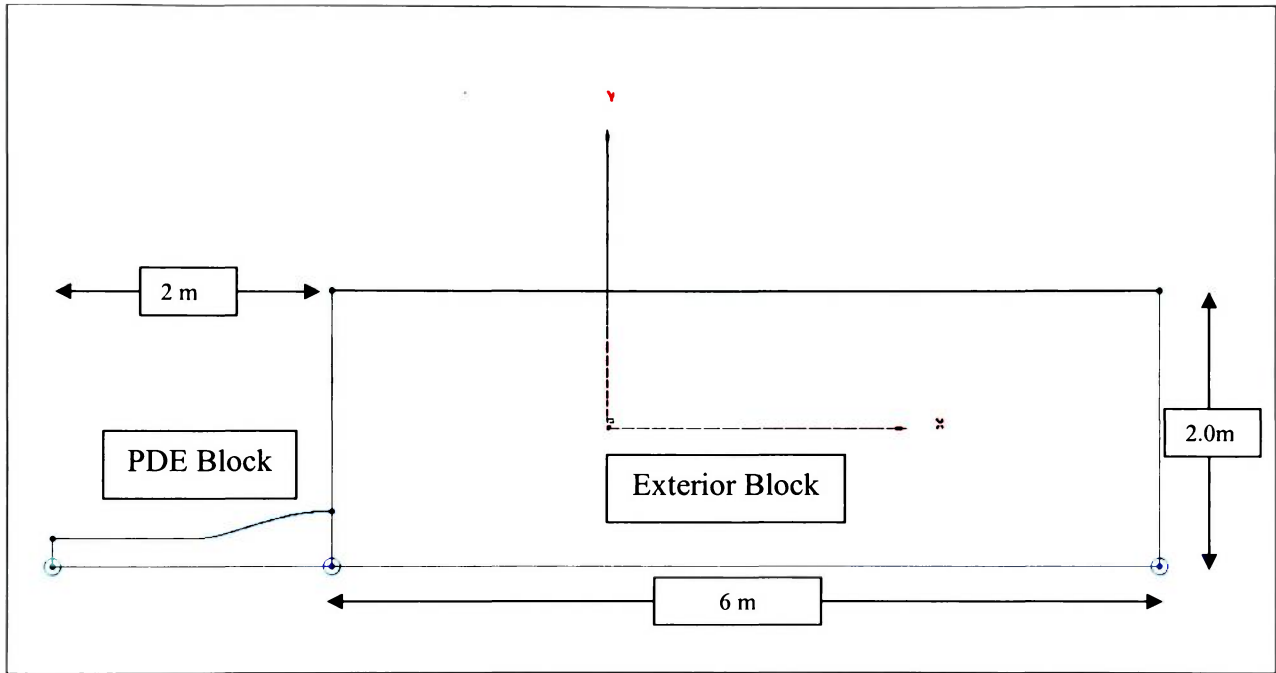


**Figure III.2 Dimensions for Computational Blocks**

In order to obtain the 3D wedge to be used in the computational analysis, the 2D profile shown in Figure III.2. is rotated 5 degrees about the x - axis. The final model is shown in the following figure.

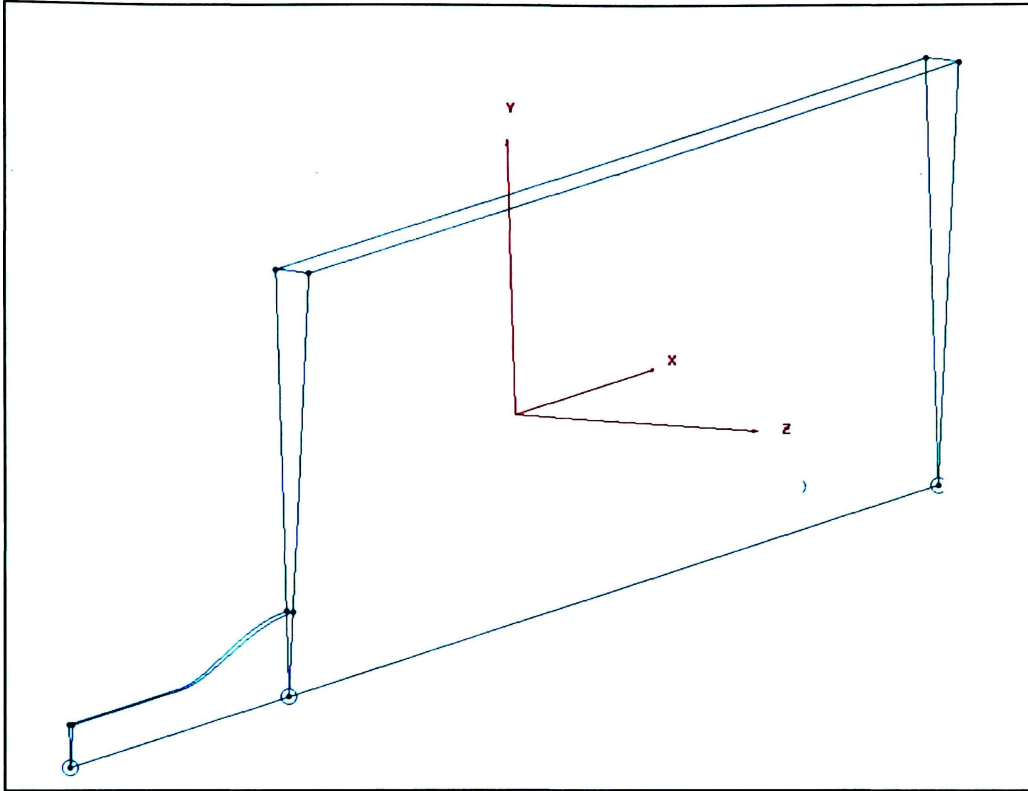


**Figure III.3 3D Geometry and External Flow Field of Pulse Detonation Engine**

### **III.3 Boundary Conditions**

A solid surface is a slip wall condition, in which the velocity parallel to the surface is not zero, and there is no fluxes going in or out of the surface. A communication boundary condition is used at the interface of two blocks and it is used to communicate flux information between the two blocks. A pole boundary condition has zero surface area and does not allow fluxes to go in or out.

#### **III.3.1 PDE Block**

**Face 1:** Solid Surface (Blue)

**Face 2:** Communication Boundary (Opposite to Face 1)

**Face 3:** Solid Surface (Blue)

**Face 4:** Solid Surface (Blue)

**Face 5:** Solid Surface (Opposite to Face 3)

**Face 6:** Pole (Red)

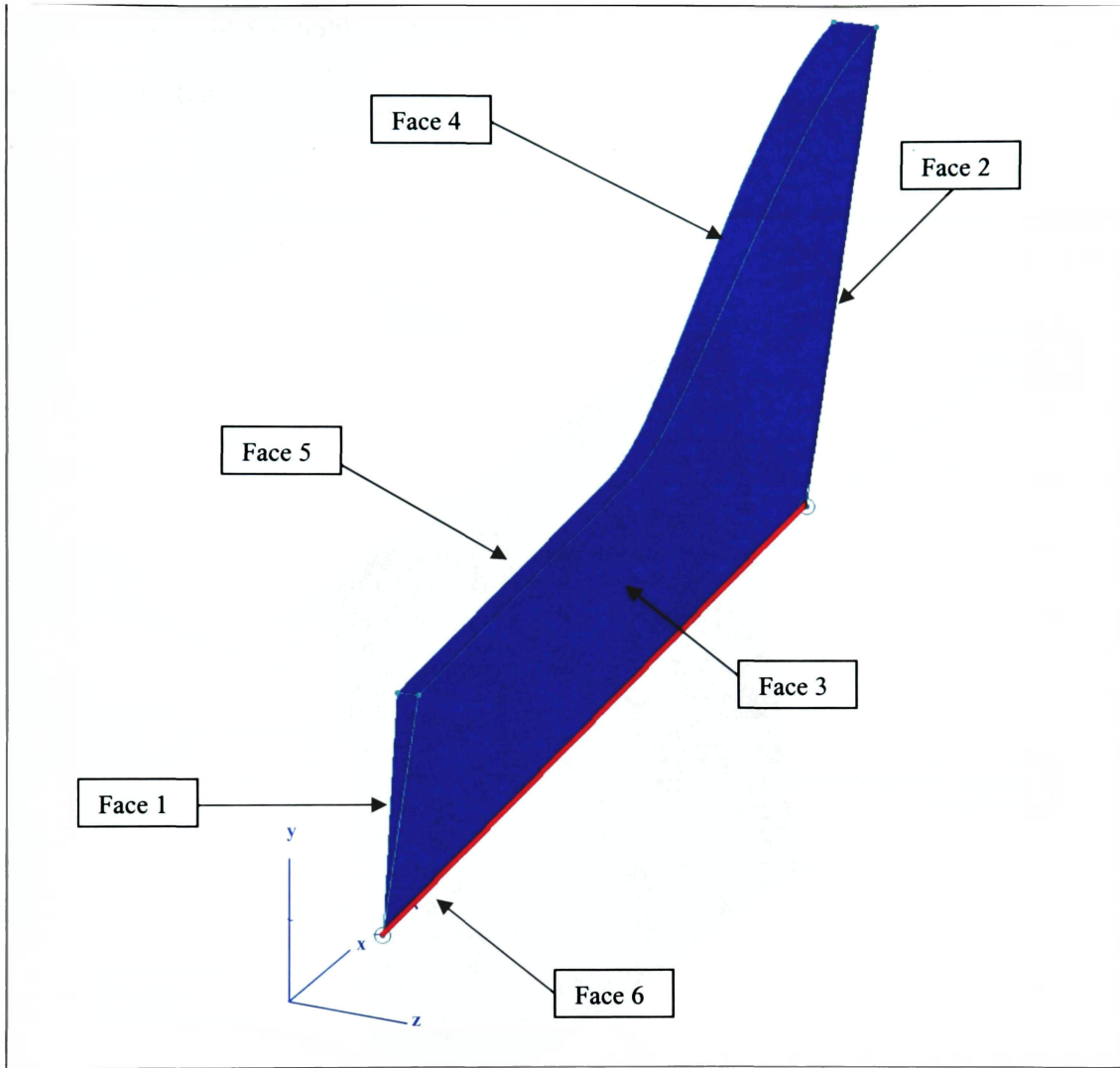


**Figure III.4 Faces for the PDE computational block**

### **III.3.2 Exterior Block**

**Face 1: Communication Boundary (Green)**

**Face 2: Inflow (Yellow)**

**Face 3: Outflow (Opposite to Faces 1 and 2)**

**Face 4: Solid Surface (Blue)**

**Face 5: Solid Surface (Blue)**

**Face 6: Solid Surface (Opposite to Face 4)**

**Face 7: Pole (Red)**

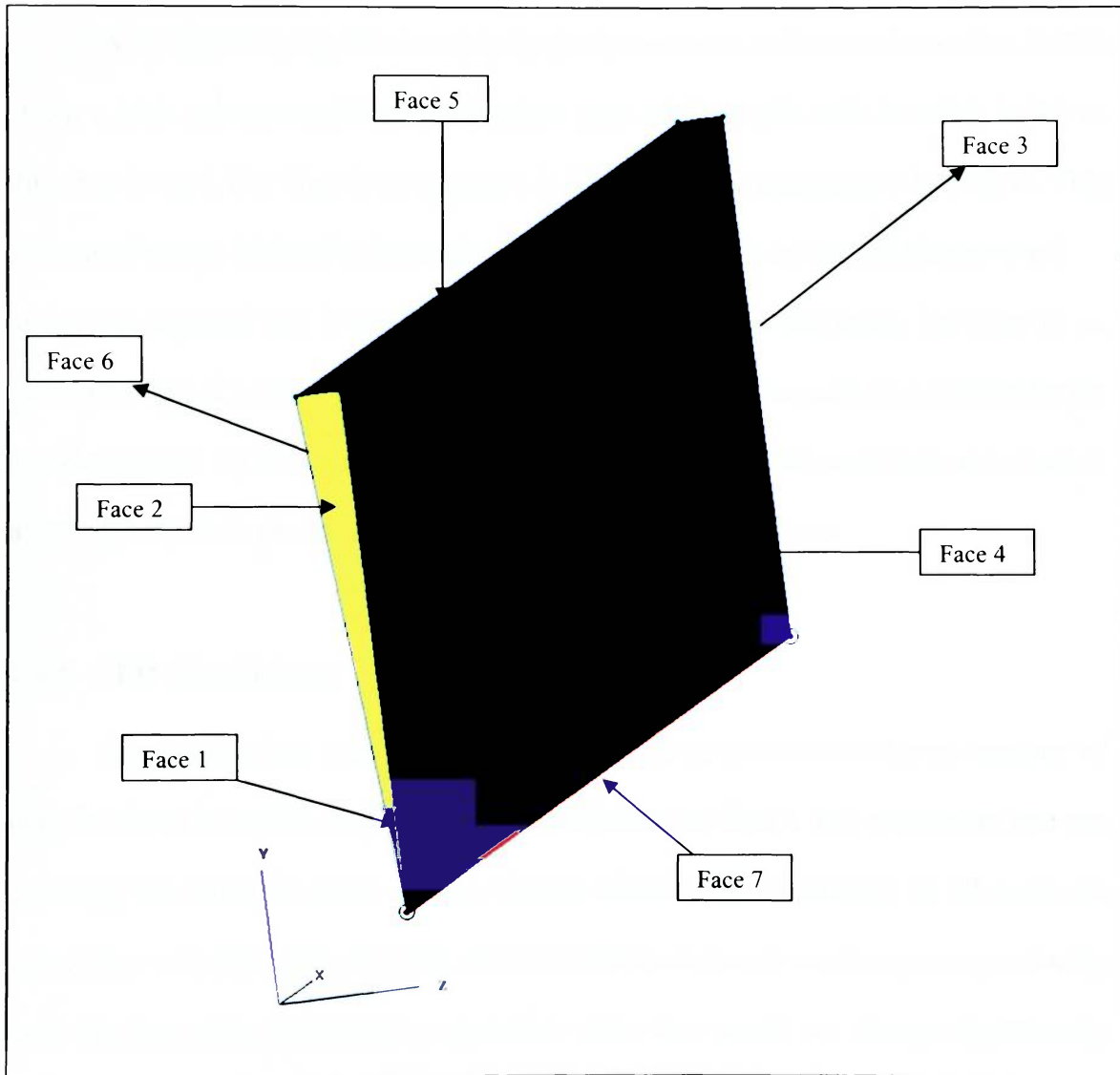


**Figure III.5 Faces for the Exterior computational block**



### **III.4 Initial Conditions**

The entire PDE is initialized with the reactants ( $H_2$  and  $O_2$ ) at atmospheric pressure and temperature, 101.325 kPa, and 300 K respectively, and the mixture is stoichiometric.

A computational spark is used to ignite the reactants and start a detonation. In this study, a high pressure and high temperature zone of three grid cells in width in the x-direction is used. For Case I, the pressure is 20 atm and the temperature is 1500 K. This amount of energy initiated a detonation in the 1D study made by He and Karagozian [11] and it was expected that it would generate the same results in this study. For Case II, an initial pressure of 3 atm and an initial temperature of 2000 K are used as suggested by He and Karagozian [1] in a later study. For Case III, the same initial conditions as in Case II are used, only there are no chemical reactions occurring in this case.

### **III.5 CFD Conditions**

The calculations were done using a CFL (Courant-Friedrich-Levy) number of 0.01 for Cases II and III, and a CFL number of 0.002 for Case I. The calculation was run explicitly for all of the cases and no viscous effects were considered. In all cases the calculation was run using the CFL (Courant-Friedrich-Levy) number given previously until the time step approached a minimum value that would not change significantly iteration after iteration. This minimum value was then taken and wired to the code as a constant time step, and thus, the CFL number was no longer needed. This constant time step ( $\Delta t$ ) was  $0.25 \times 10^{-8}$  sec for Cases II and III, and  $0.5 \times 10^{-9}$  sec for Case I.

The use of a constant time step enabled capturing of “snap shots” of the detonation wave at regular intervals.

## IV. RESULTS AND DISCUSSIONS

### IV.1 Shock Tube Results

Before the results for the computational solution for all cases is discussed, the analytical results for a straight shock tube – resembling the straight tube geometry of the PDE – are presented. These analytical results will help understand the effect of chemical reactions on the strength and velocity of the combustion wave propagating across the PDE.

In a shock tube there are two regions called the driver and the driven section. The driver section is a region of high pressure and temperature gas. The driver and the driven sections are separated by a thin boundary, called a diaphragm. For these analytical results this driver section will have the same values of pressure and temperature as the “computational spark” for Cases I and II. The driven section has a pressure and temperature value of 1 atm and 300 K. The following results assume a shock tube which is closed in one end and open at the other, no chemical reactions, and a calorically perfect gas. The reader is referred to Anderson [18] for a more in depth description of shock tube theory and equations. Note that the shock tube case B with the driver section values for Case II, is the same as the non-reacting computational case (Case III) presented in this study. The results are as follows:

**Table IV.1 Shock Tube Analytical Results**

	<b>Case A</b>	<b>Case B</b>
$P_{\text{driver}}$ (atm)	20	3
$T_{\text{driver}}$ (K)	1500	2000
Shock Pressure Ratio	6.702	2.183
Shock Wave Speed (m/s)	1315.53	768.69

Table IV.1 shows the pressure ratio of the propagating shock wave given the initial pressure in the driver section. As shock tube theory predicts, the pressure ratio across the propagating shock wave is smaller than the initial pressure ratio across the driver and driven section.

## **IV.2 Case I**

As it was described in Section III.2, in Case I the initial conditions at the “computational spark” adjacent to the wall are higher than in Case II. These high pressure and temperature were 20 atm, and 1500 K respectively. The following set of results shown will be plots of the pressure, temperature and molecular composition along the PDE centerline at 6 instants in time, as the shock wave travels through and exits the PDE.

### IV.2.1 Centerline Pressure, Temperature and Molecular Composition

At  $t = 1 \mu\text{sec}$ , Figure IV.1 shows initial pressure and temperature spikes at the wall of the PDE. These values of high pressure and temperature correspond to an initial pressure and temperature ratio of 44.5 and 13.13 respectively, and are much higher than the initial pressure and temperature ratio of 20 and 5. These pressure and temperature spikes are most likely due to the fast chemical reactions occurring behind the forming shock wave. At this point it is expected that this forming shock wave will start moving towards the exit of the PDE and that expansion waves will form and move in the opposite direction. Figure IV.2 shows the chemical reactions occurring due to the high pressure and temperature, and the concentration of the different species near the PDE wall.  $\text{H}_2\text{O}$  or water vapor seems to be produced in larger quantities, with monatomic Oxygen (O) being produced the least.

At  $t = 0.12 \text{ msec}$ s, Figure IV.3 shows a shock wave with pressure and temperature ratios of 10.8 and 11.8 respectively. Note that these ratios are much lower than the initial ratios. This seems to agree with the analytical shock tube results in section IV.1, in which the strength (pressure ratio) of the propagating shock wave is smaller than the initial pressure ratio. Also, as the shock tube results showed, the propagating shock wave should have a pressure ratio of 6.7 with no chemical reactions. Thus, the fact that the pressure ratio across the shock wave in Case I is higher than that of the simple non-reacting shock tube, seems to be due to the effect of chemical reactions. The pressure at the PDE wall has decreased from 45 atm to about 8 atm. Figure IV.3 also show a high pressure and temperature zone trailing the shock wave.

The pressure and temperature profiles in this zone, particularly the increase in pressure at the wall, are caused by reflected expansion waves propagating through the driver section. Because the region used as a “computational spark” was only three grid cells in width in the x- direction and close to the PDE wall, the expansion waves reached the PDE wall almost immediately and started to reflect back towards the PDE exit. The pressure at the wall continuously decreased and the expansion waves, after reflecting back from the wall, will further decrease the pressure of the high pressure zone behind the shock wave. In this high pressure zone trailing the shock wave, there seems to be an overall relative higher concentration of all species (except H<sub>2</sub>O) than in the zone immediately behind the shock wave, as shown in Figure IV.4. This is due to the H<sub>2</sub>O dissociation at the elevated temperature. The pressure ratio across this high pressure and temperature zone is 1.45 with respect to the pressure zone immediately behind the shock wave.

At  $t = 0.24$  msec, Figure IV.5 shows that the shock wave has a pressure ratio of 11.0 and a temperature ratio of about 11.8. These two ratios are very similar to those found at  $t = 0.12$  msec, which seems to indicate that the shock wave is moving across the PDE with an almost constant pressure ratio and strength. As in Figure IV.3, at this particular instant in time, the region of high pressure and temperature is still trailing the shock wave. This high pressure zone seems to be moving at much lower speed than that of the shock wave. However, at  $t = 0.24$  msec, the pressure ratio across the high pressure zone behind the wave has decreased from 1.45 to 1.33. This is the effect of expansion waves described previously reflecting back from the wall. Regarding molecular composition, Figure IV.6 shows there is also a higher concentration of species, except for H<sub>2</sub>O, in the high pressure zone behind the wave.

At  $t = 0.36$  msec, the pressure and temperature ratio across the shock wave in Figure 16.0, is 10.9 and 11.8 respectively. These are similar pressure ratios to those found at  $t = 0.12$ , and  $0.24$  msec. Figure IV.7 also shows that there are two sets of expansion waves traveling in opposite directions. One set is the expansion waves reflected from the PDE wall, and the other set is the expansion waves caused by the shock passing through the divergent nozzle. These expansion waves will most likely reduce the pressure ratio across the high pressure zone of burned gases behind the shock wave. In Figure IV.7 this high pressure zone's pressure ratio has already decreased to 1.28 compared to the previous two instants in time.

At  $t = 0.55$  msec., the shock wave has already exited the PDE tube. Expansion waves are formed at the end of the nozzle and propagate inside, as shown in Figure IV.9. The overall pressure inside the PDE is reduced, specially the pressure in the red zone that was trailing the shock wave. This high pressure zone is, at this instant in time, at the throat of the PDE nozzle. The temperature in this zone is also reduced, although the highest temperature inside the PDE is still in this zone, with a value of 3525 K. Figure 19.0 shows no significant change in the chemical composition of the products as compared with the previous instants of time. The following final figures will show the results a while after the shock has exited the PDE tube and expansion waves have significantly reduced the pressure inside the PDE tube.

Figure IV.11 shows that the pressure inside has decreased due to the reflected expansion waves created by the shock wave exiting the PDE. The minimum pressure inside the PDE at this instant of time is 4.79 atm.

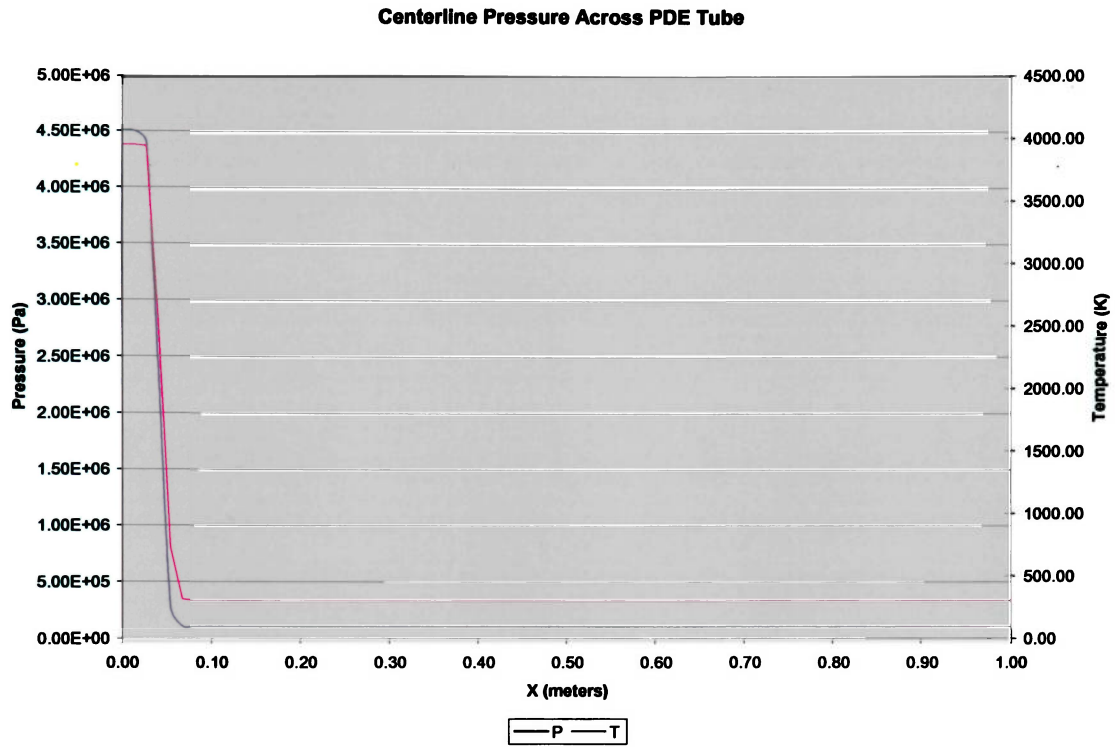


**Figure IV.1 Centerline Pressure and Temperature at  $t = 1 \mu\text{sec}$**

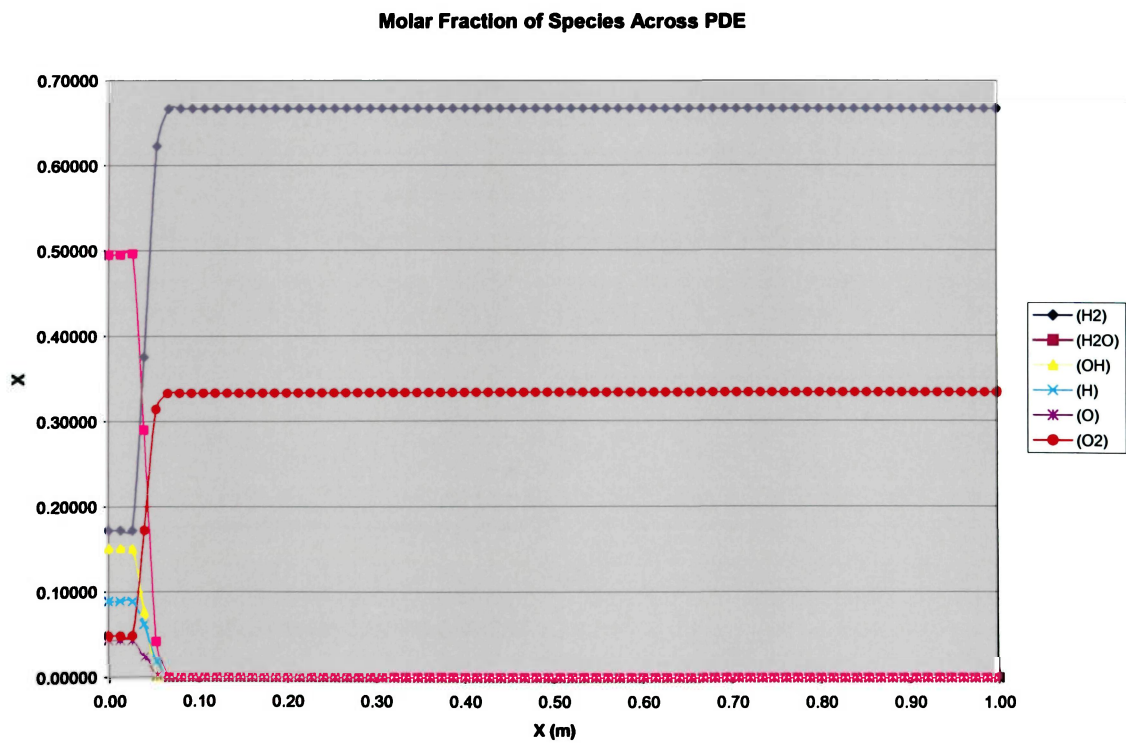


**Figure IV.2 Molecular Composition at  $t = 1 \mu\text{sec}$**



Centerline Pressure Across PDE Tube

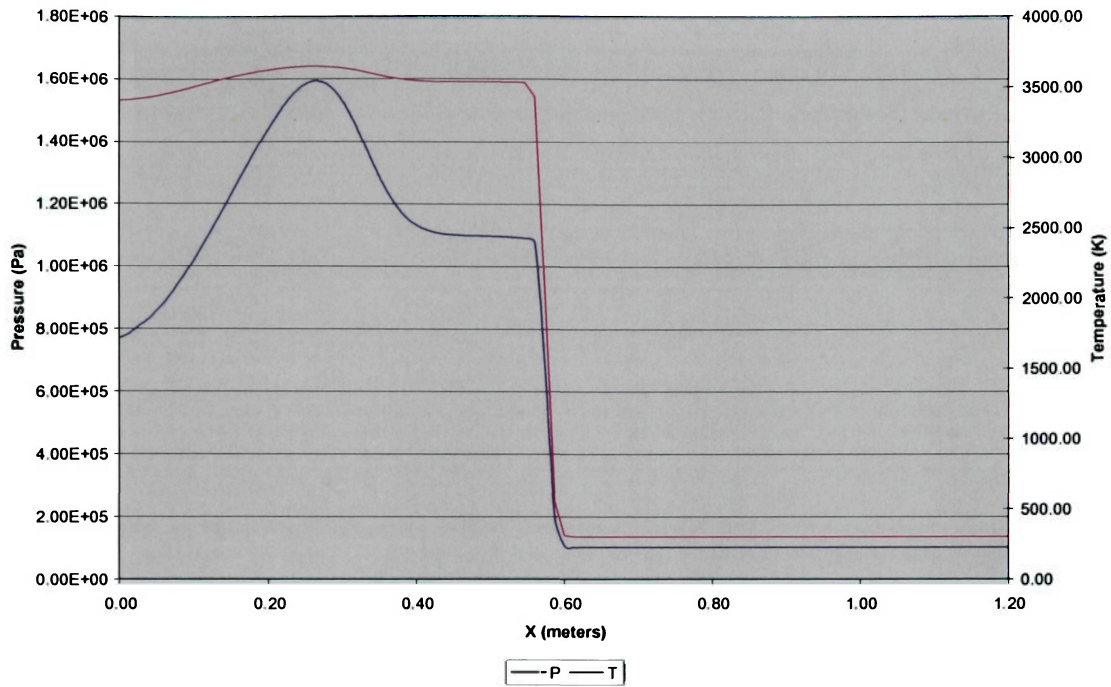


Figure IV.3 Centerline Pressure and Temperature at t = 0.12 msec

Molar Fraction of Species Across PDE

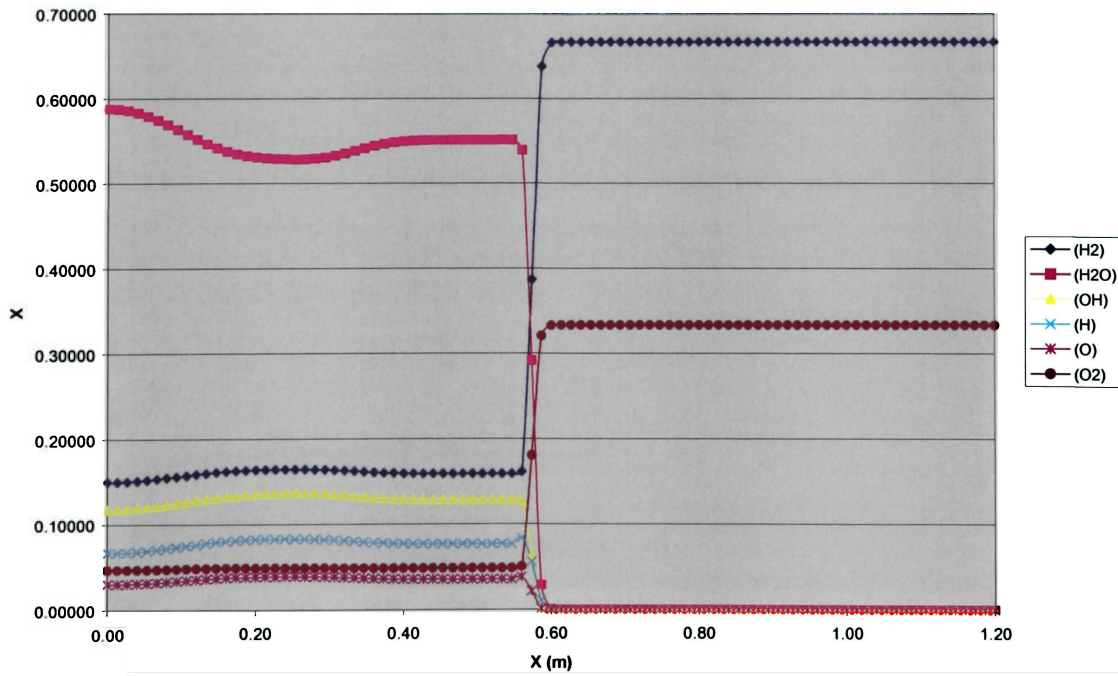
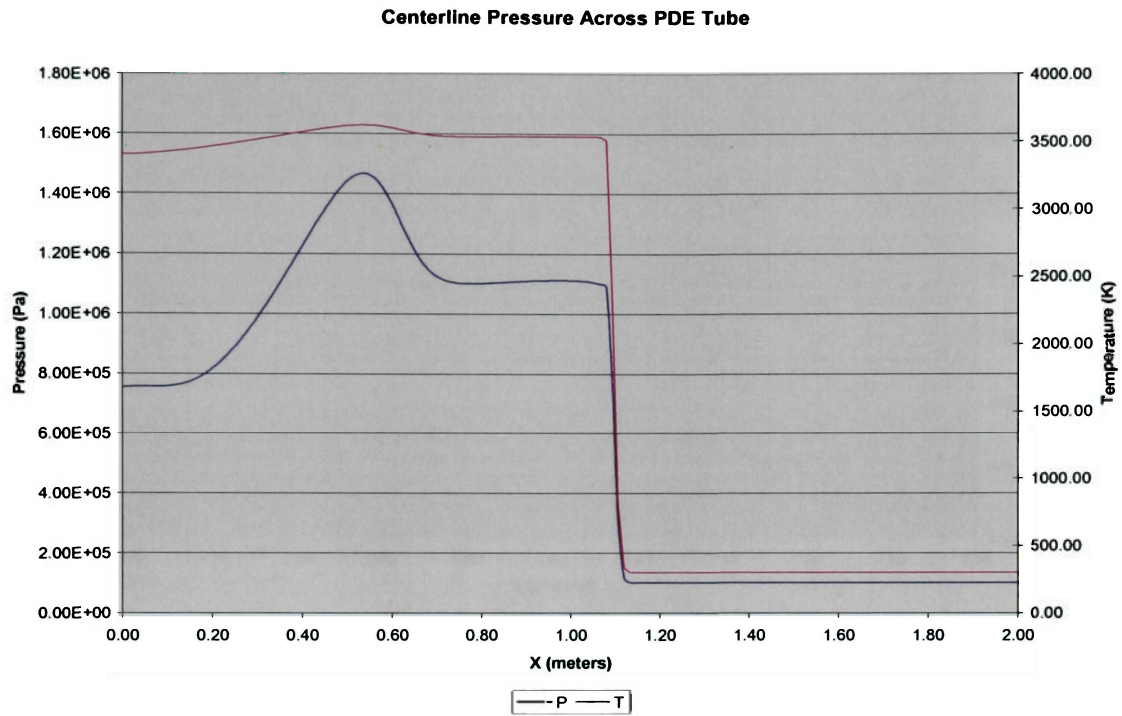
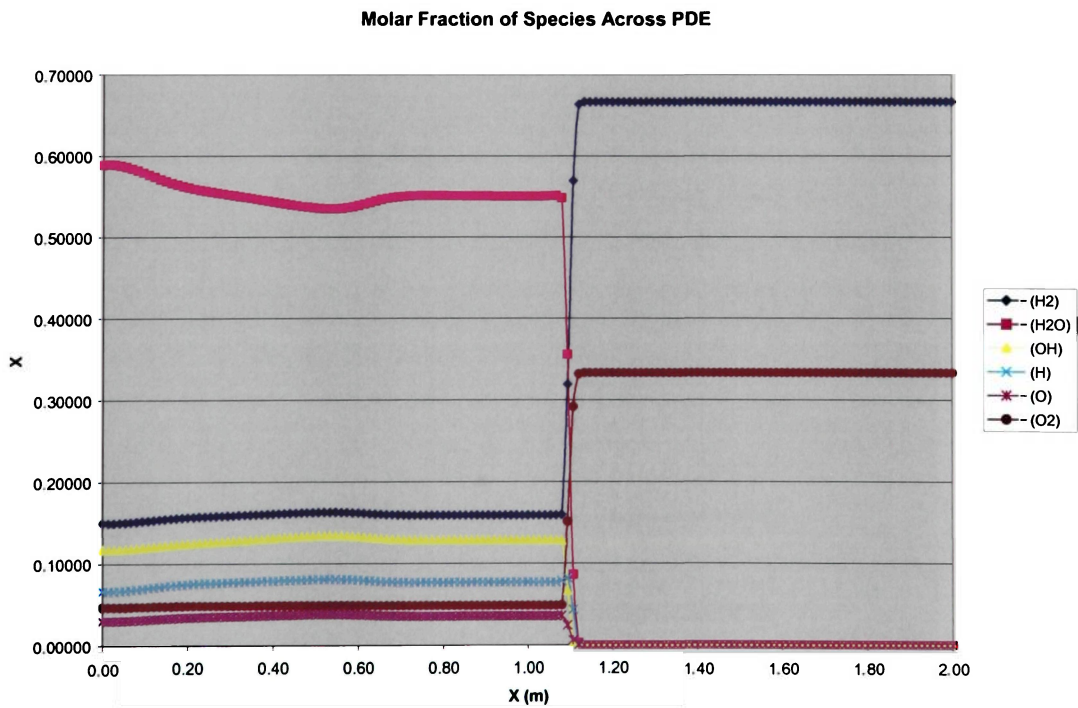


Figure IV.4 Molecular Composition at t = 0.12 msec



**Figure IV.5 Centerline Pressure and Temperature at t = 0.24 msec**



**Figure IV.6 Molecular Composition at t = 0.24 msec**

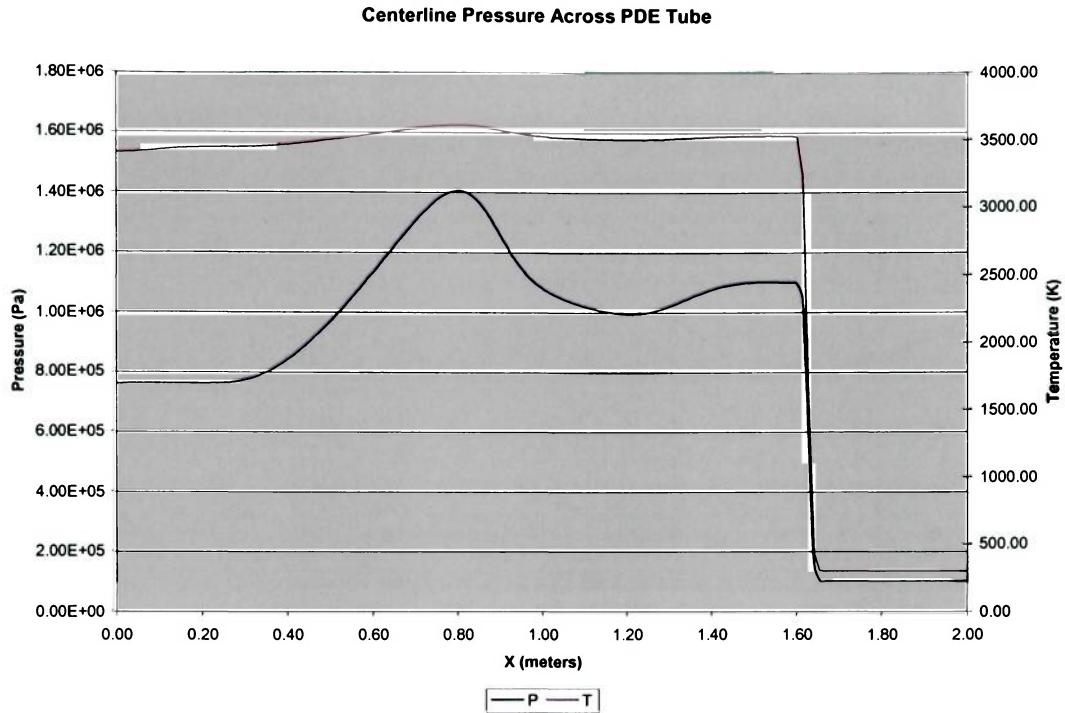


**Figure IV.7 Centerline Pressure and Temperature at t = 0.36 msec.**

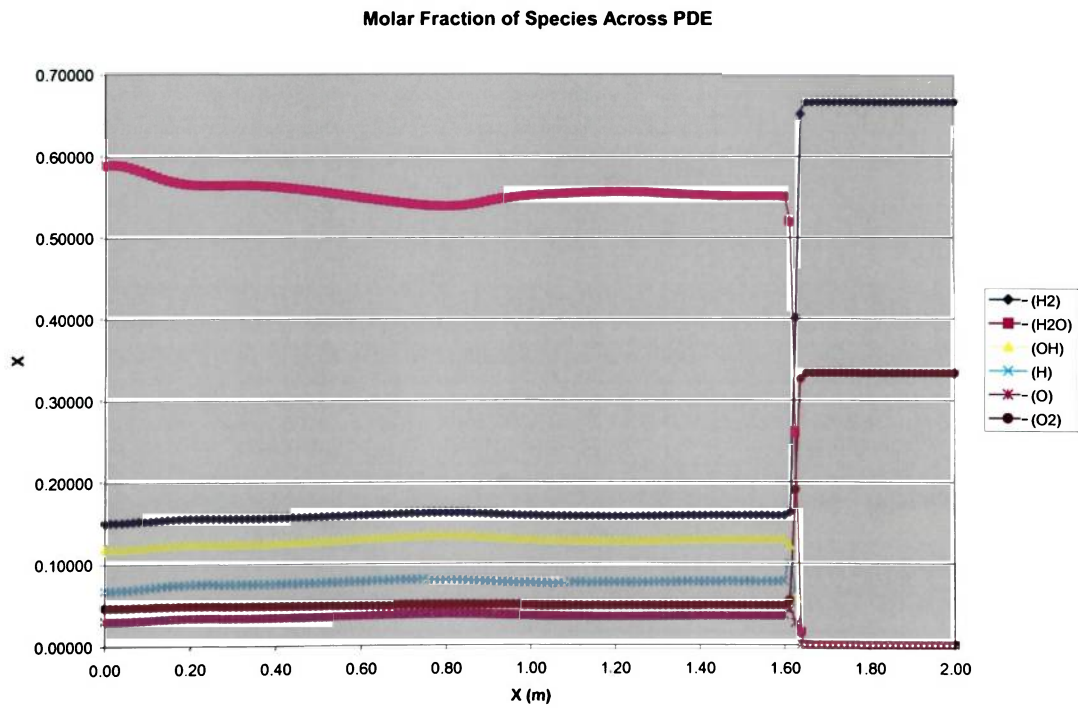


**Figure IV.8 Molecular Composition at t = 0.36 msec.**

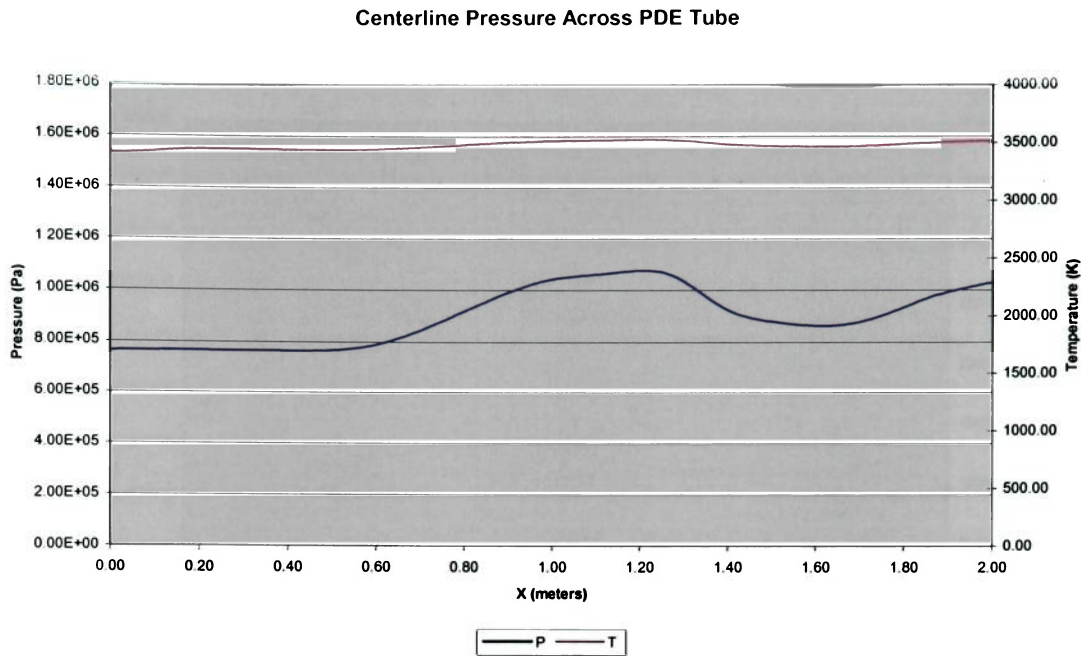


**Figure IV.9 Centerline Pressure and Temperature at t = 0.55 msecs.**

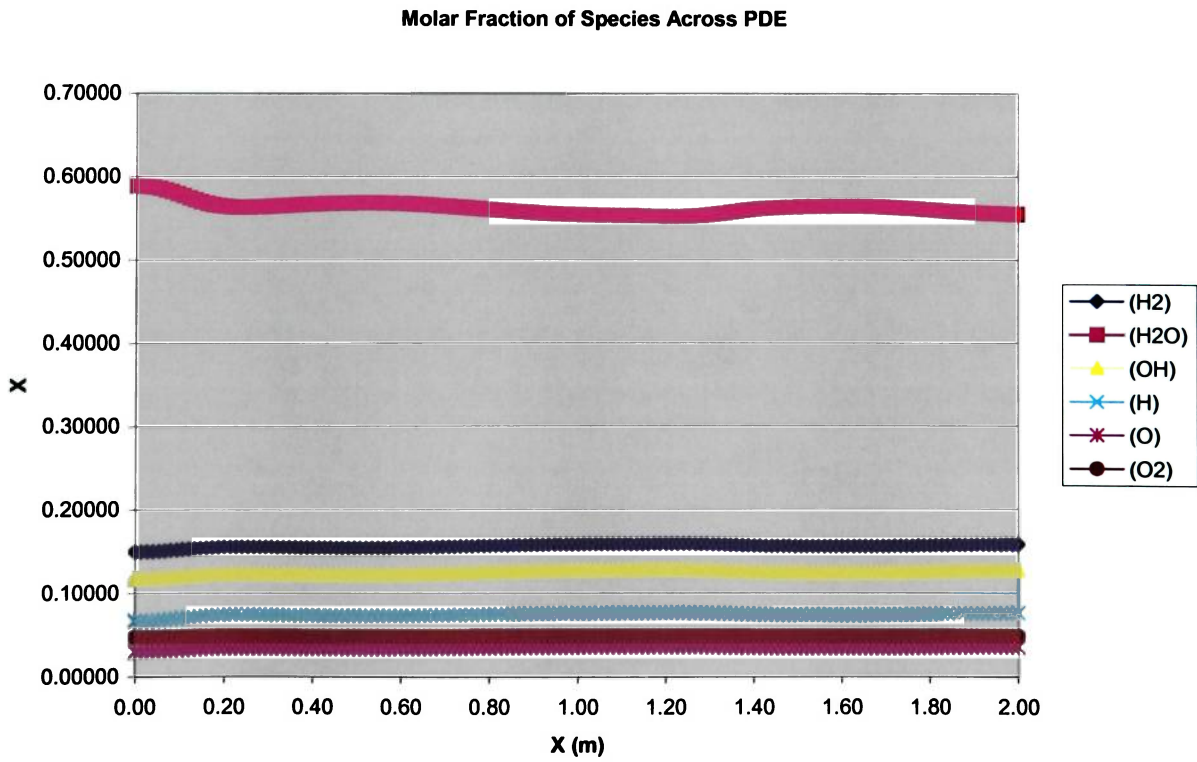


**Figure IV.10 Molecular Composition at t = 0.55 msecs**

**Centerline Pressure Across PDE Tube**

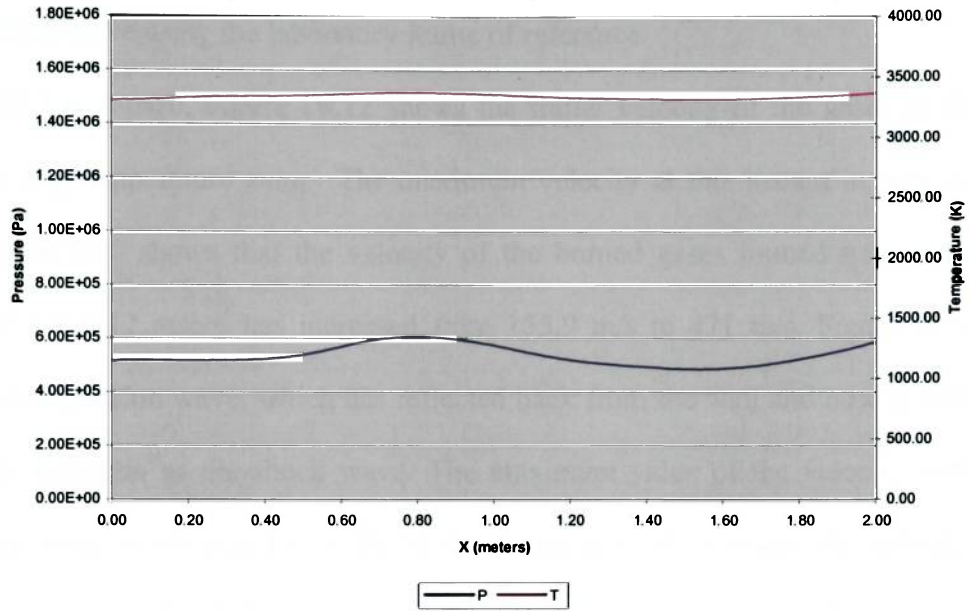


**Figure IV.11 Centerline Pressure and Temperature at t = 1.5 msecs**

## IV.2.2 Centerline Pressure and Velocities

The following figures give the value of the velocity of the gas behind and ahead of the shock wave using the laboratory frame of reference.

At  $t = 1 \mu\text{sec}$ , Figure IV.12 shows the initial velocity of the gases in the high pressure and temperature zone. The maximum velocity at this instant in time is 155.9 m/s. Figure 22.0 shows that the velocity of the burned gases immediately behind the shock at  $t = 0.12 \text{ msec}$ s has increased from 155.9 m/s to 471 m/s. Figure IV.13 also shows an expansion wave, which has reflected back from the wall and now is moving in the same direction as the shock wave. The maximum value of the velocity within the expansion wave is 995 m/s. Figure IV.14 shows that at  $t = 0.24 \text{ msec}$ s, the velocity of the burned gases immediately behind the shock wave has increased and is almost constant at a value of 478 m/s.

Figure IV.15 shows that the velocity of the burned gases has slightly decreased behind the shock wave to 469 m/s. In this figure an expansion wave at the beginning of the divergent nozzle ( $x = 1.0 \text{ m}$ ) is also noticeable. This expansion wave is smaller in magnitude to the expansion wave observed in Figures IV.12-14 and is moving in the opposite direction. Finally Figure IV.16 shows the velocity profile of the burned gas velocity as the shock wave exits the PDE tube. Figures IV.15 and IV.16 show that the velocity of the burned gas velocity behind the wave decreases as the shock wave travels through the nozzle.

Centerline Pressure and Velocity

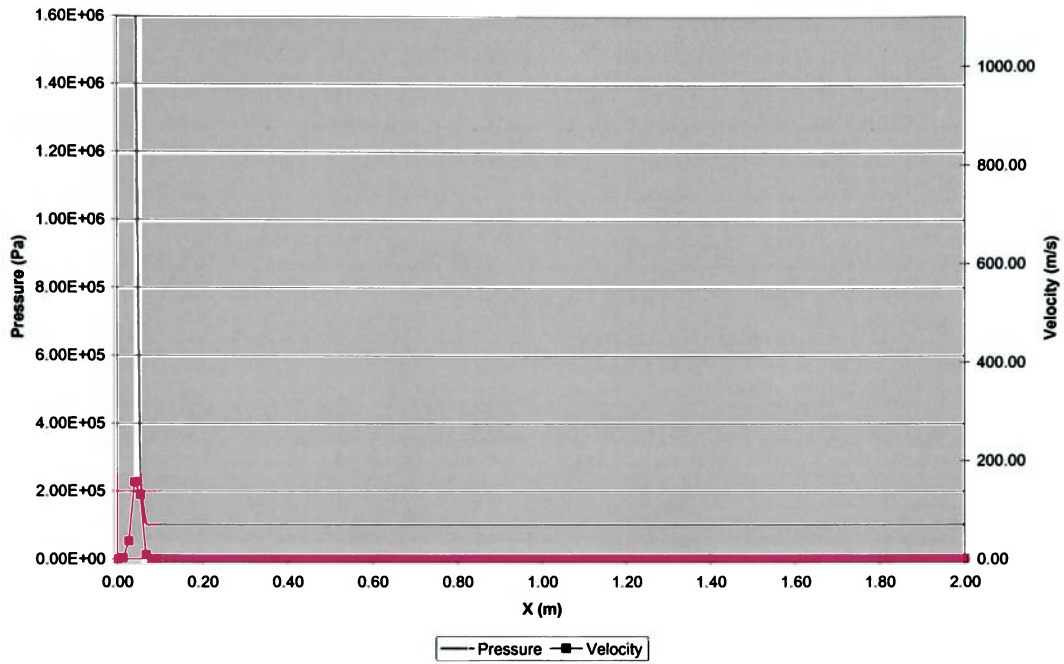


Figure IV.12 Centerline Pressure and Velocity at  $t = 1 \mu\text{sec}$

Centerline Pressure and Velocity

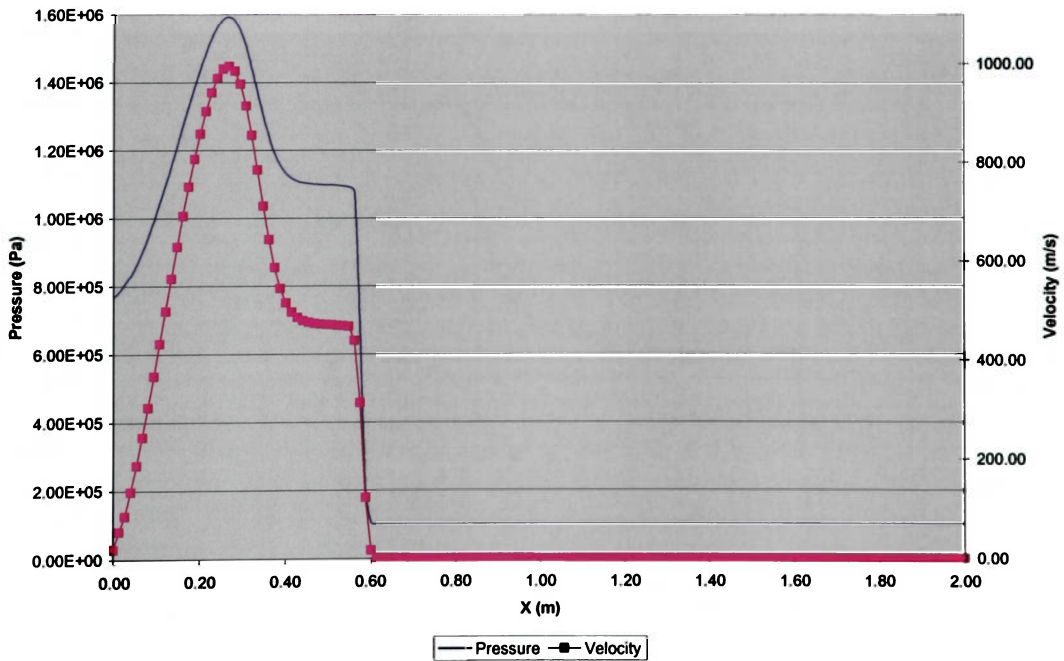
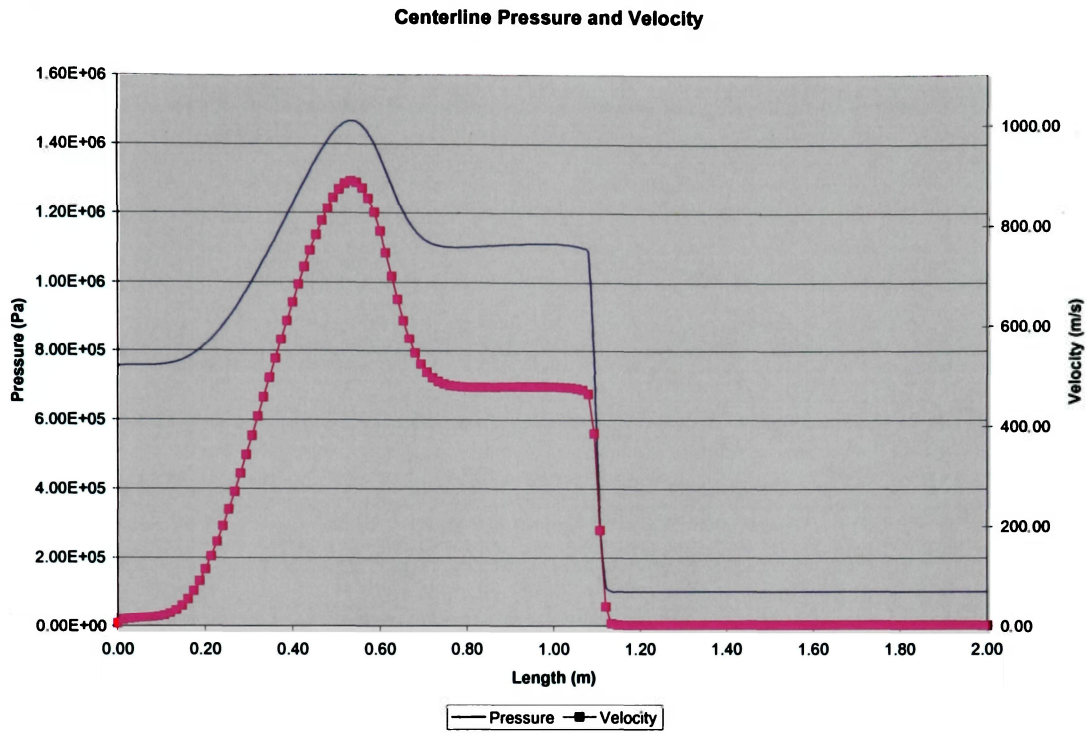
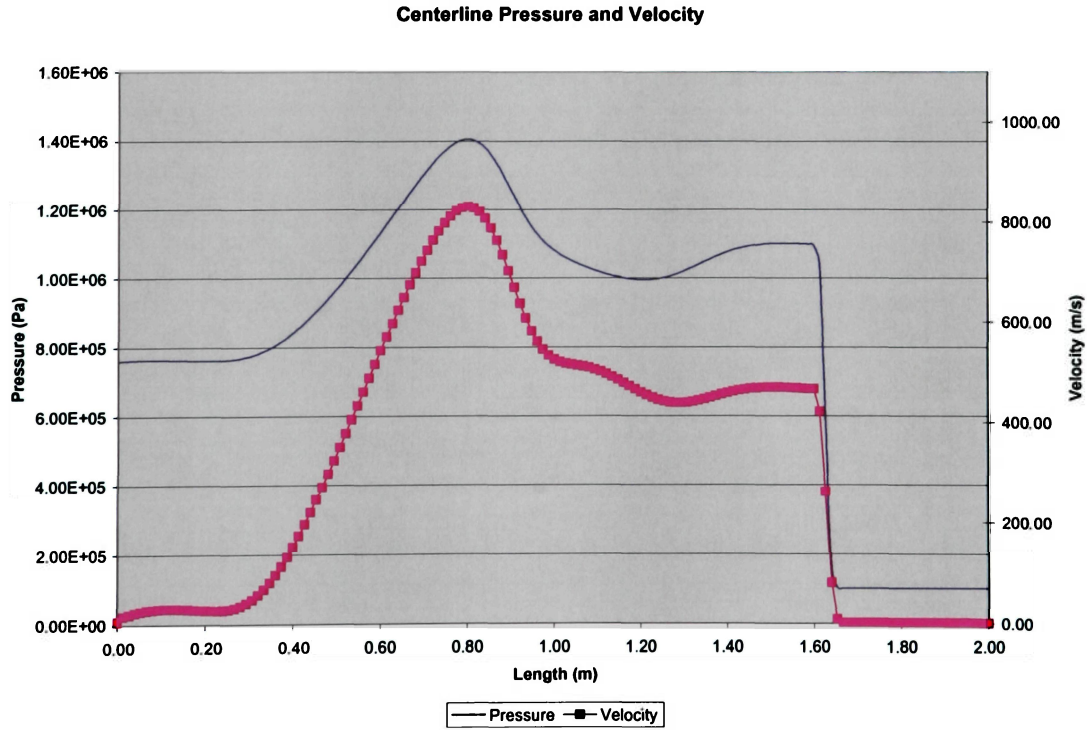


Figure IV.13 Centerline Pressure and Velocity at  $t = 0.12 \text{ msec}$



**Figure IV.14 Centerline Pressure and Velocity at  $t = 0.24$  msec**



**Figure IV.15 Centerline Pressure and Velocity at  $t = 0.36$  msec**



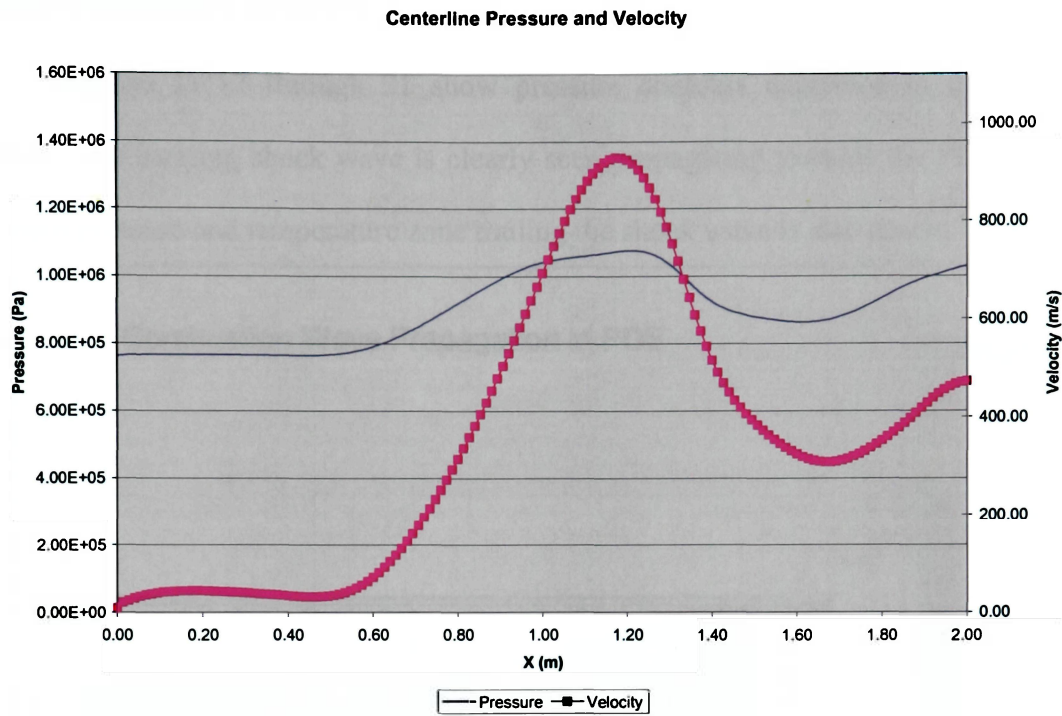


**Figure IV.16 Centerline Pressure and Velocity at t = 0.55 msec**

### IV.2.3 Pressure Contours

Figures IV.17 through 21 show pressure contours described in the previous section. The forming shock wave is clearly seen propagating towards the PDE exit and the high pressure and temperature zone trailing the shock wave is also shown.

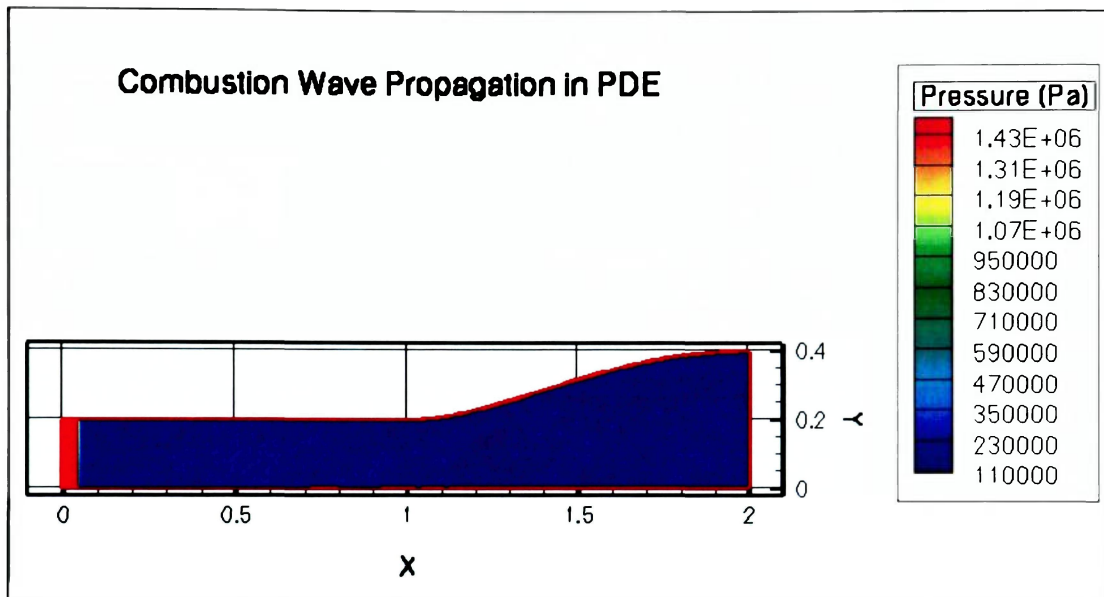


Figure IV.17 Pressure Contours Graph at  $t = 1 \mu\text{sec}$

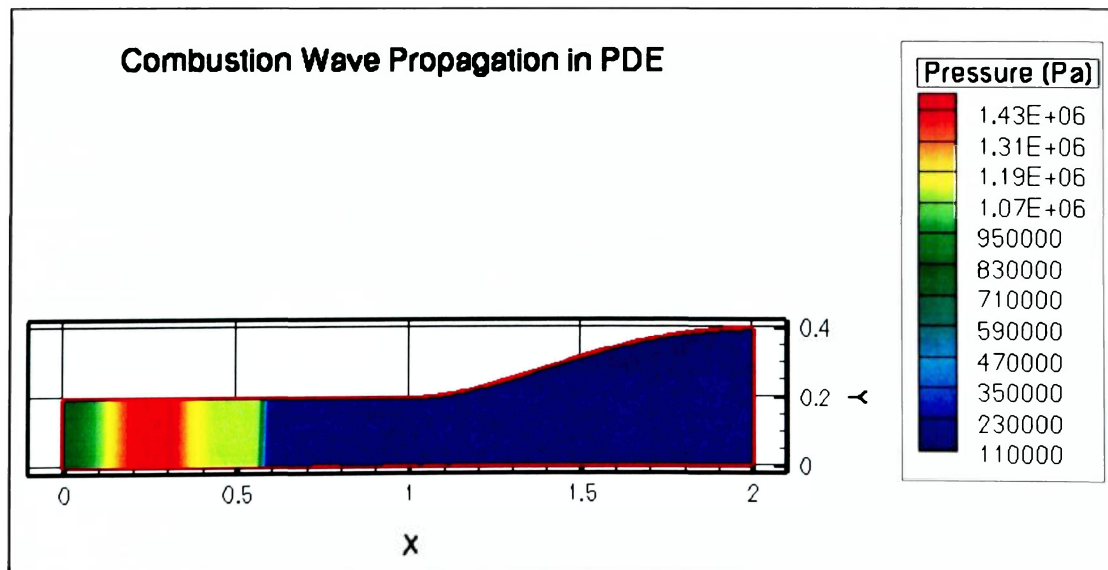
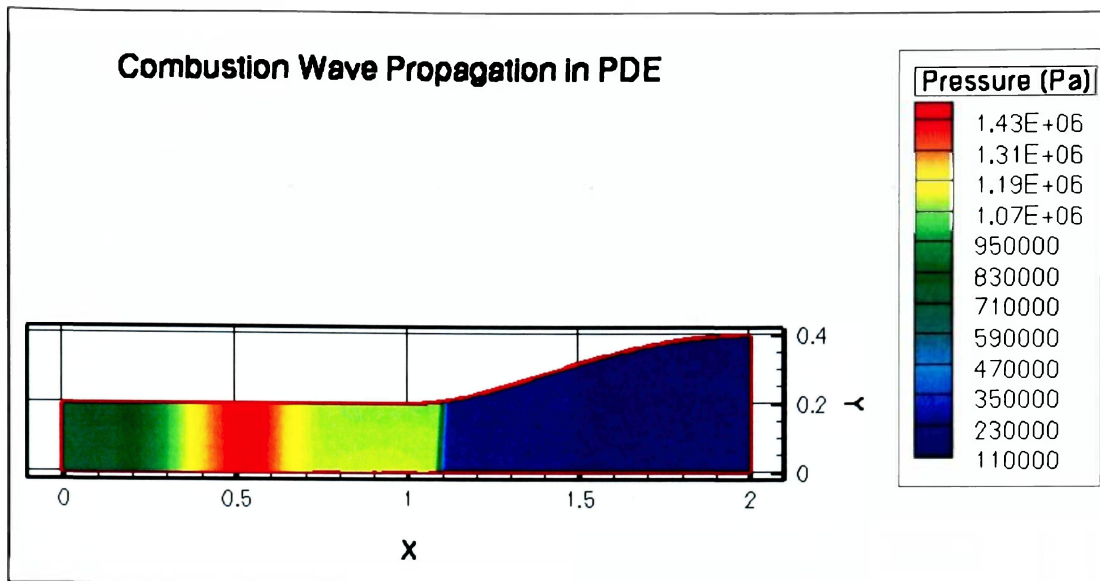
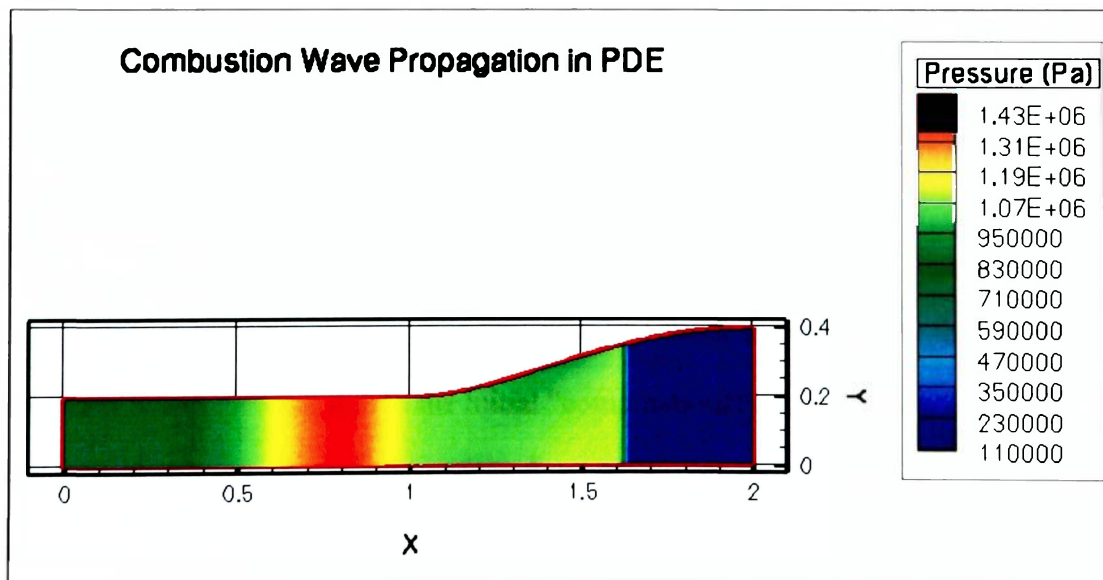


Figure IV.18 Pressure Contours at  $t = 0.12 \text{ msec}$



**Figure IV.19 Pressure Contours at t = 0.24 msec**



**Figure IV.20 Pressure Contours at t = 0.36 msec**

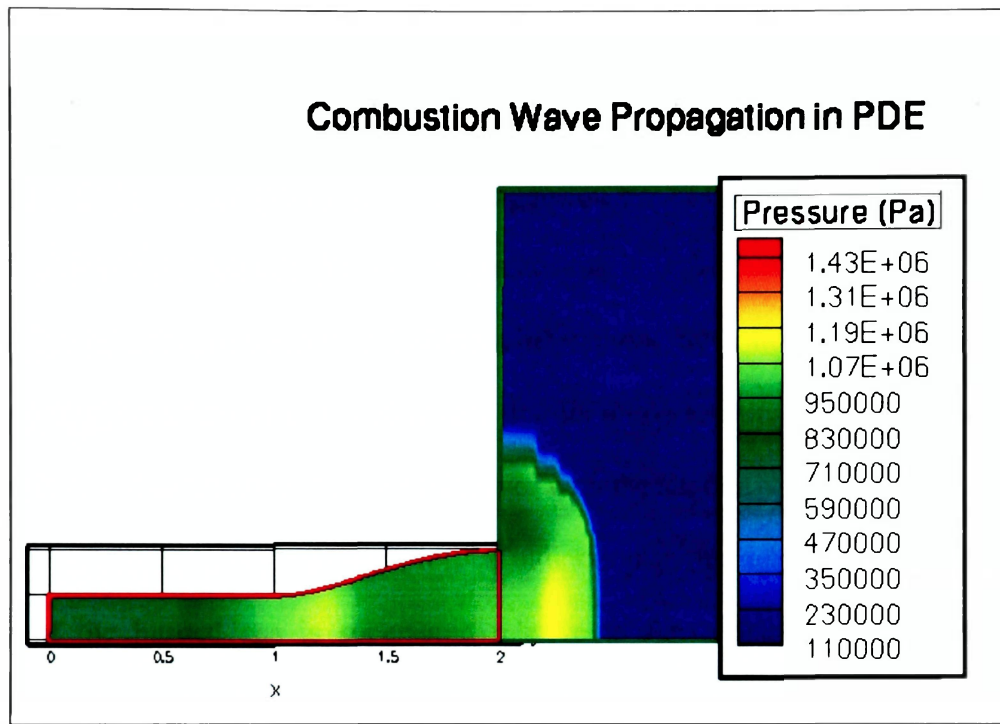


**Figure IV.21 Pressure Contours at t = 0.55 msecs**

#### **IV.2.4 Case I Results Discussion**

One of the first observations that could be made is that of the shock wave and expansion waves forming due to the initial “computational spark” at the closed end of the PDE. The shock wave is traveling through the PDE with a higher pressure ratio than that predicted by the simple shock tube case with the same initial conditions. The pressure ratio slightly increases in the straight tube of the PDE, but it also slightly decreases when the shock wave is moving in the divergent part of the nozzle.

These results agree with the fact that if the surface area of the shock increases with time (what is called a divergent shock) the strength of the shock rapidly attenuates [17]. The velocity of the burned gases immediately behind the shock wave was substantially constant in the straight tube of the PDE and slightly decreased when the shock wave was traveling through the divergent nozzle. The expansion waves that reflected back from the wall trailed the shock wave but it never caught up with it.

Observations of the pressure indicate a detonation, rather than a deflagration. The pressure ratio across the shock is higher than that for a non-reacting shock tube. Also the pressure rise is substantially constant, and moves with the shock.

Observations of the velocity profiles indicate that the detonation is weak. The velocity of the burned gas is supersonic relative to the shock wave. In laboratory coordinates (frame of reference fixed to the wave) however, the velocity of the gases is subsonic as it decreases in the nozzle expansion. The relative Mach number of the burned gas with respect to the shock wave is calculated in Section IV.5 to verify this observation.

### **IV.3 Case II**

In Case II the “computational spark” adjacent to the PDE wall used an initial pressure and temperature of 3 atm, and 2000 K respectively. The pressure ratio between the gas within the computational spark and the unburned gas in front of it was therefore 3, significantly lower than that of Case I. The following set of results shown will be plots of the pressure, temperature and molecular composition along the PDE centerline at 6 instants in time.

#### **IV.3.1 Centerline Pressure, Temperature and Molecular Composition**

At  $t = 1 \mu\text{sec}$ , Figure IV.22 shows an initial spike in pressure and temperature in the “computational spark” zone near the wall. These values of high pressure and temperature correspond to an initial pressure and temperature ratio of 3.52 and 7.97 respectively, across “computational spark” zone. The pressure ratio in Case I was 44.5 and it is significantly higher than that of Case II. This is not the case for the temperature ratio which was only 13.13. Both Cases I and II showed an initial spike in pressure and temperature due to the effect of chemical reactions. Figure IV.23 shows the chemical reactions occurring due to the initial high pressure and temperature, and also shows the concentration of the different species behind the wave.  $\text{H}_2\text{O}$  (water vapor), as in Case I, seems to be produced in larger quantities. Monatomic Oxygen (O) is being produced the least.

In Case II however there is a smaller concentration of H<sub>2</sub>O compared to Case I, most likely due to Le Chatelier's principle; the pressure is higher in Case I. The molar fraction of H<sub>2</sub>O near the wall in Case II is about 0.354 compared to 0.496 of Case I.

At  $t = 0.12$  msec, Figure IV.24 shows the shock wave moving forward with a pressure and temperature ratio of 10.8 and 12.21 respectively. Note that the pressure ratio increased from the initial value of about 3 at  $t = 1 \mu\text{sec.}$ , to 10.8. This increase in pressure is most likely due to the effect of chemical reactions occurring behind the shock wave as shown in Figure IV.25. The simple shock tube results showed that the shock wave should be moving with a lower pressure ratio of 2.18. In Case I, the pressure ratio across the shock wave decreased significantly, from 44.5 ( $t = 1 \mu\text{sec.}$ ) to 10.8 ( $t = 0.12$  msec.). In Case II the pressure ratio increased from 3.5 ( $t = 1 \mu\text{sec.}$ ) to 10.8 ( $t = 0.12$  msec.). It is interesting to note that at this instant in time, both cases have the same pressure ratio across the shock wave. The difference is that in Case II, there is no region of combustion zone of high pressure and temperature trailing the shock wave. In Case II this region with the highest pressure within the PDE occurs right behind the shock wave as shown in Figure IV.24. Figure IV.25 shows that there is an increase in the concentration of H<sub>2</sub>, H<sub>2</sub>O, and OH near the wall, compared to Figure 32.0 However H<sub>2</sub>O is the only one specie whose concentration increases from the wall to right behind the shock wave. In Case I, H<sub>2</sub>O is also the specie with the highest concentration, but its concentration decreases from the wall to where the shock wave is, as shown in Figure 13.0.

At  $t = 0.24$  msec, Figure IV.26 shows that the shock wave has a pressure ratio of 10.97 and a temperature ratio of about 12.18. This pressure ratio is a little higher than the pressure ratio at  $t = 0.12$  msec. Although it is not very significant, the pressure has been

increasing across the shock wave up to now. As in Figure IV.24, at this particular instant in time, the region of high pressure and temperature is still right behind the shock wave. Again, Figure IV.27 shows the chemical composition of the burned gases, with the molar concentration  $\text{H}_2\text{O}$  being the highest behind the shock wave.

At  $t = 0.36$  msec, the pressure and temperature ratio across the shock wave are 10.89 and 12.15 respectively. These are somewhat lower values than those found at  $t = 0.24$  msec. It seems that the shock wave barely loses its strength as it travels through the divergent nozzle. Figure IV.28 shows an expansion wave formed due to the shock wave entering the divergent part of the nozzle. This expansion wave seems to be moving in opposite direction as the shock wave and seems to be decreasing the pressure of the gas behind it. The same behavior is observed in Case I when the shock wave enters the divergent nozzle of the PDE.

At  $t = 0.55$  msec., the shock wave has already exited the PDE tube. Expansion waves are formed at the end of the nozzle and propagate inside, as shown in Figure IV.30. As in Case I, the overall pressure inside the PDE is reduced. The temperature is almost constant inside the PDE tube. The highest temperature value is at the wall or the closed end of the PDE tube. This highest temperature is 3631.7 K. The lowest pressure is 7.3 atm. Figure IV.31 shows no significant change in the chemical composition of the products as compared with the previous instants of time. The following final figures will show the results a while after the shock has exited the PDE tube and expansion waves have significantly reduced the pressure inside the PDE tube.



Figure IV.32 shows that the pressure inside has decreased due to the reflected expansion waves created by the shock wave exiting the PDE and the expansion waves coming back from the nozzle throat area. The minimum pressure found inside the PDE is 4.95 atm. compared to 7.3 at 0.55 msec. This value is higher than that of case one at the same instant of time. In Case I, the minimum pressure was 4.79.

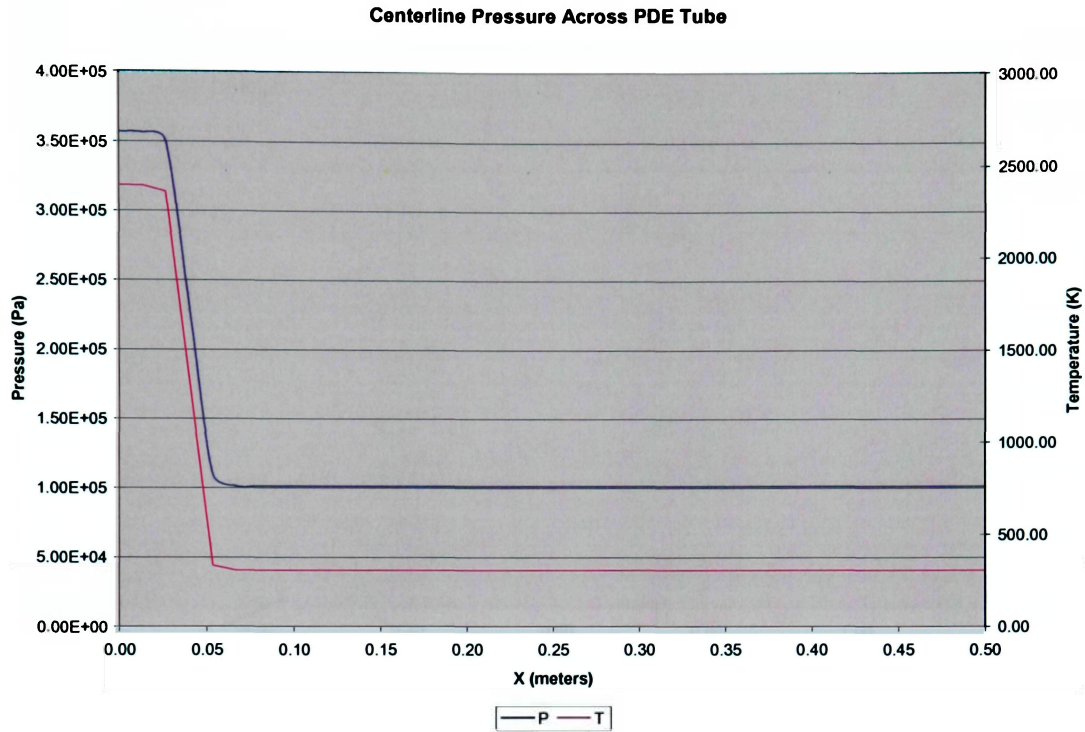


Figure IV.22 Centerline Pressure and Temperature at  $t = 1 \mu\text{sec}$

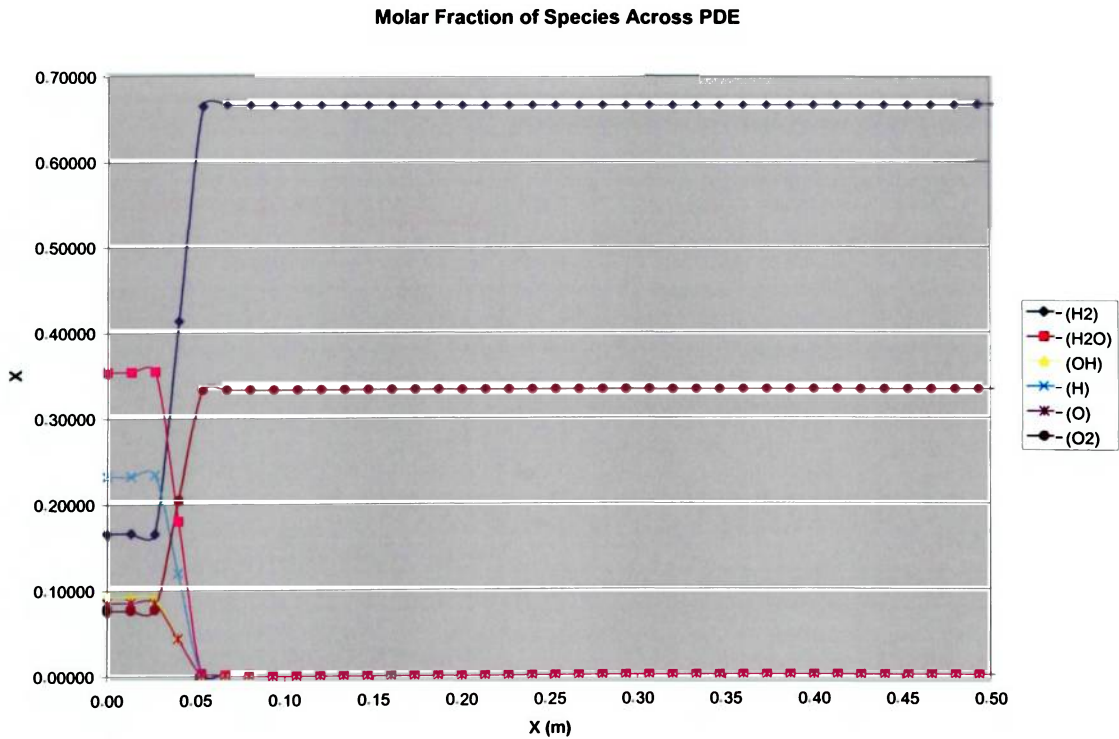
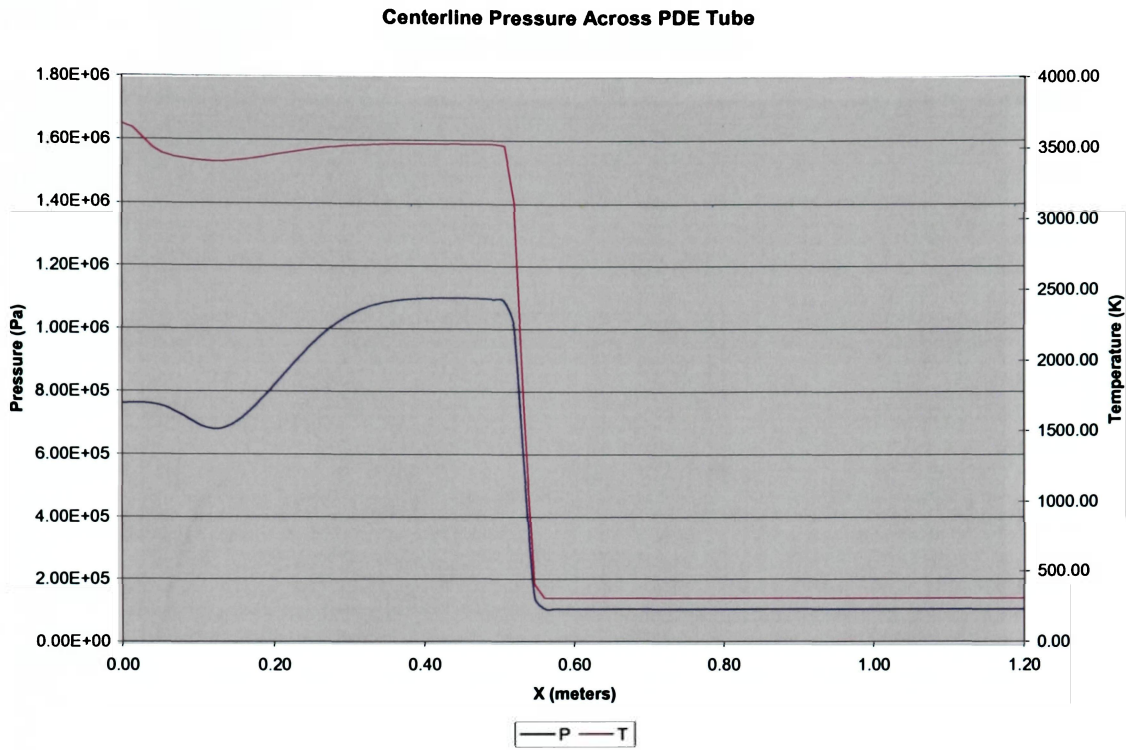
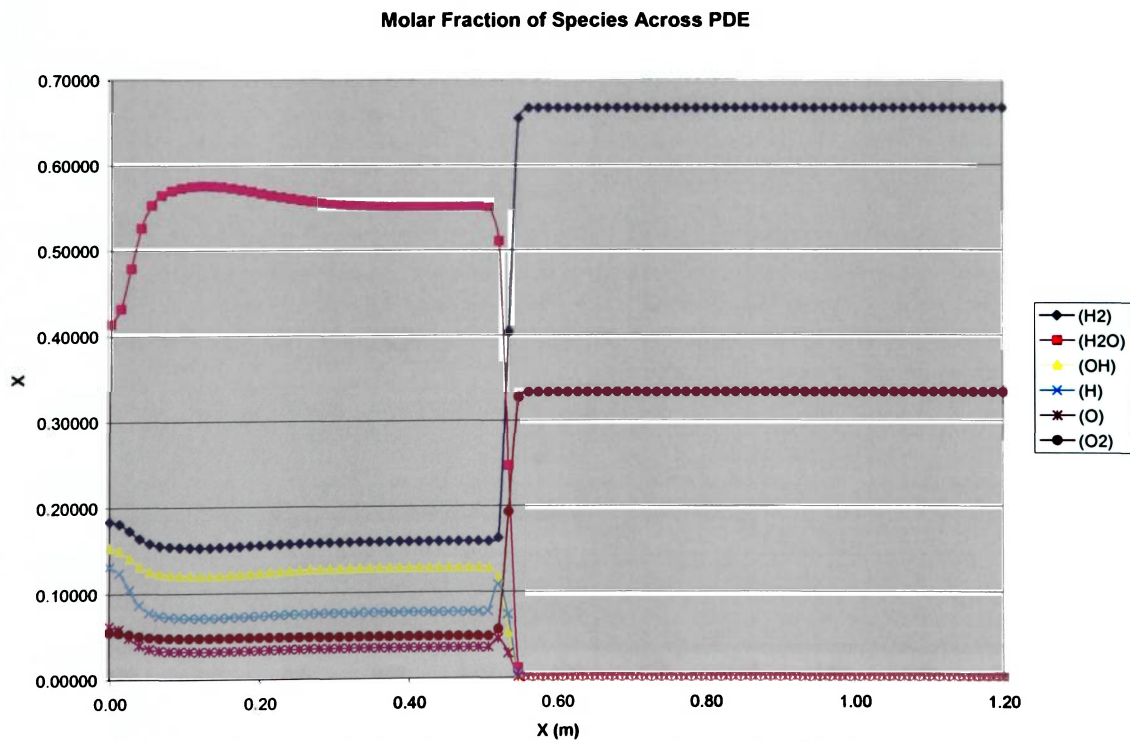


Figure IV.23 Molecular Composition at  $t = 1 \mu\text{sec}$



**Figure IV.24 Centerline Pressure and Temperature at t = 0.12 msecs**



**Figure IV.25 Molecular Composition at t = 0.12 msecs**

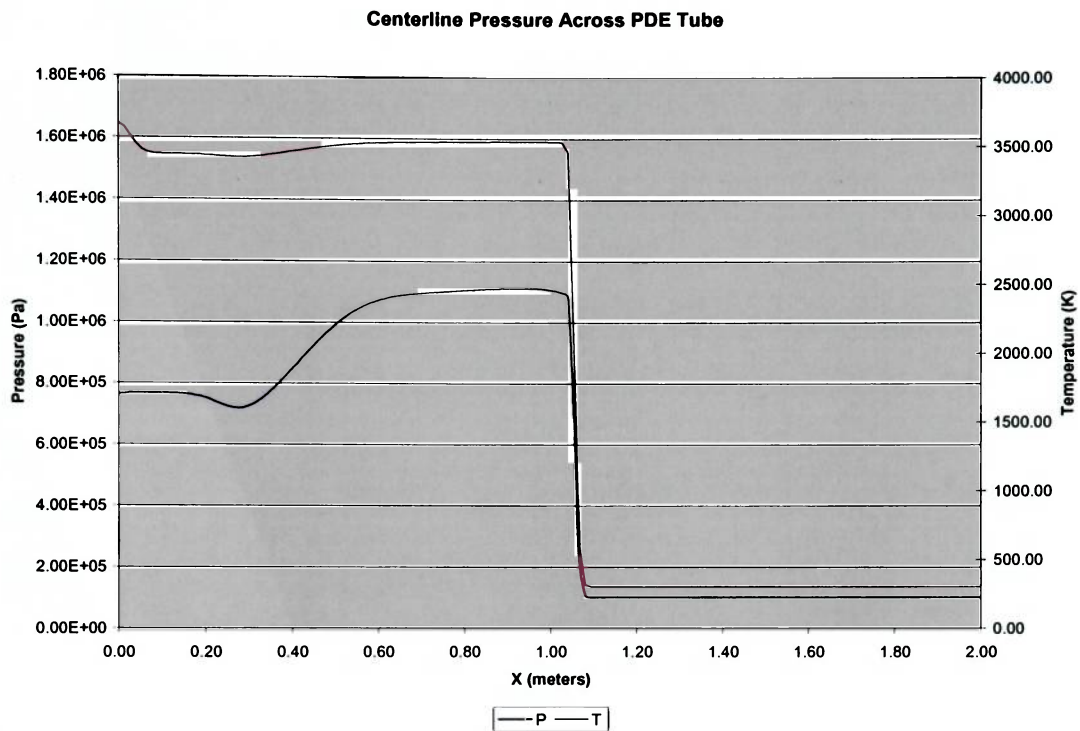


**Figure IV.26 Centerline Pressure and Temperature at t = 0.24 msec.**

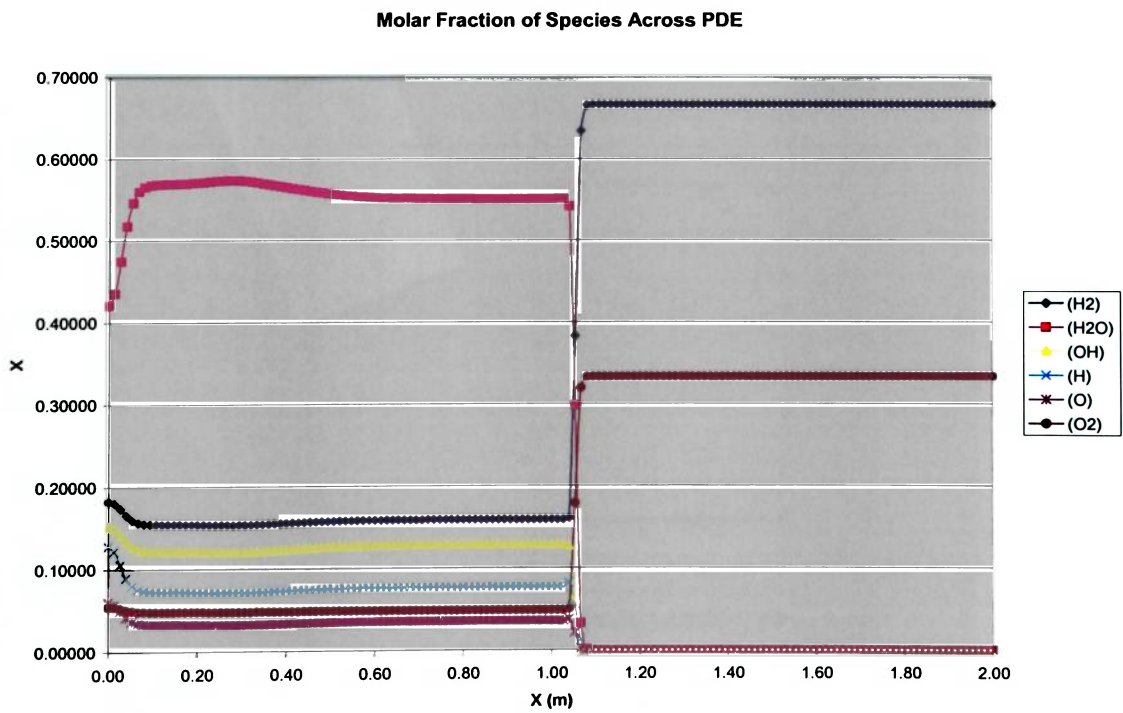


**Figure IV.27 Molecular Composition at t = 0.24 msec**

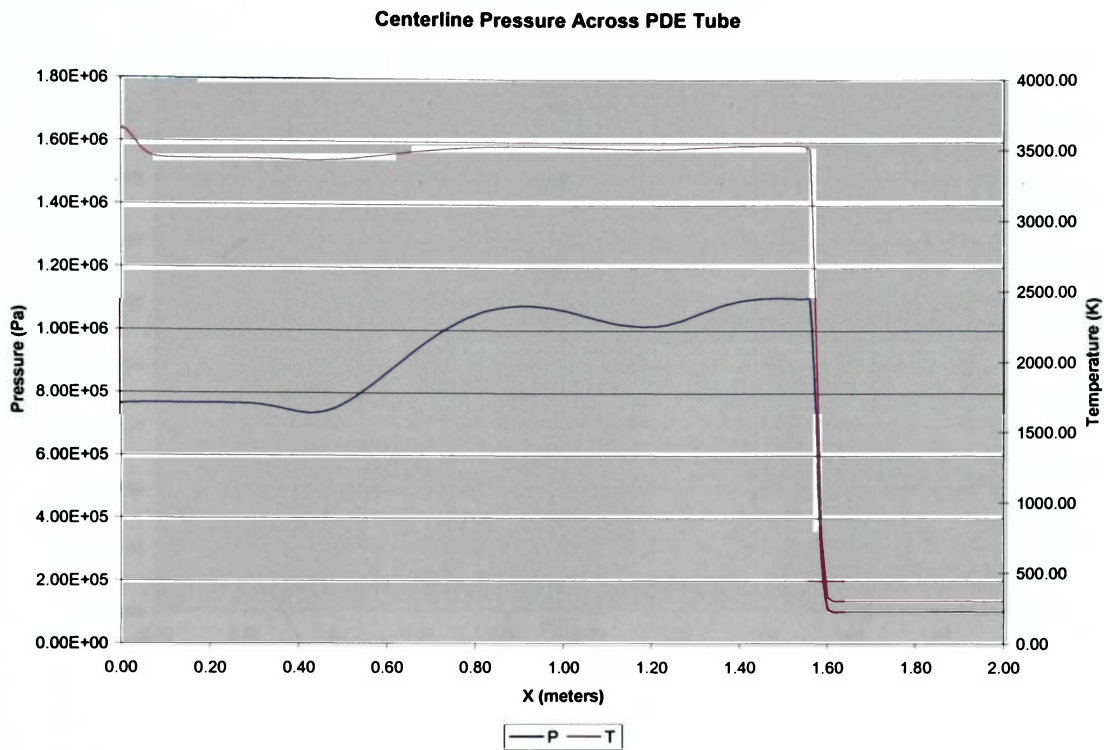


**Figure IV.28 Centerline Pressure and Temperature at t = 0.36 msec.**

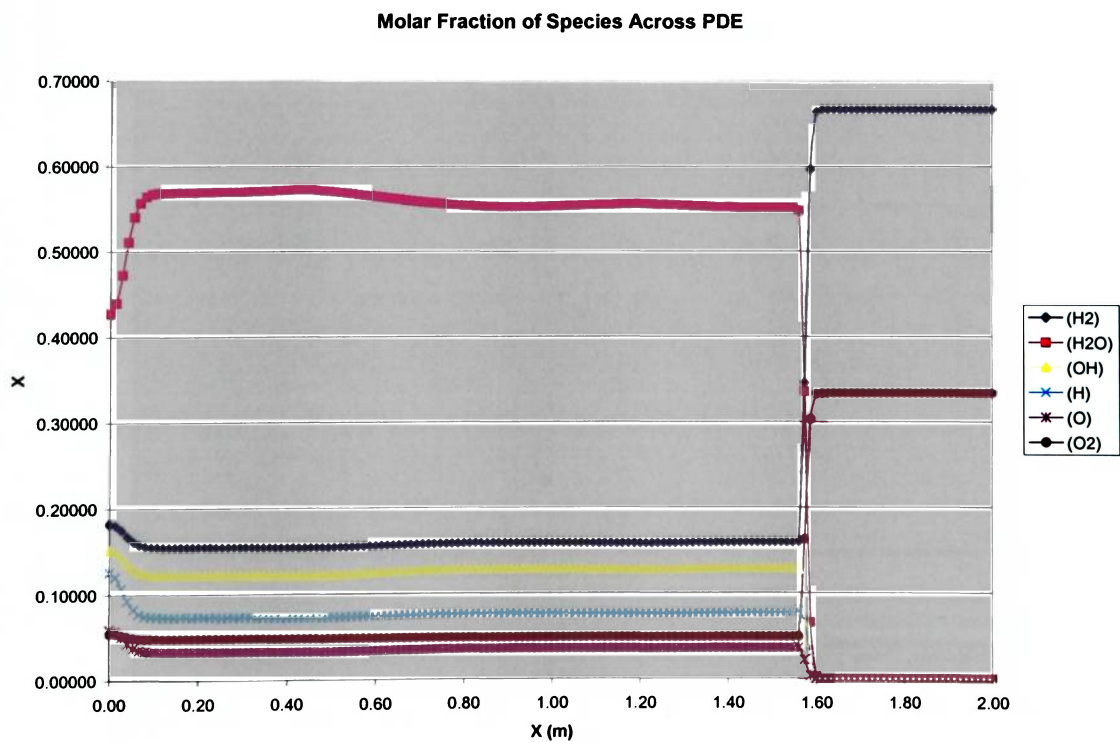


**Figure IV.29 Molecular Composition at t = 0.36 msec**

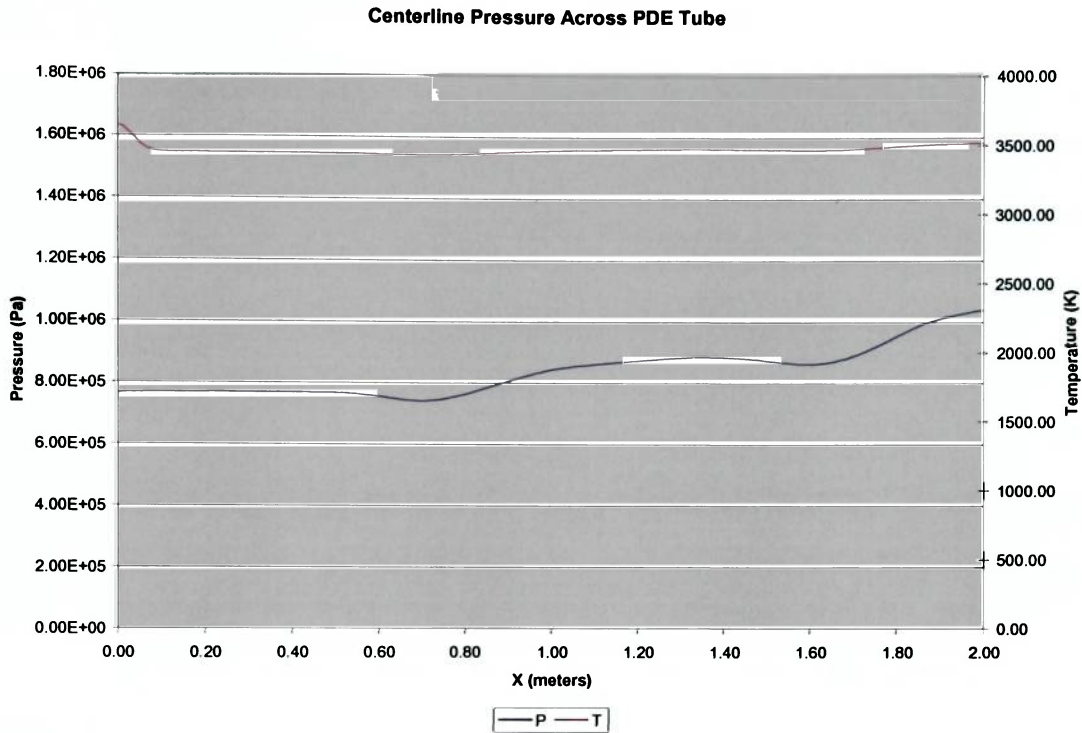


Figure IV.30 Centerline Pressure and Temperature at t = 0.55 msecs.

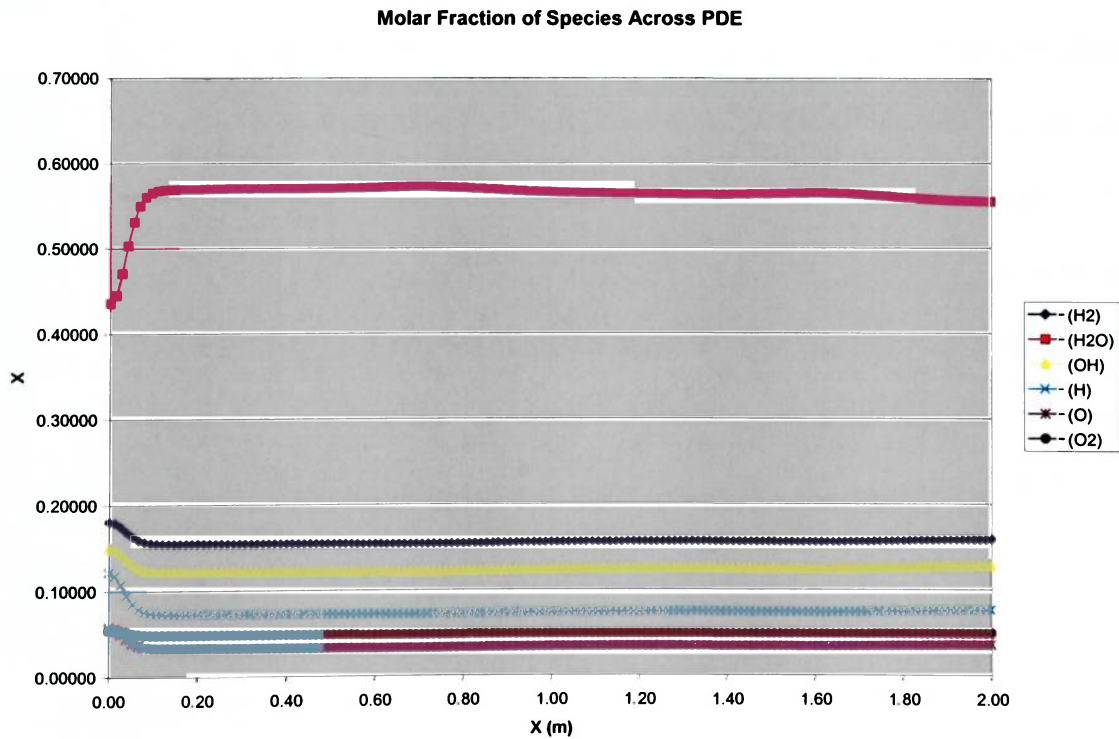
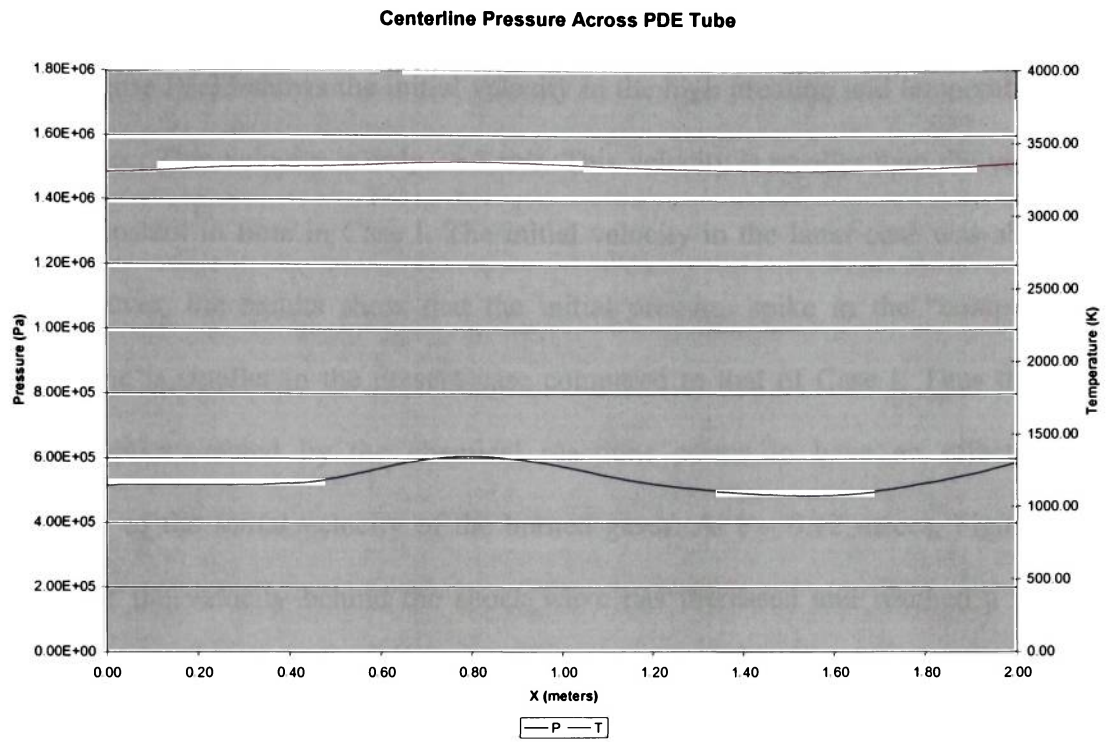


Figure IV.31 Molecular Composition at t = 0.55 msecs.

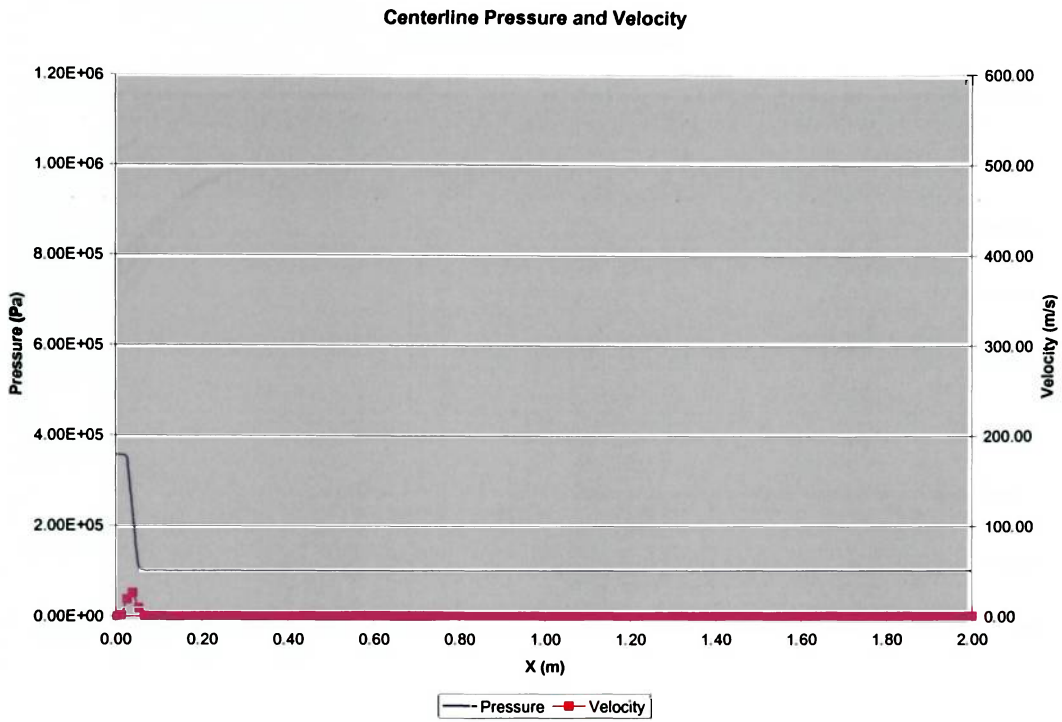


**Figure IV.32 Centerline Pressure and Temperature at t = 1.5 msec.**

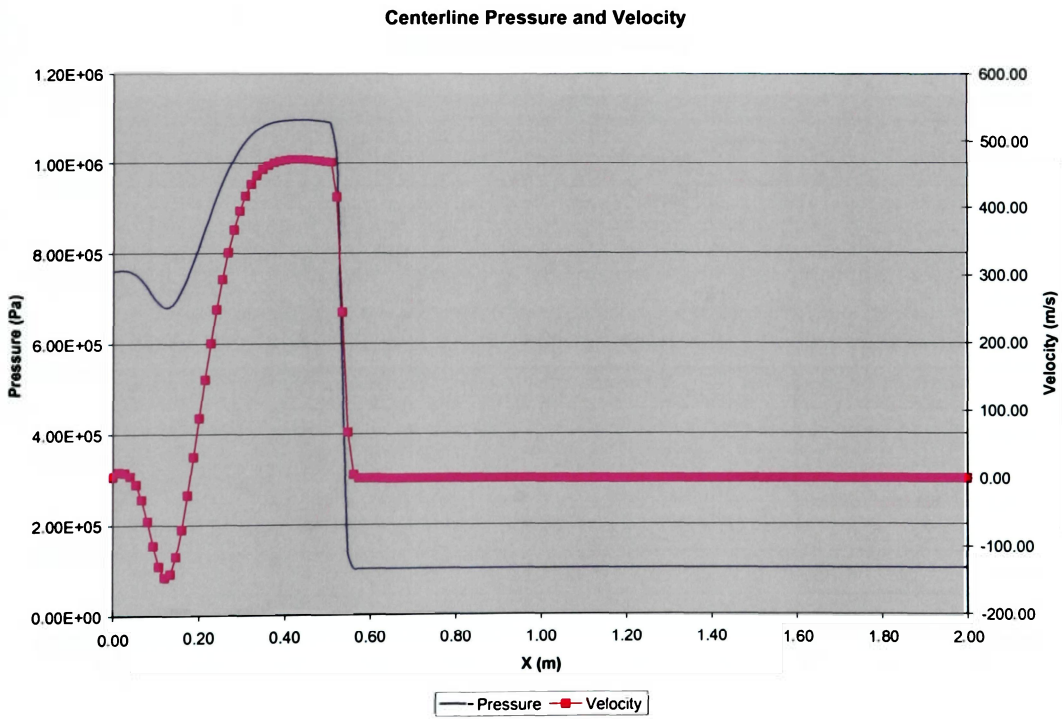
### IV.3.2 Centerline Pressure and Velocities

Figure IV.33 shows the initial velocity in the high pressure and temperature zone at  $t = 1 \mu\text{sec}$ . This velocity is only 25.8 m/s. This velocity is smaller than the velocity at the same instant in time in Case I. The initial velocity in the latter case was about 155 m/s. However, the results show that the initial pressure spike in the “computational spark” zone is smaller in the present case compared to that of Case I. Thus the initial pressure spike created by the chemical reactions seems to have an effect on the magnitude of the initial velocity of the burned gases. At  $t = 0.12 \text{ msec}$ , Figure IV.34 shows that the velocity behind the shock wave has increased and reached a value of 472.71 m/s. This figure also shows that the velocity of the burned gases around  $x = 0.2 \text{ m}$ , is negative. Physically this means that there is a right running expansion wave. This expansion wave was originally created by the pressure ratio between the “computational spark” zone and the stagnant gases. This is verified by the fact that the pressure ratio near the wall has not decreased since  $t = 1 \mu\text{sec}$ . Figure IV.35 shows that the burned gas velocity behind the wave has increased slightly, reaching a value of 478.87. Note that the velocity of the burned gases immediately behind the shock wave is almost the same for Cases I and II at  $t = 0.12$  and  $0.24 \text{ msec}$ . The pressure ratio across the shock wave is almost the same for both cases also. The results show that, although the initial velocities are different in Case I and II, the shock wave and the burned gas immediately behind it accelerate very fast until reaching a similar velocity for both cases at about 0.12 msec. Figures IV.36 and IV.37 show that the velocity of the burned gases behind the shock wave decreases slightly as the shock wave passes through the nozzle.





**Figure IV.33 Centerline Pressure and Velocity at  $t = 1 \mu\text{sec}$**



**Figure IV.34 Centerline Pressure and Velocity at  $t = 0.12 \text{ msec}$**

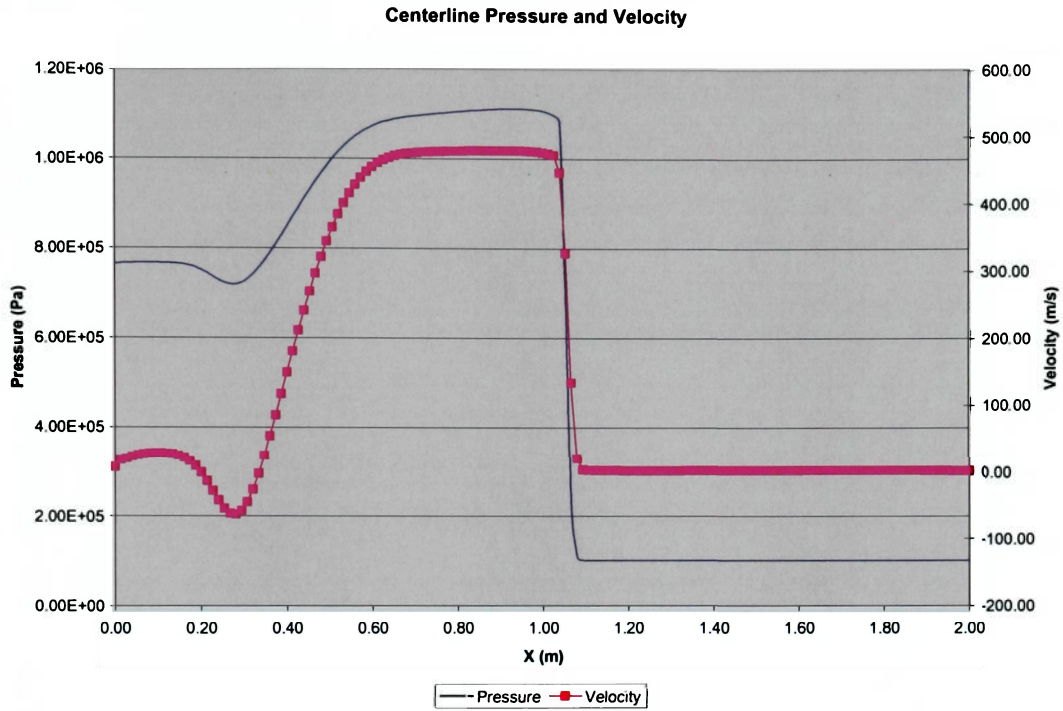


**Figure IV.35 Centerline Pressure and Velocity at t = 0.24 msec**

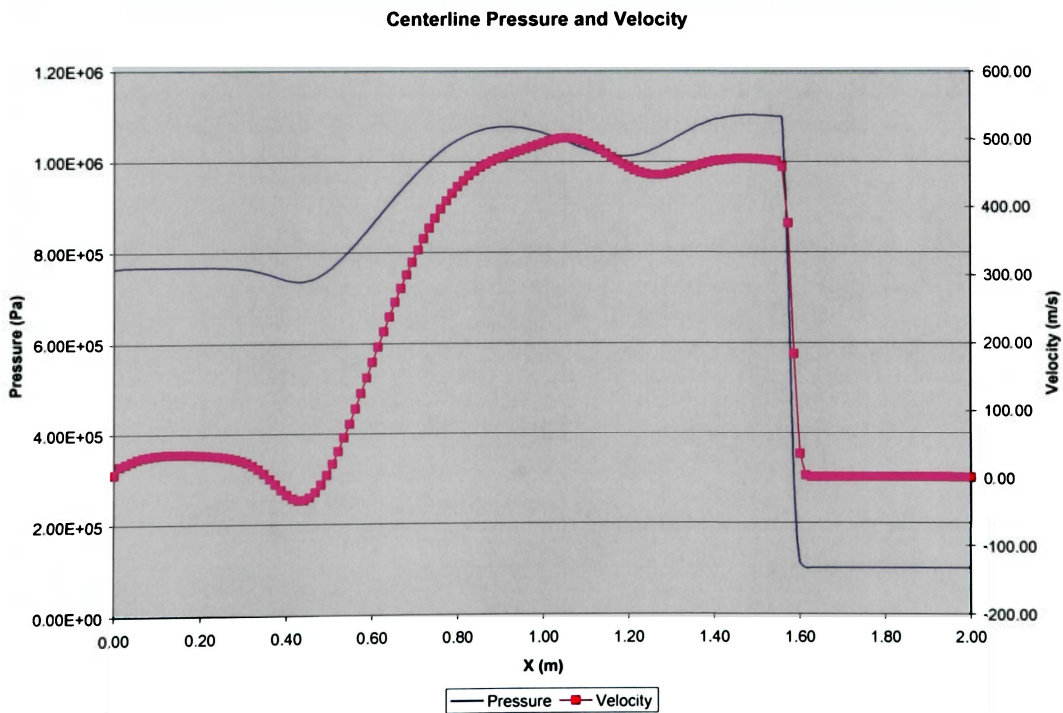


**Figure IV.36 Centerline Pressure and Velocity at t = 0.36 msec**

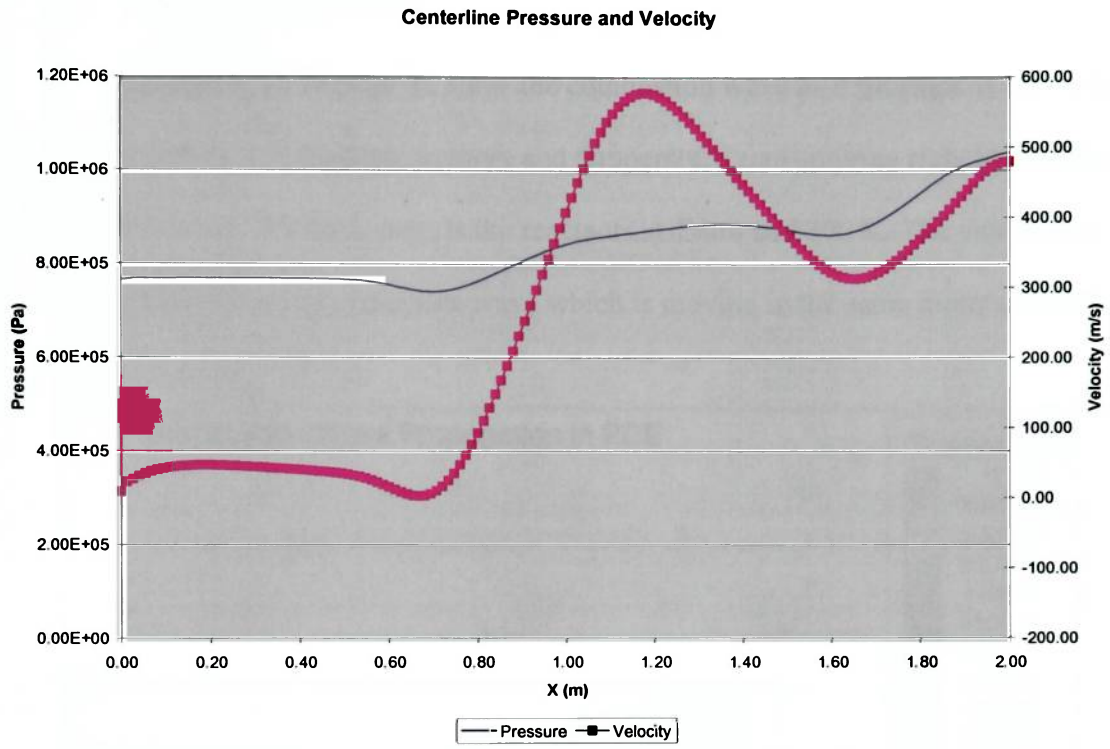


**Figure IV.37 Centerline Pressure and Velocity at t = 0.55 msec**

### IV.3.3 Pressure Contours

Figures IV.38 through 42 show the combustion wave as it propagates out of the PDE. The red zone is the high pressure and temperature zone moving right behind the combustion wave. The blue zone is the reactants at 1 atm and 300 K. The yellow line indicates the head of the expansion wave which is moving in the same direction as the combustion wave.

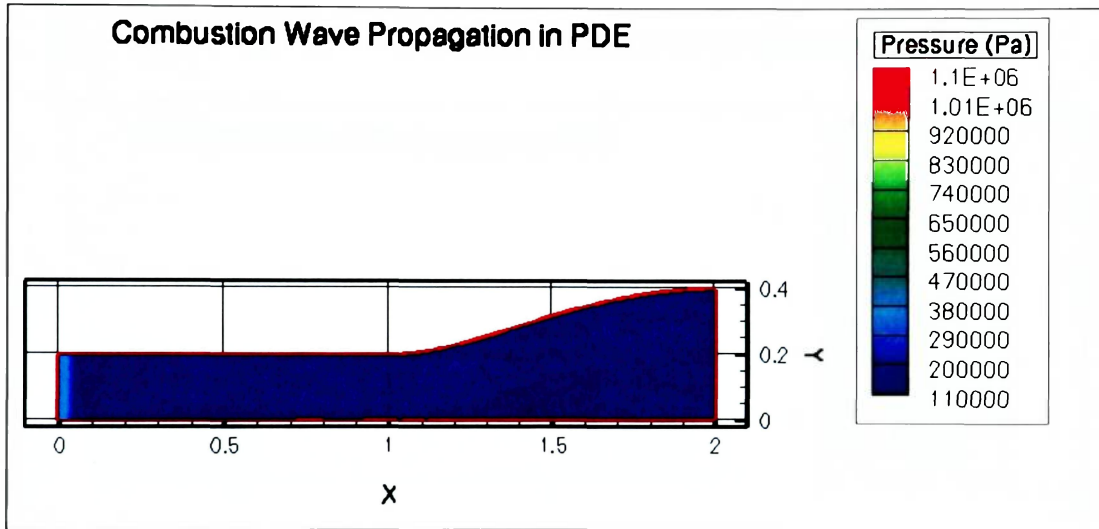


Figure IV.38 Pressure Contours at  $t = 1 \mu\text{sec}$

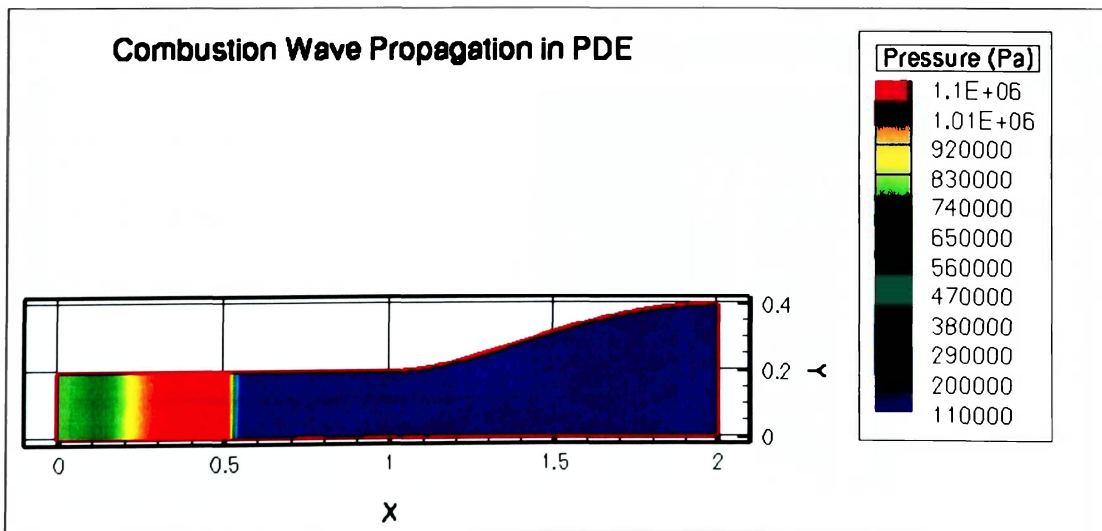
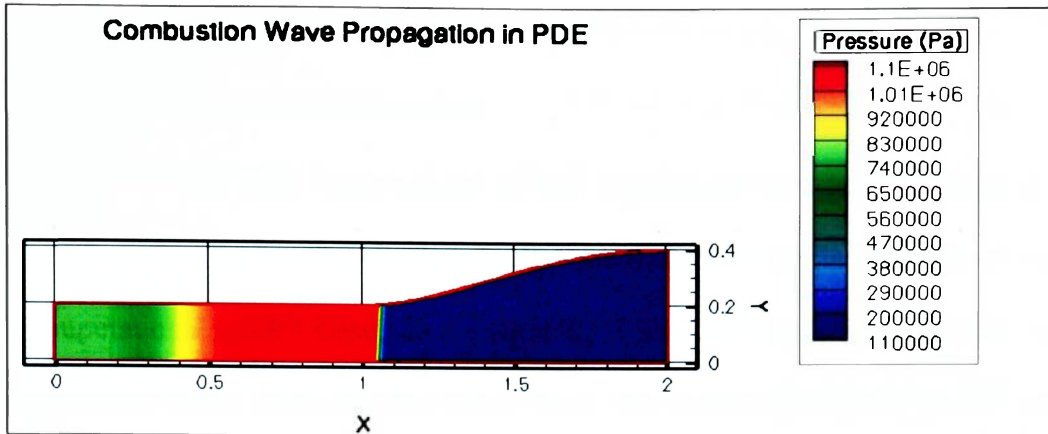
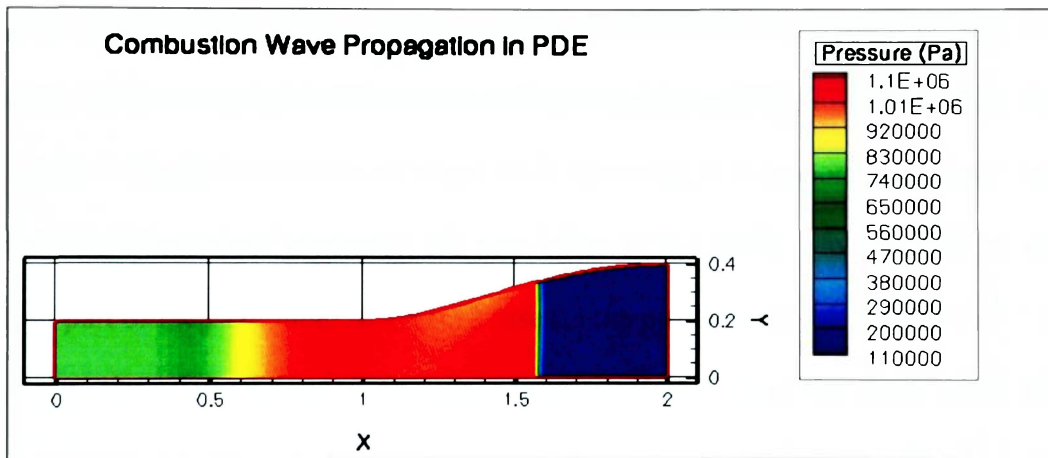


Figure IV.39 Pressure Contours at  $t = 0.12 \text{ msec}$



**Figure IV.40 Pressure Contours at t = 0.24 msecs**



**Figure IV.41 Pressure Contours at t = 0.36 msecs.**

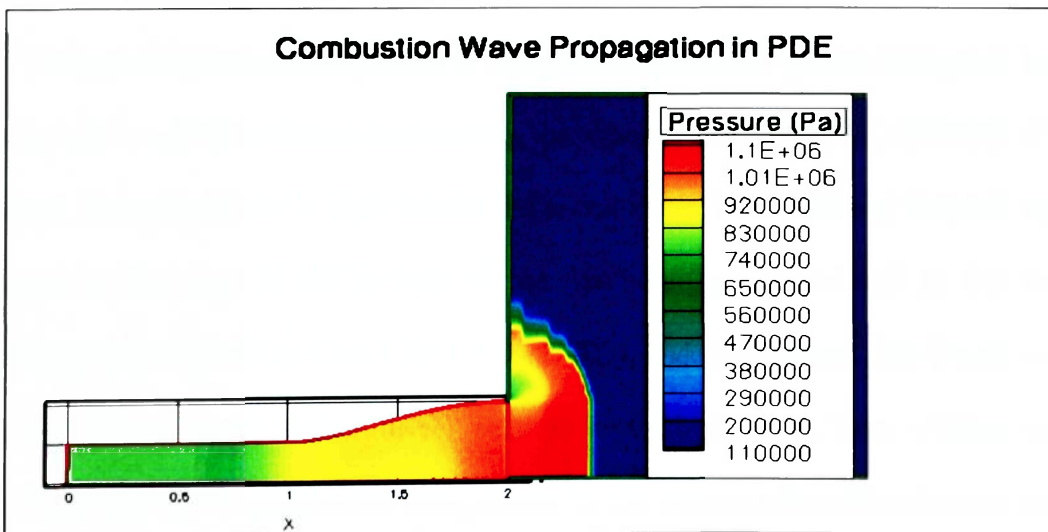


**Figure IV.42 Pressure Contours at t = 0.55 msecs**

#### **IV.3.4 Case II Results Discussion**

One of the first observations is the significant increase in pressure and temperature across the moving shock wave in Case II, from the initial conditions given in the “computational spark”. Case I in the other hand, showed that the pressure ratio of the moving shock wave decreased in value from the initial conditions given for the “computational spark”. In both Case I and II, however, the shock wave seemed to obtain the same pressure ratio of 11 as it propagated out of the PDE. From the results shown for this case, the pressure ratio of the shock wave moving through the PDE seemed to change little once it reached the value of about 11.0. However, it is important to note that the pressure ratio increased somewhat for both cases as the shock wave moved across the straight part of the PDE tube. At  $t = 0.12$  msec., the pressure ratio across the shock wave was 10.8. At  $t = 0.24$  msec., the pressure ratio was 10.97. Once the shock wave entered the divergent part of the nozzle, the pressure ratio started decreasing by a small amount as it exited the PDE. At  $t = 0.36$  msec., the pressure ratio was about 10.87.

The second observation is that in comparison with Case I, Case II does not have a high pressure and temperature zone trailing the shock wave. In Case II, the zone of high pressure and temperature is right behind the shock wave. Note however that the highest pressure in this zone is not as high as the maximum pressure found in the trailing combustion zone found in Case I for  $t = 0.12, 0.24,$  and  $0.36$  msec. This pressure peak resulted from a much higher driver section in Case I, rather than combustion. A detonation requires a shock wave being driven by the energy released by the combustion behind it.

In this Case, the results show that there are reactions occurring behind the shock wave; and that as a consequence of these reactions and the heat or energy released by them, the shock wave has increased its strength (increase in pressure ratio across the shock wave).

The next observation made is the difference in the molar concentration along the PDE tube of the specie  $H_2O$  between Case II and Case I. In Case II, at all instants in time, the concentration of  $H_2O$  is the smallest near the wall or closed end of the PDE, and it increases towards the shock wave. In Case I, there is a higher concentration of  $H_2O$  near the wall, and then its concentration decreases towards the shock wave. In both cases however, after  $t = 0.12$  msec, the concentration of all the species seems to be the same right behind the shock wave.

Another observation made when comparing the results for Case I and II is the decrease in magnitude of the pressure at the wall of the PDE for Case I after  $t = 1 \mu\text{sec}$ . As described earlier this pressure decreased from 45 to 8 atm, whereas in Case II, the wall pressure increased from 3 to 8 atm. Given the shape of the centerline pressure histories for both cases near the wall, it is very possible that this increase and decrease in wall pressure for Case II and I is caused by two factors. One factor is how wide and close to the wall the “computational spark” zone is. The second factor is the magnitude of the pressure ratio across this “computational spark” zone. The higher the pressure ratio across this computational spark zone and the stagnant gases, – analogous to the pressure ratio across the driver and the driven section of a simple shock tube – the higher the strength of the expansion waves reflecting in opposite direction to the shock wave. In Case I the expansion waves quickly propagated to the end of the wall, and since the computational spark was only three cells in width, the expansion waves reached the wall

and reflected back. Thus, the pressure at the wall of the PDE continuously decreased until the tail of the expansion waves hit and reflected back. This seems not to be what is happening in Case II. As in Case I, the pressure ratio across the “computational spark” and the stagnant gases will form expansion waves and a shock wave moving in opposite direction. However, the pressure ratio in Case II is much smaller than in Case I and thus the expansion waves will not travel as fast. In Case II, the velocity induced behind the moving shock wave is much bigger than the velocity at which the head of the expansion wave is moving towards the wall. Thus, the head of the expansion wave will not reach the wall and will not cause the pressure in the wall to decrease.

Finally, the pressure and temperature ratios across the propagating shock wave for both Cases I and II seem to indicate that in both cases, a detonation has formed. Per the definition of detonation, the shock wave is being driven and its pressure ratio kept almost constant by the energy released by the chemical reactions occurring behind it. Both Case I and II, show that in fact, the molecular concentration is the same immediately behind the shock wave. Although, two different sets of initial conditions were used as the “computational spark”, both conditions seemed to have created the right set of conditions for a combustion wave to form and immediately catch up with the shock front. Since the strength of the detonation wave is the same for both cases, the velocity and the Mach number of the detonation wave relative to the stagnant gases will be calculated using the results for Case II.

The next case studied in this thesis will be that of a simple shock tube, with no chemical reactions occurring. These results will be used to validate the effect of chemical



reactions in the shock wave strength and velocity, and to validate the computational results with those of Case B of the analytical shock tube calculations.

## IV.4 Case III

The following case is similar to that of a shock tube discussed earlier. In this case a narrow region of high pressure and temperature will be used as the driver section, three cells in width in the x – direction as in the previous two cases. The initial conditions for this high pressure and temperature region are the same as in Case II (3 atm and 2000 K). In this case there are no chemical reactions. The following results shown will be plots of pressure and temperature along the PDE centerline at the same 6 instants of time as in the previous two cases.

### IV.4.1 Centerline Pressure and Temperature

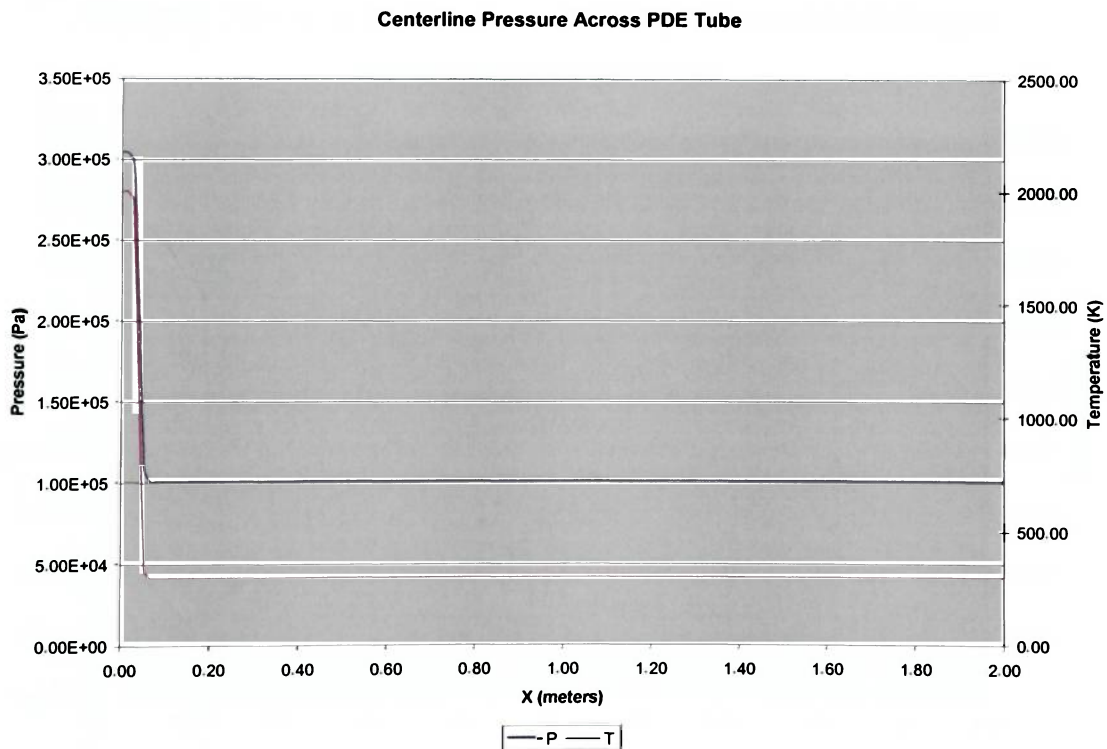


**Figure IV.43 Centerline Pressure and Temperature at  $t = 1 \mu\text{sec}$**

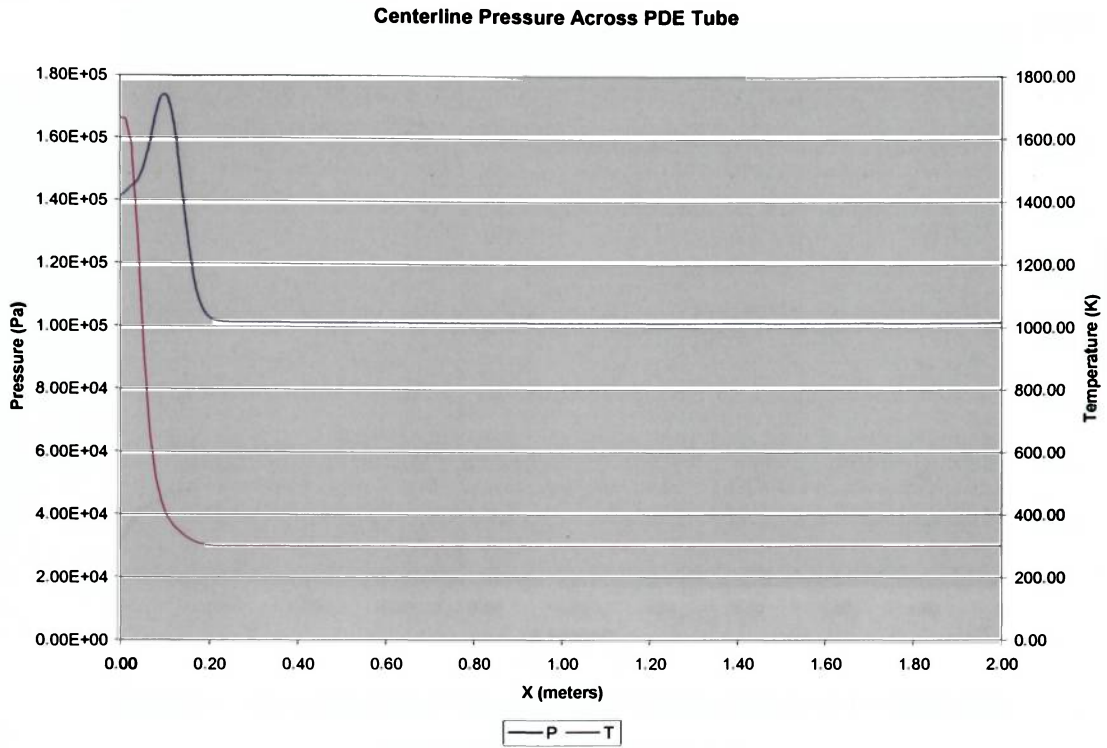


**Figure IV.44 Centerline Pressure and Temperature at t = 0.12 msec**

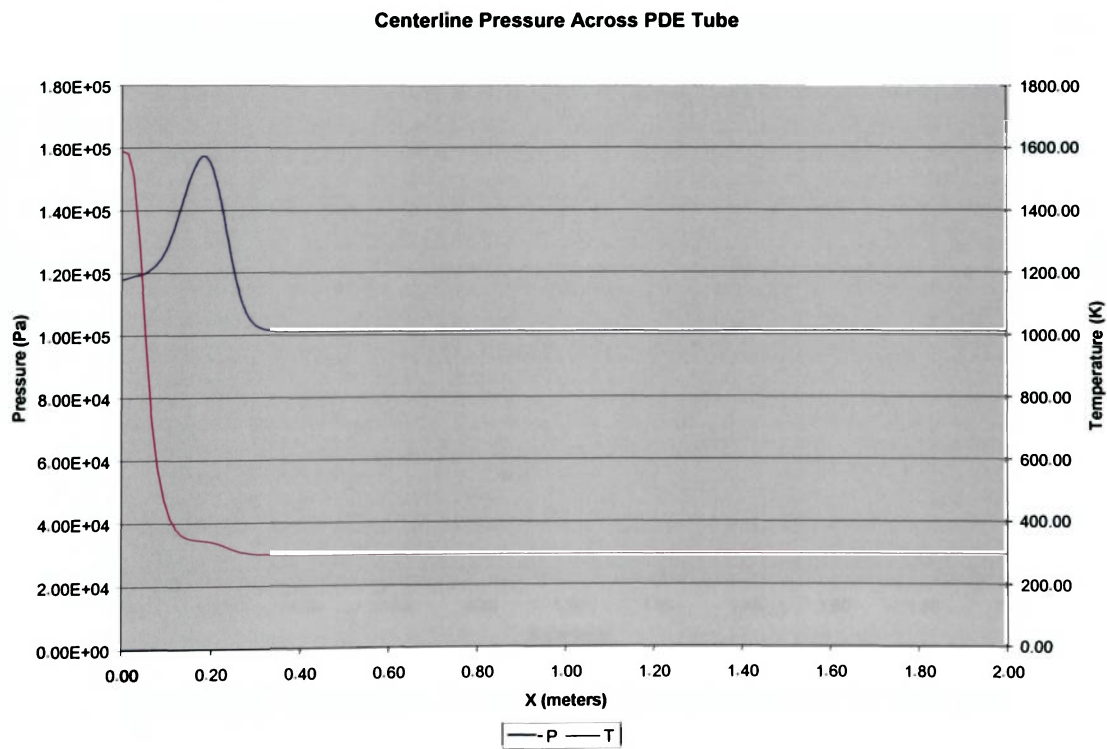


**Figure IV.45 Centerline Pressure and Temperature at t = 0.24 msec**

Centerline Pressure Across PDE Tube

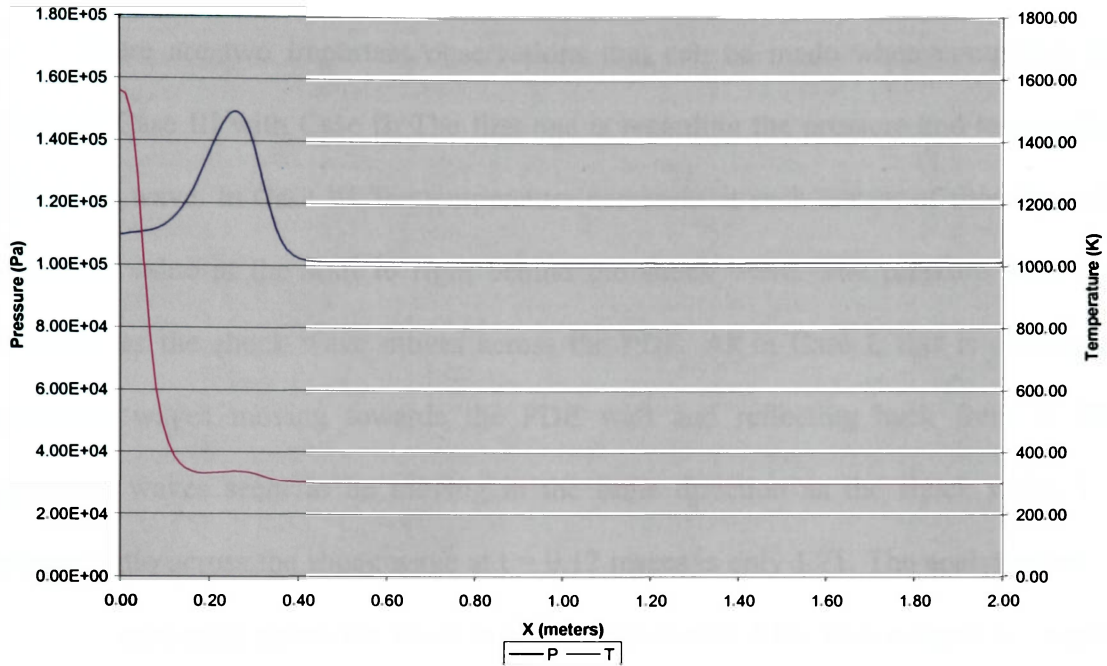


Figure IV.46 Centerline Pressure and Temperature at t = 0.36 msec

Centerline Pressure Across PDE Tube

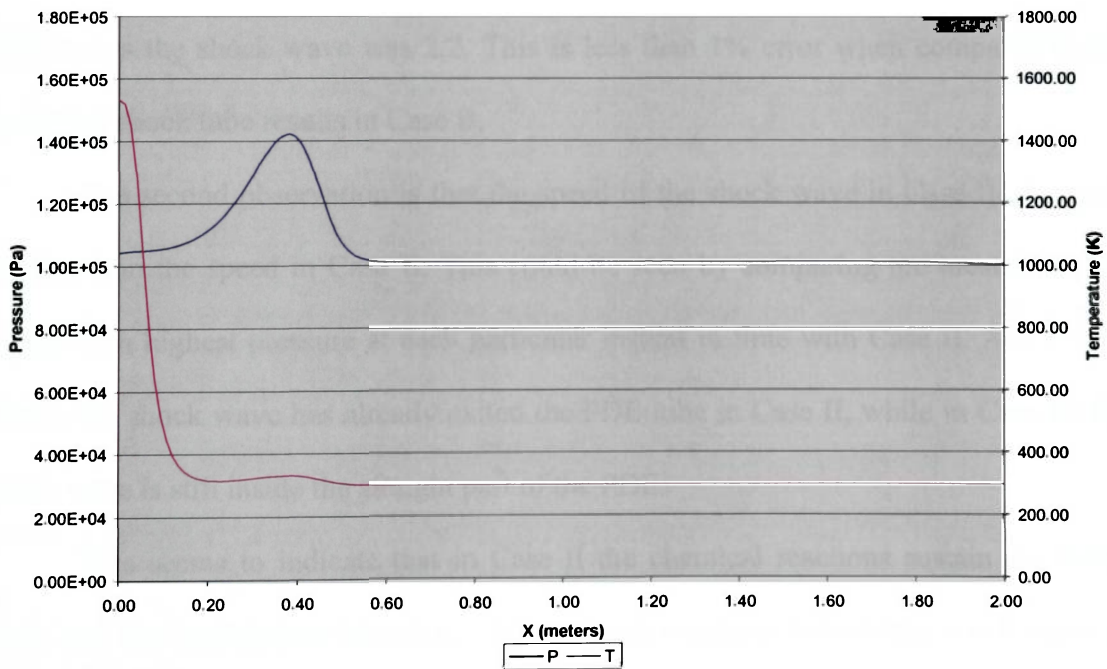


Figure IV.47 Centerline Pressure and Temperature at t = 0.55 msec

#### IV.4.2 Case III Results Discussion

There are two important observations that can be made when comparing the results of Case III with Case II. The first one is regarding the pressure and temperature behind the wave. In Case III, the temperature decreases at each instant of time from the maximum value at the wall to right behind the shock wave. The pressure ratio also decreases as the shock wave moves across the PDE. As in Case I, this is due to the expansion waves moving towards the PDE wall and reflecting back from it. The expansion waves seem to be moving in the same direction as the shock wave. The pressure ratio across the shock wave at  $t = 0.12$  msec is only 1.71. The analytical value of the pressure ratio across the shock wave in Case B was 2.18. This is equal to an error of 22%. However, when the driver section in Case III was made 38 cells wider in the x-direction to avoid an earlier reflection of the expansion waves from the wall, the pressure ratio across the shock wave was 2.2. This is less than 1% error when compared to the analytical shock tube results in Case B.

The second observation is that the speed of the shock wave in Case III, is much smaller than the speed in Case II. This could be seen by comparing the location of the region with highest pressure at each particular instant in time with Case II. At  $t = 0.55$  msec, the shock wave has already exited the PDE tube in Case II, while in Case III the shock wave is still inside the straight part of the PDE.

This seems to indicate that in Case II the chemical reactions sustain the shock wave and the combustion behind it. The chemical reactions behind the shock wave in Case II do not allow for a decrease in the pressure ratio, but rather sustains an almost constant pressure ratio throughout the length of the PDE.

## IV.5 Detonation Wave Speed

Before it could be asserted that a detonation wave has been obtained for Cases I and II of this study, it is necessary to calculate the speed of the shock wave relative to the quiescent gases in front of it. A subroutine is implemented in the CFD code to be able to track the position of the region with the highest pressure difference along a constant j cell index value. This highest pressure difference corresponds to the location of the shock wave within the PDE. The change in position is then divided by the time period taken to move from one x location to the other ( $x_2 - x_1$  has to be greater than 0.1 for the subroutine to calculate the speed).

$$|v| = \frac{\Delta x}{\Delta t} = \frac{x_2 - x_1}{t_2 - t_1} \quad \text{Equation IV.1}$$

In equation IV.1,  $|v|$  is the speed of the wave in the x - direction. To calculate the Mach number of the shock wave or possible detonation wave relative to the stagnant gases, the following relation is used.

$$M_{dw} = \frac{|v|}{\sqrt{\gamma_{mix} R_{mix} T}} \quad \text{Equation IV.2}$$

The following are the results obtained at different locations of the shock or detonation wave as it travels out of the PDE.

**Table IV.2 Detonation Wave Velocity and Mach Number**

Shock/Detonation location (m)	Shock/Detonation Speed (m/s)	Mach Number
0.147	3344.96	6.20
0.362	4389.60	8.14

0.657	4888.21	9.06
1.139	4376.89	8.11
1.455	4336.98	8.04

Table IV.2 shows indeed that the wave is moving at supersonic speed and that the detonation wave is accelerating up to the where the nozzle throat area starts. The divergent nozzle decelerates the shock or detonation wave when it goes through it. To be able to compare these results with other experimental results, an average speed is taken.

$$|v_{ave}| = 4267.33 \frac{m}{s}$$

The relative Mach number of the detonation wave was calculated with the stagnant gases stoichiometrically mixed and at a pressure and temperature of 1 atm. and 300 K. The results obtained for the pressure ratios and detonation velocities are compared in Table IV.3 to those obtained by He and Karagozian [14] [15], and those published by Kuo [7].

Having established that a detonation wave has been obtained, it is necessary to recall the discussion of the Hugoniot Curve in section II.1 in order to establish what kind of detonation it is. As discussed earlier, there are two regions in the upper branch of the Hugoniot Curve. The regions are separated by the upper Chapman-Jouguet point. In order to establish whether a weak, strong or CJ wave was obtained, the mach number of the burned gases relative to the wave is calculated. Since the velocity of the burned gases behind the wave is similar for Cases I and II and almost constant after 0.12 msec, the mach number of the burned gases relative to the wave will be calculated at  $t = 0.12$  msec.

The velocity of the shock wave and the gas behind it relative to the laboratory frame are respectively,

$$v_{wave} = 4390 \frac{m}{s}$$

$$v_{gas} = 472.71 \frac{m}{s}$$

Thus, the velocity of the burned gas relative to the wave is

$$v_{gas\_rel} = v_{wave} - v_{gas} = 3917.29 \frac{m}{s}$$

The Mach number is then,

$$M_{gas} = \frac{3917.29 \frac{m}{s}}{\sqrt{1.217(568)3531.86}} = 2.5$$

The Mach number of the burned gas relative to the shock front is therefore supersonic.

This indicates that the combustion wave obtained in this study is a weak detonation.



## IV.6 Results Comparison

**Table IV.3 Comparison of Case II Results with other Computational and Experimental Results**

	Case II (2D)	Karagozian (2D)	Kuo (Analytical 1D)
$P_2/P_1$	$\approx 11.0$	$\approx 10.0$	18.0
<b>Detonation Velocity (m/s)</b>	4267.33	N/A	2806

The average detonation velocity found in this study seems to be higher than the velocity obtained by one of the analytical methods described in [7]. The reason for the difference in detonation wave velocities is most likely because the velocity in this study is that of a weak detonation. The velocity obtained by Kuo is that of a CJ detonation wave. Table IV.3 also shows that the pressure ratio obtained in this study for a weak detonation is smaller than that for a CJ detonation wave. There is also some error due to numerical dissipation across the shock wave, since the CFD code is only first order accurate in this study.

Table 6.0 also shows the pressure ratio across the shock wave, for the results obtained in cases I and II, and the results obtained by He and Karagozian. He and Karagozian also tested a straight PDE tube of one meter in length and a divergent nozzle 1 meter long.

However, only the straight tube was filled with reactants, the nozzle was filled with inert gas. In both the present study and in Karagozian, early expansion waves were observed at the beginning of the nozzle.

He and Karagozian also found out that a significant reduction in the detonation wave strength is caused by the interface between the reactants and the inert face. In our study an almost constant pressure ratio ( $P_2/P_1$ ) of 11.0 was observed as the detonation wave moved along the PDE. He and Karagozian observed a similar pressure ratio across their detonation wave. It is important to mention that the results of He and Karagozian were obtained using a reaction mechanism which contained 8 species and 20 reactions, while this study's reaction mechanism involved 6 species and 9 reactions. Also, it is not clear whether the detonation obtained by He and Karagozian is that of a CJ, weak or strong detonation wave. He and Karagozian used the Weighted Essentially Non-Oscillatory (WENO) method for spatial interpolation of the system of governing equations. This WENO method was 5<sup>th</sup> order accurate in smooth regions and 3<sup>rd</sup> Order accurate in regions of discontinuities. This study used a first order upwind finite volume scheme both for smooth and discontinuous regions. The upwind scheme is based on the Flux Vector Splitting technique.

## V. HIGHER ORDER EXTRAPOLATION

### V.1 High Order Extrapolation Scheme Derivation

In order to increase the accuracy of the CFD code in capturing and describing the detonation wave that occurs in a Pulse Detonation Engine, the order of the code is increased from a first-order accurate code, to a sixth-order accurate code. In areas where discontinuities occur, such as shock waves, the code is decreased to first-order accuracy. This higher order accuracy is only taken in the spatial dimensions. The temporal dimension is still first order accurate.

The accuracy of the code is increased by means of a higher order extrapolation in a Taylor series expansion. The values of the conserved variables  $Q$  at cell faces are found by extrapolation of the cell centered values.

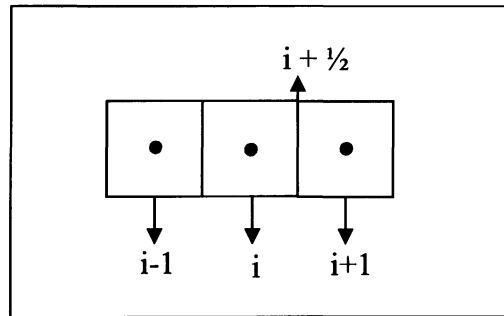


**Figure V.1 Adjacent computational cells with their respective index**

The Taylor series expansion about  $Q_i$  is performed.

$$Q_{i+\frac{1}{2}} = Q_i + \frac{\delta Q_i}{\delta \zeta} \cdot \Delta \zeta + \frac{\partial^2 Q_i}{\partial \zeta^2} \cdot \Delta \zeta^2 + \dots \quad \text{Equation V.1}$$

The previous equation can also be written as

$$Q_{i+\frac{1}{2}} = Q_i + \frac{\delta Q_i}{\delta \zeta} \cdot \Delta \zeta + O(\Delta \zeta^2) \quad \text{Equation V.2}$$

This denotes previous equation denotes that the truncation error is of the order of  $\Delta \zeta$  to the second power. Hence, this form is called “second order”.  $\Delta \zeta$  will be  $\frac{1}{2}$  in the two previous equations. To calculate the values of  $Q_{i+\frac{1}{2}}$  and  $Q_{i-\frac{1}{2}}$ , a backward difference scheme and a forward difference scheme will be used respectively. In equation V.2 the first two terms on the right of the Taylor series expansion are retained. That is  $Q_i + \frac{\delta Q_i}{\delta \zeta} \cdot \Delta \zeta$ . A finite difference is now needed for  $\frac{\delta Q_i}{\delta \zeta}$ . For a second order extrapolation scheme a first-order finite difference approximation is needed to keep the total Truncation Error (TE) to  $O(\Delta \zeta^2)$ . That is, the truncation error of the finite difference approximation  $O(\Delta \zeta)$  is multiplied by  $\Delta \zeta$ , for a total truncation error  $O(\Delta \zeta^2)$ . Thus a backward first order finite difference is,

$$\frac{\delta Q_i}{\delta \zeta} \approx Q_i - Q_{i-1} + O(\Delta \zeta) \quad \text{Equation V.3}$$

Substituting V.3 into V.2 a second order extrapolation scheme is obtained.

$$Q_{i+\frac{1}{2}} = Q_i + (Q_i - Q_{i-1}) \cdot \frac{1}{2} + O(\Delta \zeta^2) \quad \text{Equation V.4}$$

In a similar manner using a forward finite difference,

$$Q_{i-\frac{1}{2}} = Q_i + (Q_{i+1} - Q_i) \cdot \frac{1}{2} + O(\Delta \zeta^2) \quad \text{Equation V.5}$$

As it is shown, the highest derivative degree for a second order extrapolation scheme is of degree one. For a seventh order extrapolation scheme consider the following Taylor series expansion,

$$Q_{i+\frac{1}{2}} = Q_i + \frac{\delta Q_i}{\delta \zeta} \cdot \Delta \zeta + \frac{\partial^2 Q_i}{\partial \zeta^2} \cdot \frac{\Delta \zeta^2}{2!} + \frac{\partial^3 Q_i}{\partial \zeta^3} \cdot \frac{\Delta \zeta^3}{3!} + \frac{\partial^4 Q_i}{\partial \zeta^4} \cdot \frac{\Delta \zeta^4}{4!} + \frac{\partial^5 Q_i}{\partial \zeta^5} \cdot \frac{\Delta \zeta^5}{5!} + \frac{\partial^6 Q_i}{\partial \zeta^6} \cdot \frac{\Delta \zeta^6}{6!} + O(\Delta \zeta^7)$$

Equation V.6

In Equation V.6 the highest derivative degree is of degree 6. The order for the finite difference approximation needed for this sixth-degree derivative term, needs to be one to keep the total truncation error to  $O(\Delta \zeta^7)$ . With the same reasoning, a second order finite difference approximation is needed for the fifth-degree derivative term; a third order finite difference scheme for the fourth-degree derivative term; and so forth. In general, the order of the finite difference approximation increases with decreasing degree of the derivative.

A forward finite difference will be used to approximate  $Q_{i-\frac{1}{2}}$ , and a backward finite difference will be used to approximate  $Q_{i+\frac{1}{2}}$ . A method to obtain  $\frac{\partial^n Q_i}{\partial \zeta^n}$  for any  $n$  and any order of accuracy is needed. Hirsch [19] derives families of difference operators.

**Forward:**

$$\left(\frac{\partial^n Q}{\partial \zeta^n}\right)_i = \frac{1}{\delta \zeta^n} \cdot (\delta^+ - \frac{\delta^{+2}}{2} + \frac{\delta^{+3}}{3} - \dots)^n Q_i \quad \text{Equation V.7}$$

**Backward:**

$$\left(\frac{\partial^n Q}{\partial \zeta^n}\right)_i = \frac{1}{\delta \zeta^n} \cdot (\delta^- - \frac{\delta^{-2}}{2} + \frac{\delta^{-3}}{3} - \dots)^n Q_i \quad \text{Equation V.8}$$

Where

$$\delta^+ Q_i = Q_{i+1} - Q_i \quad \text{Equation V.9}$$

$$\delta^- Q_i = Q_i - Q_{i-1} \quad \text{Equation V.10}$$

$$\delta^{+2} Q_i = \delta^+ (\delta^+ Q_i) = \delta^+ (Q_{i+1} - Q_i) = Q_{i+2} - Q_{i+1} - Q_{i+1} + Q_i = Q_{i+2} - 2Q_{i+1} + Q_i \quad \text{Equation V.11}$$

The operator series to the  $n^{\text{th}}$  power in equations V.7 and V.8 is expanded for  $n = 1$  to  $n = 6$ , and the highest order of the finite difference approximation is 6. Table V.1 shows the expanded operators.

**Table V.1 Expanded operators with appropriate number of terms**

Derivative	Order	Expanded Terms (Equations V.8 and V.9)
$(\frac{\partial^1 Q}{\partial \zeta^1})_i$	6 <sup>th</sup>	$Q \pm \frac{1}{2} Q^{+2} + \frac{1}{3} Q^{+3} \pm \frac{1}{4} Q^{+4} + \frac{1}{5} Q^{+5} \pm \frac{1}{6} Q^{+6}$
$(\frac{\partial^2 Q}{\partial \zeta^2})_i$	5 <sup>th</sup>	$Q^{+2} \pm Q^{+3} + \frac{11}{12} Q^{+4} \pm \frac{5}{6} Q^{+5} + \frac{137}{180} Q^{+6}$
$(\frac{\partial^3 Q}{\partial \zeta^3})_i$	4 <sup>th</sup>	$Q^{+3} \pm \frac{3}{2} Q^{+4} + \frac{7}{4} Q^{+5} \pm \frac{15}{8} Q^{+6}$
$(\frac{\partial^4 Q}{\partial \zeta^4})_i$	3 <sup>rd</sup>	$Q^{+4} \pm 2Q^{+5} + \frac{17}{6} Q^{+6}$
$(\frac{\partial^5 Q}{\partial \zeta^5})_i$	2 <sup>nd</sup>	$Q^{+5} \pm \frac{5}{2} Q^{+6}$
$(\frac{\partial^6 Q}{\partial \zeta^6})_i$	1 <sup>st</sup>	$Q^{+6}$

In Table V.1, plus is used for backward finite differences and minus for forward differences. Also, for backward differences the sign for the exponent in  $Q^{+n}$  would be negative, as in  $Q^{-n}$ .

Using the same procedure to obtain  $Q^{+2}$  in Equation V.11,  $Q^{+3}$  to  $Q^{+6}$  can be obtained. The results are given in the following table for a forward finite difference.

**Table V.2 Finite Difference Operators expanded**

Finite Difference Operator	Expanded Terms (Equations V.8 and V.9) *
$Q$	$Q_{i+1} - Q_i$
$Q^{+2}$	$Q_{i+2} - 2Q_{i+1} + Q_i$
$Q^{+3}$	$Q_{i+3} - 3Q_{i+2} + 3Q_{i+1} - Q_i$
$Q^{+4}$	$Q_{i+4} - 4Q_{i+3} + 6Q_{i+2} - 4Q_{i+1} + Q_i$
$Q^{+5}$	$Q_{i+5} - 5Q_{i+4} + 10Q_{i+3} - 10Q_{i+2} + 5Q_{i+1} - Q_i$
$Q^{+6}$	$Q_{i+6} - 6Q_{i+5} + 15Q_{i+4} - 20Q_{i+3} + 15Q_{i+2} - 6Q_{i+1} + Q_i$

Again, for a seventh order extrapolation, Equation V.6 yields

$$Q_{i+\frac{1}{2}} = Q_i + \frac{\delta Q_i}{\delta \zeta} \cdot \Delta \zeta + \frac{\partial^2 Q_i}{\partial \zeta^2} \cdot \frac{\Delta \zeta^2}{2!} + \frac{\partial^3 Q_i}{\partial \zeta^3} \cdot \frac{\Delta \zeta^3}{3!} + \frac{\partial^4 Q_i}{\partial \zeta^4} \cdot \frac{\Delta \zeta^4}{4!} + \frac{\partial^5 Q_i}{\partial \zeta^5} \cdot \frac{\Delta \zeta^5}{5!} + \frac{\partial^6 Q_i}{\partial \zeta^6} \cdot \frac{\Delta \zeta^6}{6!}$$

Now, substituting the derivative terms found in Table V.1.0 and the expanded terms for each of the finite difference operators in Table V.2, into Equation V.6. The following relation can be obtained for a seventh order accurate scheme, assuming that  $\Delta \zeta$  is equal to  $\frac{1}{2}$ .

$$Q_{i-\frac{1}{2}} = \frac{3003}{1024}Q_i - \frac{3003}{512}Q_{i+1} + \frac{9009}{1024}Q_{i+2} - \frac{2145}{256}Q_{i+3} + \frac{5005}{1024}Q_{i+4} - \frac{819}{512}Q_{i+5} + \frac{231}{1024}Q_{i+6}$$

Equation V.12

$$Q_{i+\frac{1}{2}} = \frac{3003}{1024}Q_i - \frac{3003}{512}Q_{i-1} + \frac{9009}{1024}Q_{i-2} - \frac{2145}{256}Q_{i-3} + \frac{5005}{1024}Q_{i-4} - \frac{819}{512}Q_{i-5} + \frac{231}{1024}Q_{i-6}$$

Equation V.13

### V.3 Test Case

To verify the accuracy of the high order accuracy finite difference scheme, a validation case was set up using two known functions. One of them is a well behaved polynomial function and the other one is an exponential function. In this test case, the reduction in the error as the accuracy of the scheme is increased and the grid size is reduced, is very evident.

The two known functions tested are the following.

- $f(x) = 0.01(x^6) - 10(x^2)$  Well behaved function
- $f(x) = 0.5 \cdot e^x$

The results are shown in the next page.



**Table V.3 Test Matrix for High Order Extrapolation Scheme**

Test Matrix for High Order Extrapolation

		FUNCTIONS											
Function1		$f(x)=0.01x^6 - 10x^2$				Both Functions evaluated at $x=7.5$ for $Q(+1/2)$ , $x=6.5$ for $Q(-1/2)$							
Function2		$f(x)=0.5 \cdot \exp(x)$											
	Exact Value	Second Order		Third Order		Fourth Order		Fifth Order		Sixth Order		$\Delta x$	
		Approx Value	% Error	Approx Value	% Error	Approx Value	% Error	Approx Value	% Error	Approx Value	% Error		
Function 1 * 1000	Q(-1/2)	0.3317	0.1557	53.1	0.3891	-17.3	0.319	3.8	0.3334	-0.5	0.3316	0.0	0.5
	Q(+1/2)	1.2173	1.0413	14.5	1.171	3.8	1.2078	0.8	1.2159	0.1	1.2172	0.0	
Function 2 * 1000	Q(-1/2)	0.3326	0.1926	42.1	0.4234	-27.3	0.2737	17.7	0.3708	-11.5	0.3078	7.5	
	Q(+1/2)	0.904	0.7641	15.5	0.849	6.1	0.8824	2.4	0.8955	0.9	0.9007	0.4	
	Exact Value	Second Order		Third Order		Fourth Order		Fifth Order		Sixth Order		$\Delta x$	
		Approx Value	% Error	Approx Value	% Error	Approx Value	% Error	Approx Value	% Error	Approx Value	% Error		
Function 1 * 1000	Q(-1/2)	0.3317	0.2063	37.8	0.3582	-8.0	0.328	1.1	0.332	-0.1	0.3317	0.0	0.25
	Q(+1/2)	1.2173	1.079	11.4	1.1922	2.1	1.214	0.3	1.217	0.0	1.2173	0.0	
Function 2 * 1000	Q(-1/2)	0.3326	0.2368	28.8	0.3695	-11.1	0.3193	4.0	0.3371	-1.4	0.3311	0.5	
	Q(+1/2)	0.904	0.7909	12.5	0.8714	3.6	0.8951	1.0	0.9017	0.3	0.9034	0.1	

## VI. CONCLUSIONS AND RECOMENDATIONS

One of the objectives of this study was to obtain a detonation wave using the right set of initial conditions (pressure and temperature) so that a shock wave would form, ignited the reactants, and that the chemical reactions would form a combustion wave that caught up with the shock front and drive it across the PDE. Three cases were tested varying the initial conditions used as a “computational spark”. One of the cases was that of a simple shock tube with no chemical reactions. The following conclusions are made.

- A detonation wave was obtained for Cases I and II. This is indicated by comparison of the pressure and temperature ratio across the shock wave with the values in Table II.1; by the presence of a chemical reaction zone behind the shock wave; and by the velocity of the accelerating shock wave relative to the stagnant gases. The Mach number of the burned gas behind the shock wave indicates that the gas is moving supersonically with respect to the shock front. Thus, a weak detonation has been obtained. Note, however, that only a stoichiometric mixture of  $H_2$  and  $O_2$  was considered in this study. It is not known if other mixtures would have resulted in CJ detonation wave propagation.
- Although a detonation was obtained for Cases I and II, it is not known if the detonation wave obtained in Cases I and II would have kept accelerating or reach a steady velocity if the PDE had been a straight tube with no divergent nozzle.
- It is recommended future research on straight PDE tubes to isolate the effects of expansion waves in the divergent part of the nozzle and to determine more precisely what time of detonation is obtained.

- The effects of expansion waves being so close to the wall because of the narrow “computational spark” were hard to isolate initially. However, it was found in this study that they play an important role in determining the shape of the centerline pressure histories near the PDE wall. It is also recommended that the width of the computational spark is increased to keep the expansion waves from traveling to the wall and reflecting back almost immediately, as in Case I.
- The results of this study show that there is reasonable agreement with the results obtained in similar PDE simulations, such as those by He and Karagozian, especially with the pressure ratios across the detonation wave. The velocity however is higher in this study than the detonation velocity given in [7] because of the velocity obtained in this study is that of a weak detonation and not a CJ detonation wave. There is also some numerical error introduced due to numerical dissipation across the shock wave. The CFD code used in this study is still a first order accurate computer code in areas of discontinuities, such as shocks, and smooth regions. The chemical reaction model was also different compared to that of He and Karagozian, since in this study only 6 species were used, and 9 reactions. However, the results show that the present CFD is accurate enough to model the basic physics and chemical phenomena occurring in an ideal single cycle PDE.
- The higher accuracy code may also enable the future researcher to be able to capture acoustic phenomena and study Sound Pressure Levels, as it is done by He and Karagozian. With a higher accuracy code it may also be possible to study the DDT phenomenon.

## REFERENCES

- 1- He, X., Karagozian, A. R., "Performance and Noise Characteristics of Pulse Detonation Engines", AIAA 2004-0469, 42<sup>nd</sup> AIAA Aerospace Science Meeting, Reno, NV, January 2004.
- 2 – Kailasanath, K., "Recent Developments in the Research on Pulse Detonation Engines", AIAA 2002-0470, 40<sup>th</sup> AIAA Aerospace Science Meeting, Reno, NV, January 2002.
- 3- Anonymous, "Pulse Detonation Technology Project", NASA Glenn Research Center, [www.grc.nasa.gov/WWW/AERO/base/pdet.htm](http://www.grc.nasa.gov/WWW/AERO/base/pdet.htm).
- 4- Dean, A.J., "Recent Developments in Approaches to Pulsed Detonation Propulsion", AIAA 2003-4510, 39<sup>th</sup> AIAA Aerospace Sciences Meeting, Reno, NV, January 2003.
- 5- Perrell, E. R., Ericsson, W.D., Candler, G.U., "Numerical Solution of Nonequilibrium Condensation in a Hypersonic Wind Tunnel". Journal of Thermophysics and Heat Transfer, Vol. 10, No. 2, Apr-Jun 1996, Pgs 277-283.
- 6- Busiing, T., Eberhardt, S., "Chemistry Associated with Hypersonic Vehicles,' AIAA 1987-1792
- 7- Kuo, K. K., Principles of Combustion, John Wiley & Sons, New York, 1986.
- 8 – Malcolm W. Chase, Jr., NIST-JANAF Thermochemical Tables. 4<sup>th</sup> Edition, Part I & II. Journal of Physical and Chemical Reference Data, Monograph 9.
- 9 – Paxson, D.E., "Optimal Area Profiles for Ideal Single Nozzle Air-Breathing Pulse Detonation Engines", AIAA 2003-4512, 39<sup>th</sup> AIAA/ASME/SAE/ASEE Joint Propulsion Conference and Exhibit, July 2003, Huntsville, Alabama.
- 10 – Friedman, R. American Rocket Society J., Vol 24, p. 349, November 1953

- 11 – He. X, Karagozian, A.R., “Numerical Simulation of Pulse Detonation Engine Phenomena”, Journal of Scientific Computing, Vol. 19, Nos. 1-3, December 2003
- 12 – Gropp, W., Lusk, E., Skjellum, A., “Using MPI – Portable Parallel Programming with Message Passing Interface”. The MIT Press, Cambridge, Massachusetts. London, England. Second Edition.
- 13.- Turns, R.S. “An Introduction to Combustion – Concepts and Applications”. McGraw Hill Series in Mechanical Engineering. Second Edition.
- 14 – He. X, Karagozian, A.R., “Reactive Flow Phenomena in Pulse Detonation Engines”, AIAA 2003-1171, 41<sup>st</sup> Aerospace Sciences Meeting and Exhibit, January 2003, Reno, Nevada.
- 15 – He. X, Karagozian, A.R., “Performance and Noise Characteristics of Pulse Detonation Engines”, AIAA 2004-469, 42<sup>nd</sup> Aerospace Sciences Meeting and Exhibit, January 2004, Reno, Nevada.
- 16 – B. Lewis and J.B. Friauf, Journal of American Chemical Society, Vol. 52, p. 3905, 1930.
- 17 – Emanuel G. “Analytical Fluid Dynamics”. CRC Press LLC, second Edition, 2001.
- 18 – Anderson, J. “Modern Compressible Flow”. McGraw-Hill, Inc. 1982
- 19 – Hirsch C., “Numerical Computation of Internal and External Flows”. Volume I, Wiley and Sons, 1988.
- 20 – Steger, J., and Warming, R.F., “Flux Vector Splitting of the Inviscid Gas Dynamic Equations with Applications to Finite Difference Methods”, NASA TM-78605, 1979.